

CALIMA: ON-THE-FLY DUST AND PAH EVOLUTION FOR RADIATION-HYDRODYNAMICS GALAXY FORMATION SIMULATIONS

FRANCISCO RODRÍGUEZ MONTERO^{1,*}, YOHAN DUBOIS², HARLEY KATZ^{1,3},
ADRIANNE SLYZ⁴, JULIEN DEVRIENDT⁴

¹Kavli Institute for Cosmological Physics, University of Chicago, Chicago IL 60637, USA

²Institut d'Astrophysique de Paris, Sorbonne Université, CNRS, UMR 7095, 98 bis bd Arago, 75014 Paris, France

³Department of Astronomy & Astrophysics, University of Chicago, 5640 S Ellis Avenue, Chicago, IL 60637, USA and

⁴Sub-department of Astrophysics, University of Oxford, Keble Road, Oxford OX1 3RH, United Kingdom

Version February 26, 2026

Abstract

Dust grains and polycyclic aromatic hydrocarbons (PAHs) actively contribute to the thermodynamics, chemistry, and radiative state of the interstellar medium (ISM), yet most ISM models and galaxy simulations either exclude them altogether or adopt simplified treatments. We present CALIMA, a new module for dust and PAH formation and evolution in radiation-hydrodynamics simulations for RAMSES, designed to self-consistently couple dust physics to radiative transfer and non-equilibrium thermochemistry in a multiphase ISM. The model employs a two-size, two-composition dust framework with log-normal grain populations, explicitly evolving stellar dust injection, turbulence-informed gas-phase accretion, shattering, coagulation, thermal and non-thermal sputtering, and shock destruction, while PAHs are separate components with their own evolution. The evolving dust populations and radiation field determine local, wavelength-dependent opacities, photoelectric heating efficiencies, grain-assisted recombination, dust–gas collisional heating/cooling, and H₂ formation on both grains and PAHs. Updated treatments of thermal sputtering and collisional cooling that include finite grain sizes and modern ion–solid physics reduce sputtering rates at high temperatures and extend the regime where dust significantly cools hot gas. One-zone ISM tests show that dust and PAH evolution modifies classical thermal phase diagrams and C-bearing chemistry, while isolated disc galaxy simulations reveal environment-dependent variations in dust-to-metal ratio, small-to-large grain ratio, PAH fraction, and interstellar radiation field intensity that drive non-trivial structure in infrared emission, UV transparency, and H₂ formation. CALIMA provides a physically motivated framework to interpret dust- and PAH-based observables and to assess dust-mediated feedback in galaxy formation across cosmic time.

Subject headings: the interstellar medium, atomic and molecular clouds, dust, galaxy formation

1. INTRODUCTION

Interstellar dust grains and polycyclic aromatic hydrocarbons (PAHs) are not passive tracers of galaxy evolution. Rather they are active agents that regulate the thermodynamics, chemistry, and radiative state of the interstellar medium (ISM). Dust locks up a substantial fraction of refractory elements¹, modifies the charge balance and heating/cooling processes, mediates the formation of molecules, and sets the opacity that links stellar radiation to the gas (Draine 2011; Klessen et al. 2016). PAHs and very small grains in particular dominate the photoelectric heating of neutral gas, providing a direct feedback loop between young stars and the thermal state of the ISM (e.g. Weingartner & Draine 2001a; Verstraete 2021). Consequently, any attempt to interpret galaxy evolution through dust- and PAH-based observables must treat these components as dynamically evolving, thermodynamically active constituents rather than static by-products.

Dust grains remove heavy elements from the gas phase via depletion, thereby altering both the cooling chan-

nels and the chemical composition of the gas-phase ISM. Depletion is strong function of the local ISM properties (Jenkins 2009; De Cia et al. 2016; De Vis et al. 2017), and cosmic evolution (Wiseman et al. 2017; Konstantopoulou et al. 2022; Konstantopoulou et al. 2024). These trends imply that most refractory atoms spend a significant fraction of their lifetime bound in dust grains and that the partition between gas-phase and solid-phase metals evolves as gas cycles between ISM phases. Simultaneously, grains play a fundamental role in the free charge budget of the ISM. Through photo-emission, collisional charging and grain-assisted recombination, dust efficiently removes electrons and ions from the gas, especially in dense, shielded regions where grains tend to carry a net negative charge (e.g. Draine & Sutin 1987; Ibanez-Mejia et al. 2019; Glatzle et al. 2022). This modifies ion–molecule chemistry (Langer et al. 1976; Weingartner & Draine 2001c; Gong et al. 2019; Rimola et al. 2021) and alters ambipolar diffusion (Mouschovias et al. 1991; Kunz & Mouschovias 2010; Khesali et al. 2012), influencing the fragmentation properties of magnetised clouds. Moreover, the charge balance is highly sensitive to the local grain-size distribution and charging state (Masson et al. 2015; Guillet et al. 2020).

One of the cornerstone results of modern ISM theory is the central role of photoelectric heating (PEH) by small

*E-mail: currodri@uchicago.edu

¹ Refractory elements are those that condense into solids at relatively high temperatures compared to volatile elements. These usually include Fe, Mg, Si, Ca, Al, and Ni.

grains and PAHs in the neutral, diffuse ISM (e.g. Bakes et al. 1994; Weingartner & Draine 2001a; Wolfire et al. 2003; Glover & Mac Low 2007; Kim et al. 2013). Because the ionization potentials of many grains and PAHs lie below the Lyman limit, far-ultraviolet (FUV) photons efficiently eject valence electrons from the surface of PAHs, and the kinetic energy of these electrons is transferred to the gas. Theoretical studies consistently find that very small grains and PAHs have the largest photoelectric yields and efficiencies. The overall heating rate strongly depends on the abundance and charge distribution of the small-grain end of the size spectrum (Bakes et al. 1994; Weingartner & Draine 2001a; Berné et al. 2022). In solar-metallicity neutral gas, PEH may dominate the heating budget over a wide range of densities and radiation field strengths, with the thermal balance set primarily by the competition between this heating and cooling through CII and OI fine-structure lines (see e.g. Wolfire et al. 2003; Bialy & Sternberg 2019; Kim et al. 2023; Katz et al. 2022). Variations in the abundance or charging of PAHs and small grains therefore directly affect the position and stability of the cold and warm neutral medium (CNM/WNM) equilibrium.

Dust also provides a major cooling mechanism for star-forming gas. By absorbing UV/optical photons and re-radiating in the infrared, dust both removes energy from the radiation field and increases shielding of dense gas from young stars (see the reviews by Li & Greenberg 2003; Draine 2003a). At sufficiently high densities, gas–dust collisions couple the gas temperature to the dust internal temperature (Dwek & Werner 1981; Hollenbach & Mckee 1989), allowing thermal energy to be efficiently radiated away in the IR and enabling gas to cool to low temperatures conducive to fragmentation. The necessity of dust cooling for low-mass fragmentation was established theoretically by Schneider et al. (2002, 2006) and Omukai et al. (2005), who showed that gas–dust collisional cooling at high densities enables a second fragmentation phase inaccessible to molecular or fine-structure line cooling. Subsequent work (Schneider & Omukai 2010; Omukai et al. 2010) demonstrated that dust cooling is the only mechanism capable of producing sub-solar mass fragments at metallicities well below the fine-structure critical metallicity threshold, thereby enabling the Pop III–Pop II transition.

Chemically, dust grains act as the dominant catalytic surfaces in the ISM. They provide a thermal bath for adsorbed atoms and molecules, enabling surface reactions that are otherwise inefficient in the gas phase. Of particular importance is molecular hydrogen: under typical ISM conditions, H_2 formation proceeds mainly on grain surfaces, with rates determined by the total grain surface area, surface properties, and dust temperature (Cazaux & Tielens 2002, 2004; Bron et al. 2014). Dust grains also serve as the seeds for the first solid phases of many molecules in the cold and dense ISM. The build-up of icy mantles on grain surfaces is a critical step in the formation of complex organic molecules and the onset of abiogenesis (e.g. Tielens & Hagen 1982; Allamandola et al. 1988; Schutte 1995).

Dust may play an important dynamical role through radiation pressure, both by (single-)scattering of UV/optical photons and through the scattering, emission, and re-emission (usually termed multi-scattering) of infrared

(IR) photons. Radiation pressure on dust plays markedly different roles across scales. On molecular cloud scales, it couples efficiently to dense, optically thick gas and acts as a robust feedback mechanism that contributes to cloud disruption and the regulation of star formation (e.g. Krumholz & Dekel 2010; Murray et al. 2010). Even so, its importance on galactic scales is far less certain: early models invoking efficient infrared multi-scattering suggested radiation pressure could drive large-scale outflows (Murray et al. 2005; Thompson et al. 2005), but subsequent multidimensional radiation-hydrodynamic simulations have shown that instabilities, porosity, and photon leakage substantially reduce momentum coupling, rendering radiation pressure generally subdominant to supernova feedback except in extreme starbursts (Krumholz & Thompson 2013; Hopkins et al. 2014; Rosdahl et al. 2015). These conclusions remain sensitive to poorly constrained dust properties, including dust-to-gas ratio, grain size distribution, and opacity, which are expected to vary strongly with environment and redshift. Thus, self-consistent evolution of dust is a necessary step towards understanding the role of radiation pressure on galaxy formation and the ISM. This is particularly relevant nowadays, given the revived interest in radiation-driven ejection of dust to explain the ‘apparent’ attenuation-free galaxies observed in the early Universe (e.g. Ferrara et al. 2022; Pallottini & Ferrara 2023; Ferrara 2024).

Self-consistent evolution of dust and PAHs is not only necessary for their feedback on the ISM and galaxy formation, but also for a direct prediction of their observables across cosmic time. PAH emission bands in the 3–20 μm range predominantly originate in photodissociation regions (PDRs), at the surfaces of molecular clouds, and within or around H II regions (see the review by Tielens 2008). As their presence correlates with the far-UV (FUV) field, observations with ISO and Spitzer established that PAH emission scales with star formation rate (e.g. Genzel et al. 1997; Peeters et al. 2004; Calzetti et al. 2007). However, the overall strength, spectral shape, and relative mid-infrared band fluxes of PAH emission depend sensitively on local physical conditions, including gas density (Joblin et al. 1996; Verstraete et al. 2001; Sandstrom et al. 2023; Chasten et al. 2023), radiation field intensity and hardness (Boulanger et al. 1998; Peeters et al. 2002; Galliano et al. 2008b; Egorov et al. 2023; Egorov et al. 2025), and metallicity (Engelbracht et al. 2005; Madden et al. 2005; Sandstrom et al. 2012; Chasten et al. 2023). In particular, the PAH-to-dust mass ratio exhibits a much steeper dependence on metallicity than either the dust-to-gas or dust-to-metal ratios, with PAH emission strongly suppressed in low-metallicity environments (e.g. Whitcomb et al. 2024; Shivaeei et al. 2024). The combined effects of PAH destruction in hard radiation fields, this strong metallicity dependence, and the contribution of evolved stellar populations to PAH excitation (e.g. Helou et al. 2001; Calzetti et al. 2007; Bendo et al. 2010; Chasten et al. 2023) render PAH emission a complex and intrinsically environment-dependent tracer of star formation.

Early dust evolution models extended classical chemical evolution frameworks, evolving dust in one-zone or multi-zone schemes alongside gas, stars, and metals (e.g. Dwek 1998; Zhukovska et al. 2008; Asano et al. 2013;

Hirashita 2015). These models included stellar dust injection by SNe and AGB stars, destruction in SN shocks, and grain growth in the ISM, and were computationally inexpensive yet highly effective at exploring dust-to-gas relations, dust mass build-up, and extinction in idealized galaxies (see the compilation by Parente et al. 2025). Coupled to semi-analytic galaxy formation models, they reproduced global dust scaling relations and the cosmic dust budget (e.g. Lisensfeld & Ferrara 1998; Calura et al. 2007; Popping et al. 2017; Vijayan et al. 2019), but could not capture the spatially resolved coupling between dust, radiation, and ISM thermodynamics. Hydrodynamical simulations of galaxy formation have long tracked metal abundances, motivating early dust treatments based on simple scalings between metals and dust calibrated on the Milky Way (MW) or nearby galaxies. As resolved observations of dust abundances have pointed out, a fixed DTM overpredicts dust masses in low-metallicity environments and underpredicts them in metal-rich systems where ISM grain growth dominates. This leads to systematic biases in dust masses, attenuation, and IR luminosities in cosmological simulations (see e.g. McKinnon et al. 2017; Byun et al. 2025, for a comparison between these simplified approaches and live dust evolution models).

Live dust models address these issues by evolving dust as a separate component with explicit sources and sinks, so that local dust-to-metal ratios emerge from the physical conditions and the thermodynamic evolution of the gas. The increased availability of large-scale computational resources has driven a rapid expansion in the development of live dust models for cosmological galaxy formation simulations (e.g. Bekki 2013; McKinnon et al. 2016; Aoyama et al. 2017; Hou et al. 2017; Gjergo et al. 2018; Li et al. 2019; Aoyama et al. 2020; Granato et al. 2021; Parente et al. 2022; Romano et al. 2022b; Choban et al. 2022; Dubois et al. 2024). Sub-grid prescriptions track different size bins or species, including stellar seeding, accretion from the gas phase, shattering, coagulation, and destruction in SN shocks and hot gas. This new generation of simulations has achieved important successes: matching the cosmic dust density evolution to at least cosmic noon (e.g. McKinnon et al. 2017; Aoyama et al. 2018; Li et al. 2019; Ragone-Figueroa et al. 2024; Trayford et al. 2025), recovering observed relations between metallicity and dust-to-gas/dust-to-metal ratios (e.g. Zhukovska 2014; Hou et al. 2019; Dubois et al. 2024), capturing the transition from stellar-source-dominated to ISM growth-dominated dust production at higher metallicities (e.g. Hou et al. 2019; Granato et al. 2021; Choban et al. 2024; Narayanan et al. 2025), and reproducing environment-dependent grain processing (e.g. Gjergo et al. 2018), radial dust profiles (e.g. Granato et al. 2021; Parente et al. 2022), spatial dust inhomogeneities across ISM phases (e.g. Zhukovska et al. 2016; Hu et al. 2019; Matsumoto et al. 2024), and extinction-curve trends driven by evolving grain size distributions (e.g. Aoyama et al. 2020; Romano et al. 2022a; Dubois et al. 2024).

Despite this progress, the coupling of live dust to radiation transfer and thermochemistry remains incomplete in most galaxy and ISM-scale simulations. Many models evolve dust mass (and sometimes size distributions) but still employ static or metallicity-scaled opacities in

radiative transfer, so changes in small-grain and PAH abundances, coagulation, or shattering do not feed back into UV/optical attenuation or radiation pressure. Conversely, simulations that prioritize detailed multiphase ISM structure and non-equilibrium chemistry typically rely on empirical dust prescriptions: metal depletions are not consistent with the adopted cooling curves, photoelectric heating efficiencies are fixed or tied only to bulk dust abundance, and H₂ formation rates depend on Milky Way-calibrated efficiencies rather than on the properties of an evolving grain population. Cosmological live-dust simulations often lack on-the-fly radiative transfer, using approximate UV backgrounds and line-of-sight treatments that ignore detailed dust properties, while PAHs are almost always implemented via fixed templates or post-processing rather than as a live component that modifies local heating and opacities.

We present a new implementation of dust and PAH evolution in the RAMSES hydrodynamical galaxy formation code (Teyssier 2002), in its version adapted for on-the-fly radiative transfer (RAMSES-RT, Rosdahl et al. 2013; Rosdahl & Teyssier 2015) and its direct coupling to the non-equilibrium chemistry of primordial, metal, and molecular species (RAMSES-RTZ, Katz 2022). Section 2 describes the two-size dust evolution model, including its coupling to gas heating, cooling, and radiative transfer. Section 3 extends this framework to include the chemistry, evolution, and impact of PAHs in the ISM. In Section 4.1 we assess the impact of individual dust and PAH processes on the equilibrium structure of the local ISM, and in Section 4.2 we apply the full model to an isolated galaxy simulation. Finally, Section 5 discusses how this implementation relates to previous dust evolution models in RAMSES and outlines its limitations, while Section 6 summarises our main results and future prospects.

2. THE TWO-SIZE DUST MODEL

The dust size distribution is the result of the complex interplay between dust formation and destruction. Because interstellar extinction spans a wide range of wavelengths, grains with radii a satisfying $2\pi a/\lambda \sim 1$ tend to contribute most efficiently to the extinction at wavelength λ . The grain-size distribution (GSD) derived from this premise extends over many orders of magnitude and is usually explained by two fundamental processes: collisional fragmentation and turbulent grain growth. If one considers an initial distribution dominated by large dust grains (possibly seeded by AGB winds or SNe Type II ejecta, see Section 2.1 for further details) the large relative velocities of grains can easily result in collisions that break apart these grains into fragments of smaller sizes. This process of shattering was originally discussed by Hellyer (1970) in the context of asteroid collisions, and later introduced within the framework of interstellar dust grains by Dorschner et al. (1982). For a simplified derivation, see Chapter 5.5.2 of Krügel (2008), but the fundamental result is the prediction of a power-law grain distribution such that the grain number density n with radius a scales according to $n(a) \propto a^{-3.5}$, in agreement with the canonical Mathis-Rumpl-Nordsieck (MRN) distribution (Mathis et al. 1977) for the MW diffuse ISM. While the collisional fragmentation model predicts that an initial large dust grain distribution evolves towards a power law distribution, based on the conservation of dust

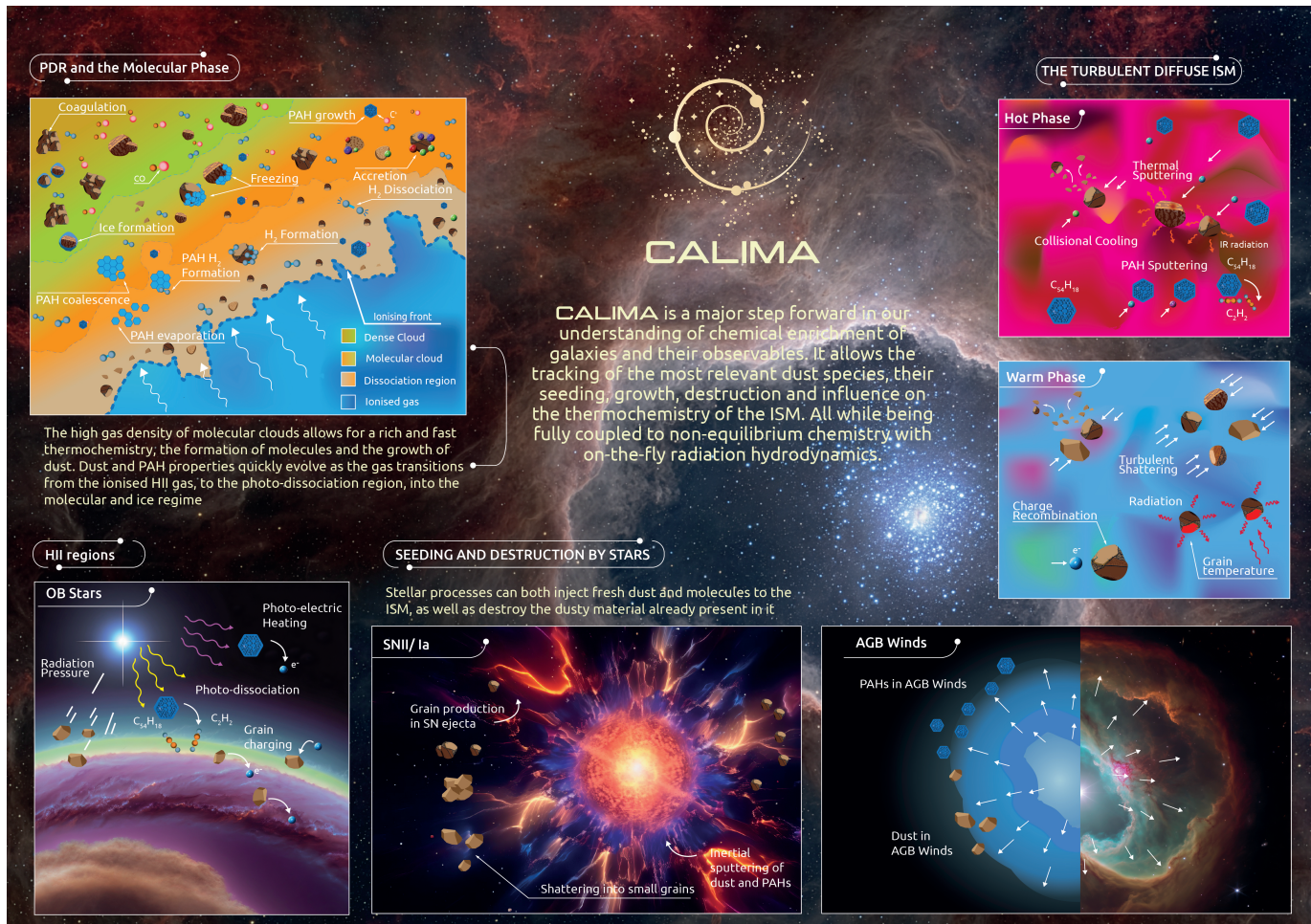


FIG. 1.— Overview of the CALIMA model. Click on a process name to jump to its detailed description.

mass in high velocity collisions and without evaporation, (see also Section 2.8), turbulent grain growth is needed to explain the growth of dust mass after it is injected into the ISM.

There is well established observational evidence for supersonic ISM turbulence, which according to theory and simulations gives rise to an approximately log-normal² distribution of gas densities (see reviews by Low & Klessen 2004; Elmegreen & Scalo 2004; McKee & Ostriker 2007; Hennebelle & Falgarone 2012). In Section 2.4 we carefully examine how the growth of dust grains by gas-phase accretion of metals depends on gas density. Given the large variance of the gas density field caused by supersonic turbulence, dust accretion occurs on different timescales within a turbulent ISM. Therefore, the assumption that gas and dust grains are highly coupled implies that dust grain size correlates with gas density distribution. Even if the initial dust grain size distribution follows a power law, the memory of the initial conditions will be quickly erased by the underlying gas density field (Mattsson et al. 2020).

These two scenarios explain the origin of two widely used GSDs: power-laws and log-normals (e.g. Compiègne

et al. 2010; Jones et al. 2017; Zubko et al. 2004; Hensley & Draine 2021). However, these models make different assumptions about grain type and GSD spatial variation. Nevertheless, both models agree on the following aspects of the diffuse ISM grain properties (Krügel 2008):

1. The sizes of very small carbonaceous grains (VSGs) need to peak in the range between $3 \leq a \leq 30 \text{ \AA}$, so that they can be stochastically heated to the high temperature necessary to explain mid-IR features (see Section 3).
2. Small (but larger than VSGs) grains in the range from $\sim 5 \text{ nm}$ to $\sim 30 \text{ nm}$ contribute to the mid-IR continuum. Whether or not silicate grains are also found at these sizes determines whether there are 9.7 and $18 \mu\text{m}$ emission features due to O-Si-O bending.
3. The sizes of large grains need to peak at $\sim 0.1 \mu\text{m}$ and have a sharp cut-off at larger a . This constraint arises from multiple observational probes: the near-IR and optical extinction slope (e.g. Cardelli et al. 1989; Fitzpatrick 1999; Weingartner & Draine 2001b), scattering of diffuse galactic light (e.g. Brandt & Draine 2011), and scattering from X-ray sources (e.g. Predehl & Schmitt 1995; Draine & Tan 2003).

² There is strong evidence that the probability density function (PDF) deviates from log-normal at high Mach numbers (e.g. Federrath & Klessen 2012; Hopkins 2013; Federrath & Banerjee 2015; Hennebelle et al. 2024).

	s [g cm ⁻³]	N_C	a_0 [μ m]	a_{\min} [μ m]	a_{\max} [μ m]	σ
small PAHs	2.0	54	5×10^{-4}	3×10^{-4}	1×10^{-3}	0.3
large PAHs	2.0	418	1×10^{-3}	3×10^{-4}	9×10^{-3}	0.4
small C	2.2	-	1×10^{-2}	1×10^{-3}	1×10^{-1}	0.7
large C	2.2	-	1×10^{-1}	5×10^{-3}	1.0	0.8
small Sil	3.3	-	5×10^{-3}	5×10^{-4}	1×10^{-1}	0.75
large Sil	3.3	-	1×10^{-1}	5×10^{-3}	1.0	0.75

TABLE 1: Fiducial parameters for the full CALIMA model. All grain/molecules assume a modified log-normal GSD given by Eq. 1. From left to right columns: material density, number of carbon atoms in the PAH molecule, grain/molecule centroid radius, minimum and maximum size cut-offs, and width of the log-normal distribution.

Therefore, temporarily ignoring the source of aromatic features attributed to VSGs, the GSD can be roughly described by a population of small grains with $a \leq 30$ nm and a population of large grains with $a > 30$ nm. This is considered to be the minimal two-size approximation for the evolution of the GSD in the ISM (Hirashita 2015), and captures the main features of the full GSD (Asano et al. 2013). Similar to the two-size approximation adopted by other galaxy formation simulations (Aoyama et al. 2017; Gjergo et al. 2018; Granato et al. 2021), we model small and large grains with central bin sizes given in Table 1. PAHs are also separated in small ($a_0 = 5\text{\AA}$) and large ($a_0 = 10\text{\AA}$) bins (see Section 3 for further details with respect to this discretisation). We assume that the underlying GSD within each bin is a modified log-normal:

$$n(a)da = \frac{C}{a^4} \exp\left(\frac{[\log(a/a_0)]^2}{2\sigma^2}\right) da, \quad (1)$$

where the grain number density $n(a)$ has been defined as the number of grains per unit volume with radius in the range $a \rightarrow a + da$. This log-normal is centred at a_0 , and with standard deviation given by σ . The normalisation constant C is obtained for each cell and each grain type j :

$$C_j = \frac{m_j n_{d,j}}{\int_{a_{\min,j}}^{a_{\max,j}} \frac{4}{3} \pi \frac{s_j}{a} \exp\left(\frac{[\log(a/a_0)]^2}{2\sigma^2}\right) da}, \quad (2)$$

which arises from relating the local dust density to the integral of the underlying distribution. Here $m_j = \frac{4}{3} \pi s_j a_0^3$ is the mass of a single dust grain, $n_{d,j}$ is the dust number density, and s_j is the grain material density.

Fig. 2 shows the decomposition of the underlying GSD for the full CALIMA model, separating carbonaceous grains in the left panel, from silicate grains in the right panel. Abundance for each grain type is inferred using the BARE-GR-S model in Zubko et al. (2004). We compare our results to the slope of the MRN distribution: our choice of underlying GSD and MW abundances assumption agrees with an MRN extending from large grains to the smallest PAHs.

In addition to dividing the dust grain population into large and small size bins, we separate the dust composition into amorphous carbonaceous grains and silicate grains with a fixed stoichiometry for a given simulation. We briefly review our choice of silicate properties.

Silicate compounds are built around the silica tetrahedra SiO_4^{4-} . Due to their overall negative charge, they pair by ionic bonds with interstellar cations, which due to cosmic abundance are limited to Mg^{2+} and Fe^{2+} (e.g. Asplund et al. 2009). Olivine and pyroxene are typically considered the relevant silicate compositions for as-

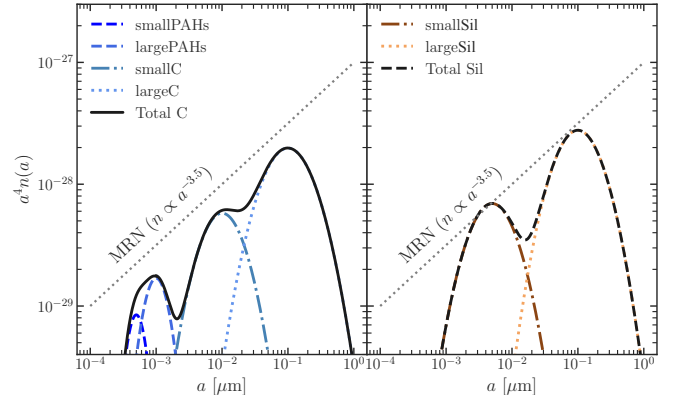


FIG. 2.—: Underlying grain size distribution assumed within each size bin in the CALIMA model for PAHs, carbonaceous grains and silicate grains. This has been computed for a gas density of 1 H cm^{-3} and using the DTG for each individual component (PAH, carbonaceous, silicate) of the BARE-GR-S model in Zubko et al. (2004).

trophysical dust grains (see the reviews by Dorschner & Henning 1995; Draine 2003a; Henning et al. 2010). Olivine crystals are characterised by a orthorhombic network of silica tetrahedra joined by dications, while in pyroxene the crystalline structure can be either orthorhombic or monoclinic. The general composition of olivine is $\text{Mg}_{2x}\text{Fe}_{2-2x}\text{SiO}_4$, and of pyroxene is $\text{Mg}_x\text{Fe}_{1-x}\text{SiO}_3$, with x ranging from 0 to 1 depending on the Mg-Fe inclusion ratio. As Mg and Fe are interchangeable on the crystalline lattice, both olivine and pyroxene can be considered as a solid solution of magnesium and iron.

Since we fix the silicate composition in any given CALIMA simulation, our choice will influence the exact depletion of refractory elements from the gas phase. Different studies have tried to put constraints on the (Fe+Mg)/Si ratio of astrophysical silicates. Sofia et al. (2001) finds that interstellar depletion results in a 2:1 ratio, suggesting a $(\text{Mg,Fe})\text{SiO}_4$ composition, with X-ray spectroscopy finding evidence of a mix of silicates with olivine- and pyroxene-type³ composition (Costantini et al. 2001). However, these compositions appear to be in disagreement with the depletion factors determined by Jenkins (2009), which suggest a Si:O ratio close to 6.6 ± 2.5 . It remains difficult to account for the depletion of oxygen in galactic dust models, even if it also forms oxides (e.g. Choban et al. 2022). Given the modelling difficulty involved, we leave the exploration of different silicate compositions for future work and instead assume a composition of olivine with equal amounts of

³ The olivine and pyroxene terms are specific to crystalline silicate structures, but we use them across this paper as a way to refer to the *effective* stoichiometry of a given amorphous silicate.

Mg and Fe inclusions (MgFeSiO_4) as commonly done to represent the interstellar silicate absorption profiles (i.e. the 9.7 and 18 μm features, [Draine et al. 1984](#); [Li & Draine 2001](#); [Kemper et al. 2004](#); [Chiar & Tielens 2005](#)), although we note that there is tentative evidence of Mg-rich silicates in starburst systems ([Min et al. 2007](#)).

This minimal model (two grain size bins, and two chemical species, i.e. carbonaceous and silicate grains) is capable of capturing the primary features of the Galactic GSD, while remaining computationally efficient in terms of memory usage and simplifying the number of inter-grain reaction rates.

2.1. Grain seeding

The amount of silicates m_{key} , traced by its key element (here Si), released by a single star is given by the mass of the least abundant element entering its composition:

$$m_{\text{key}} = \min_{\ell=\text{Mg,Fe,Si,O}} \left(\frac{M_\ell}{A_\ell N_\ell} \right), \quad (3)$$

with M_ℓ the total mass of the ℓ -th element released by the star, A_ℓ its atomic weight and N_ℓ the number of ℓ -th element atoms entering the composition of the silicate. The key element condensates within the ejecta into dust of mass $D_{\text{ej,sil},\ell}^k$ with a given efficiency δ_{Sil} according to the formula:

$$D_{\text{ej,sil},\ell}^k = \delta_{\text{Sil}}^k m_{\text{key}} A_\ell N_\ell \quad (4)$$

which guarantees a constant mass ratio with values $A_\ell N_\ell / \sum (A_\ell N_\ell) = 0.14, 0.33, 0.16, 0.37$ for $\ell = \text{Mg, Fe, Si, and O}$ respectively for the case of $x = 1$ olivine⁴. The superscript k denotes the origin of the stellar mass release with $k = \text{AGB, SNII or SNIa}$. The condensation efficiency for SNII following [Dwek \(1998\)](#) is equal to $\delta_{\text{Sil}}^{\text{SNII}} = 0.8$. Contrary to [Dwek \(1998\)](#), we do not consider dust formation in SN Ia, as models suggest that formation efficiency is drastically reduced in SN Ia (e.g. [Nozawa et al. 2011](#)), and observations have yet to find newly formed dust around them ([Gomez et al. 2012](#)). For AGB stars, the condensation efficiency depends on the ratio of C/O: if $\text{C/O} \geq 1$ all the oxygen is associated to carbon in CO molecules, and, hence, silicates do not condensate anymore due to the unavailability of O, while with $\text{C/O} < 1$ oxygen is still available to condense into silicates. We adopt $\delta_{\text{Sil}}^{\text{AGB,C/O}<1} = 0.8$ and $\delta_{\text{Sil}}^{\text{AGB,C/O}\geq 1} = 0$ as in [Dwek \(1998\)](#). For the same reasons, accretion of elements onto silicates from the ISM will be limited by the least abundant of the elements in the ISM entering the composition of the grain, replacing the total mass M_ℓ released by the star by the gas mass of the given element ℓ in the cell.

Similarly to silicates, the amount of carbonaceous dust and its condensation efficiency δ_{C}^k vary with the nature of the stellar ejecta. We assume $\delta_{\text{C}}^{\text{SNII}} = 0.5$ and $\delta_{\text{C}}^{\text{SNIa}} = 0$, while for AGB stars this efficiency depends on the ratio of C/O in the ejecta. If the ratio $\text{C/O} < 1$, then all the C elements form CO molecules that are then not

available for dust $\delta_{\text{C}}^{\text{AGB,C/O}<1} = 0^5$, while for $\text{C/O} \geq 1$ the efficiency is 1 with a mass released into C dust:

$$D_{\text{ej,C}}^{\text{AGB}} = \delta_{\text{C}}^{\text{AGB,C/O}\geq 1} \left(M_{\text{C}}^{\text{AGB}} - \frac{A_{\text{C}}}{A_{\text{O}}} M_{\text{O}}^{\text{AGB}} \right). \quad (5)$$

The dust produced in stellar ejecta is divided into a population of small and large grains, i.e. $\dot{D}_{\text{ej},i,\text{S}}^k = f_{\text{ej},i,\text{S}} \dot{D}_{\text{ej},i}$ and $\dot{D}_{\text{ej},i,\text{L}}^k = (1 - f_{\text{ej},i,\text{S}}) \dot{D}_{\text{ej},i}$, where $f_{\text{ej},i,\text{S}}$ is the fraction of small grains released for a given chemical type i (carbonaceous or silicate grains). Observational studies of dust in young SN remnants (SNRs) indicate that SN-condensed dust is frequently dominated by relatively large grains. Far-IR spectral modelling of the Crab Nebula requires size distributions with significant mass in grains $\gtrsim 0.1\mu\text{m}$ (e.g. [Blair et al. 1997](#); [Temim & Dwek 2013](#)), and analyses of Galactic SNRs show trends in extinction properties consistent with size redistribution towards large grains ([Zhao et al. 2025](#)). Additionally, modelling of SN dust survival indicates that larger grains have much higher survival fractions through reverse shock processing (e.g. [Nozawa et al. 2007](#); [Slavin et al. 2020](#)). We assume that all the dust released in the ejecta condenses into the large grain population only, thus, $f_{\text{ej},i,\text{S}} = 0$ (see appendix B in [Dubois et al. 2024](#) for the predictions of extinction curves with different values of $f_{\text{ej},i,\text{S}}$). These efficiencies can easily be used with the metal yields of any stellar model. Finally, it is important to note that the predicted and observed dust condensation efficiencies are very uncertain and can vary by up to an order of magnitude (see the review by [Schneider & Maiolino 2024](#)).

2.2. Grain charging

Dust grains constantly interact with ions and molecules in ISM, generally causing the grain to acquire a charge⁶ Q_{g} . In the diffuse ISM, where grains are subject to more intense radiation fields, they may be stripped of electrons by photons, resulting in an overall positive charge, whereas in dense clouds, dust grains can capture free electrons rendering them negatively charged. This has a non-negligible effect on the interaction of grains with each other and the gas, since accretion of gas phase metals is affected by electrostatic forces between the grain and ion (e.g. [Weingartner & Draine 1999](#); [Zhukovska et al. 2018](#)), photo-electric yields are highly dependent on the ionisation potential of the grain ([Bakes et al. 1994](#); [Weingartner & Draine 2001a](#)), charged dust dynamics is affected by electrostatic drags and acceleration by magnetic field fluctuations (e.g. [Yan et al. 2004](#)), and magnetic resistivities on collapsing protostellar cores depends on the charge acquired by grains under low ionisation fractions and high densities. Therefore, dust charging is a very important process for the thermo-dynamical interaction of dust grains with the ISM. Despite this, it has been restricted to just a few implementations in photo-ionisation/spectral synthesis codes (MEUDON

⁵ For consistency, we should then release CO in this situation, but contrary to dust grains, RAMSES-RTZ includes direct formation of CO from gas-phase C and O, so we assume that the direct formation is predicted by the chemistry solver.

⁶ Throughout this work it is assumed that grain charge Q_{g} is in units of the elementary charge e .

⁴ $A_\ell N_\ell / \sum (A_\ell N_\ell) = 0.11, 0.24, 0.24, 0.41$ for $\ell = \text{Mg, Fe, Si, and O}$ respectively for the case of $x = 1$ pyroxene.

PDR, CLOUDY, and MOCASSIN, Le Petit et al. 2006; Ferland et al. 2017; Ercolano et al. 2008, respectively), Monte-Carlo radiative-transfer (CRASH, Glatzle et al. 2022), and post-processing dust modelling tools for SN ejecta (PAPERBOATS, Kirchschrager et al. 2019).

Introducing explicit grain-charging in radiation hydrodynamics (RHD) simulations is non-trivial, since dust grains have a large reservoir of valence electrons as well as sufficiently low electron affinity to allow capture of free electrons. This results in grain charge distributions (GCDs) that extend over a very broad range of positive and negative charges, established from the equilibrium of collisional and photo-emission charging (see Weingartner & Draine 2001a). Given the computational and memory cost of obtaining the equilibrium GCD at every cooling time-step and in every cell of our RAMSES simulation, we instead make use of tabulated values of grain mean charge and the width of the GSD for the local conditions. The underlying assumptions from these tables are: (i) an averaged interstellar radiation field (ISRF) of photo-emission efficiency, and (ii) charging timescales much shorter than the cooling and hydrodynamical time-steps (see Ibanez-Mejia et al. 2019, showing that this is a good assumption for grains larger than PAHs).

CALIMA uses pre-computed tables of the GSDs using the theoretical framework of Weingartner & Draine (2001a). This allows us to predict the evolution of the GCD for the individual grain sizes and compositions used in CALIMA. We provide further details of the algorithm to compute the equilibrium GCD in Appendix A. In Fig. 3 we represent the GCD mean charge $\langle Q_g \rangle$ and width σ_{Q_g} of small silicate grains for a range of values of the charging parameter⁷ $\gamma = G_0\sqrt{T}/n_e$ (T is the gas temperature and n_e is the free electron number density). Previous works have argued that the GCD can be solely parametrised by γ (e.g. Weingartner & Draine 2001a; Ibanez-Mejia et al. 2019) when considering an average ISRF like the one from Mathis et al. (1983). In order to test this assumption, we have computed the GCD for different combinations of n_e and T that result in the same value of γ , represented in Fig. 3 by different marker size (varying n_e) and different colours (varying T). We find that there is a non-trivial second dependence on T , which suggest that fitting functions, like the ones from Ibanez-Mejia et al. (2019), may fail to fully capture the variation in grain charge with temperature (see the orange curves in Fig. 3 that result from using their fitting parameters). To help in the physical understanding of this temperature dependence, we have overplotted running medians of $\langle Q_g \rangle$ and σ_{Q_g} for low temperature $T < 10^4$ K (green, solid lines) and high temperature $T > 10^4$ K (red, dot-dashed lines). While for low temperature the collisional charging is not sufficient to overcome the photo-detachment and photo-emission caused by the Mathis et al. (1983) ISRF, sufficiently high gas temperatures allow for the collisional charging rate to exceed any photo-emitting rate, which causes these small grains to acquire a negative charge as γ (and, effectively, n_e) decreases. The grain can keep decreasing its charge until the minimum allowed charge (see the definition of Q_{\min} in Ap-

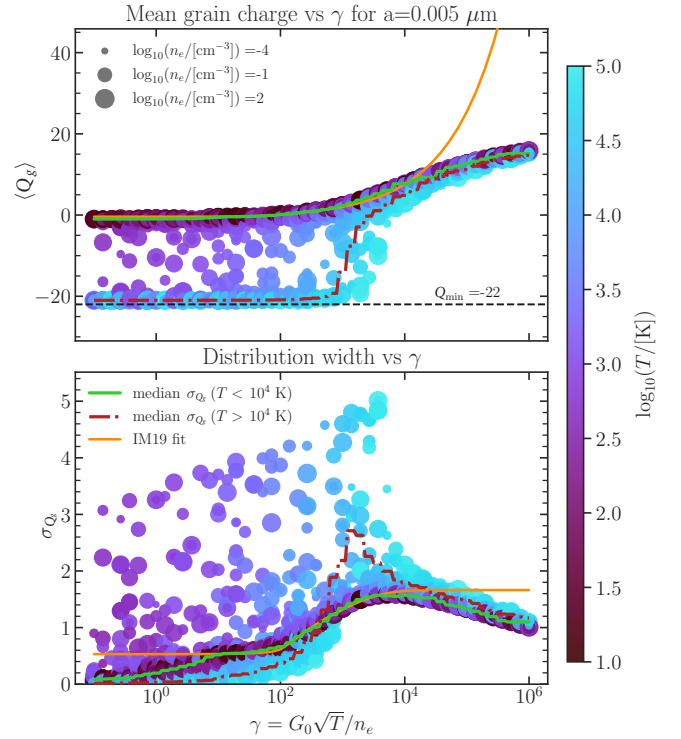


FIG. 3.—: Equilibrium grain charge of the small silicate grains ($a = 0.005 \mu\text{m}$) under the Mathis et al. (1983) ISRF. Each point describes the charge probability distribution by the mean $\langle Q_g \rangle$ (top panel) and width σ_{Q_g} (bottom panel) at a given value of the charging parameter $\gamma = G_0\sqrt{T}/n_e$. For a fixed γ , we also vary T between 10 K and 10^5 K and n_e between 10^{-4} and 10^2 cm^{-3} , represented by the colourmap and the size of the point, respectively. The result from the equilibrium modelling by Ibanez-Mejia et al. (2019) is overplotted as solid orange lines, compare to the median of our distribution for neutral ($T < 10^4$ K) and ionised gas ($T > 10^4$ K).

pendix A) is reached, which for small silicate grains is $Q_{\min} = -22$ (indicated by a horizontal dashed line in the top panel of Fig. 3). In practice, we have tabulated the mean charge and the width of the GCD varying γ and T , which allows quick computation of the GCD properties for each grain in CALIMA considering the properties of the local radiation field.

2.3. Dust photo-electric heating and recombination cooling

Photo-electric heating (PEH) is the dominant source of heating in the diffuse ISM as the gas metallicity approaches solar values (e.g. Wolfire et al. 2008; Bialy & Sternberg 2019; Kim et al. 2023; Katz et al. 2022). PEH is also the dominant process that couples the sub-ionising ($E < 13.6 \text{ eV}$) far-UV radiation field to the diffuse gas, therefore controlling the ionisation state of PDRs and the phase structure of the ISM. Originally proposed by Spitzer et al. (1948), it has been the subject of extensive theoretical modelling (e.g. Bakes et al. 1994; Weingartner & Draine 2001c). Essentially, absorption of a far-UV photon results in the release of an electron, which loses energy as it travels through the grain material. If the electron reaches the grain surface with sufficient energy

⁷ G_0 is the radiation energy density in the Habing band (i.e. 6-13.6 eV) normalised to the Habing (1968) estimate of $u_{\text{Hab}} = 5.33 \times 10^{-14} \text{ erg cm}^{-3}$

to overcome the work function W of the material, it may escape the grain and become a free electron that contributes to the thermal state of the gas.

The implementation of PEH in thermo-chemical models of the ISM relies on fitting functions to the total gas heating per H nucleus and per Habing band flux G_0 , assuming a particular composition mix of dust grains and a GSD (see e.g. [Bakes et al. 1994](#); [Weingartner & Draine 2001a](#)). However, this classical approach would be inconsistent with the multi-size, multi-composition capabilities of CALIMA. Instead we make use of our modelling of dust charging (Section 2.2 and Appendix A) to revisit the properties of PEH for individual grain sizes and compositions⁸. The dust charging model can be easily extended to consider the per-grain heating ([Weingartner & Draine 2001a](#)):

$$\Gamma_{\text{PEH}}(a) = \sum_{Q_g} f(Q_g, a) [\Gamma_{\text{PEH},v}(Q_g, a) + \Gamma_{\text{pd}}(Q_g, a)], \quad (6)$$

where f is the probability of grain a to have charge Q_g , and $\Gamma_{\text{PEH},v}$ and Γ_{pd} are the PEH contribution from valence electrons and photo-detachment of electrons in the lowest unoccupied molecular orbit, respectively. The sum is over the GCD computed with the method in Appendix A. These heating rates are computed from Eqs. 39 and 40 in [Weingartner & Draine \(2001a\)](#). Recombination of electrons and ions onto the grain result in a loss $\Lambda_{\text{rec}}(a)$ of thermal energy from the gas phase, which we compute following Eq. 3.6 in [Draine & Sutin \(1987\)](#). We benchmark our implementation by computing the total efficiency for conversion of absorbed radiation into net gas heating:

$$\epsilon_{\text{PEH}}(a) = \frac{\Gamma_{\text{PEH}}(a) - \Lambda_{\text{rec}}(a)}{P_{\text{abs}}(a)}, \quad (7)$$

where $P_{\text{abs}}(a)$ is the integrated radiation absorbed power by a grain of radius a . We compute this efficiency for graphite and silicate grains within the [Mathis et al. \(1983\)](#) ISRF and the definition of WNM phase in [Weingartner & Draine \(2001a\)](#). Our results are plotted in Fig. 4 (blue for graphite, brown for silicate) in comparison to the results of [Weingartner & Draine \(2001a\)](#) in their Figure 12 (carbonaceous, dotted line) and Figure 13 (silicates, dot-dashed line). Besides deviations at $a \lesssim 100 \text{ \AA}$ caused by different choices of graphite optical properties (see Appendix A for further details) in [Weingartner & Draine \(2001a\)](#), our results seamlessly match theirs. Given the computational and memory imprint of obtaining the full GCD, we continue our approach in Section 2.2 by pre-computing $\Gamma_{\text{PEH}}(a)$ and $\Lambda_{\text{rec}}(a)$ for each grain size and composition followed in CALIMA for a range of γ and T .

2.4. Gas-phase accretion

The primary mode of dust mass growth in the ISM is by accretion of refractory elements from the gas phase. As in [Dubois et al. \(2024\)](#), we model accretion of metals onto grains by a modified version of the collisional argument laid out in [Dwek \(1998\)](#). The mass density

⁸ We cover the modelling of PEH for PAHs in Section 3.5

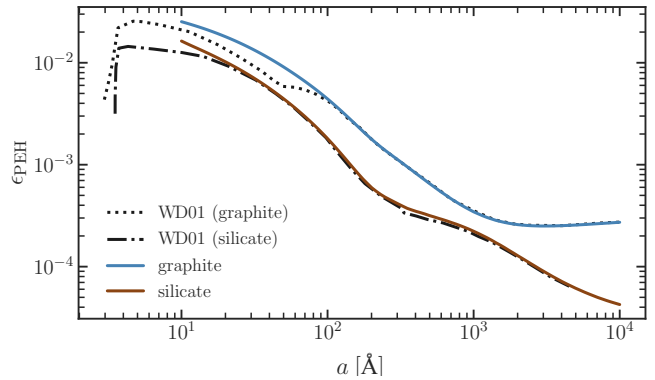


FIG. 4.—: Photo-electric net heating efficiency for graphite (blue line) and silicate (brown line) grains embedded in the [Mathis et al. \(1983\)](#) ISRF with the WNM phase conditions. Our modelling is in excellent agreement with the results of [Weingartner & Draine \(2001a\)](#) down to $a \lesssim 100 \text{ \AA}$ for graphite grains due to the different choice of optical properties in their work compared to CALIMA.

accretion rate onto dust is given by:

$$\dot{\rho}_{\text{acc},j} = \left(1 - \frac{\rho_{d,j}}{\rho_{z,j}}\right) \frac{\rho_{d,j}}{\tau_{\text{acc},j}}, \quad (8)$$

where the index j runs over each dust bin (small, large) and chemical species (silicate, carbonaceous), $\rho_{d,j}$ is the mass density of dust in bin j , and $\rho_{z,j}$ is the mass density of metals (combining gas and dust in bin j). The accretion timescale is written as:

$$(\tau_{\text{acc},j})^{-1} = \alpha \frac{\pi \bar{a}_j^2}{f_X m_{\text{gr},j}} \rho_X v_X, \quad (9)$$

where $m_{\text{gr},j}$ is the mass of a single grain of type j , α is the sticking coefficient, and $\pi \bar{a}_j^2$ is the effective grain cross-section, which considers the effect of Coulomb focusing ([Weingartner & Draine 1999](#)) with the factor F_C as $\pi \bar{a}_j^2 \equiv F_C \pi a_j^2$. The quantities ρ_X , v_X and f_X denote the gas-phase mass density, gas thermal velocity and fractional contribution of the *limiting* element X to the grain j composition. The concept of *limiting* element requires some care. In our current implementation for dust composition in CALIMA, the stoichiometry of a given dust species is kept fixed across the simulation. This does not complicate the treatment of accretion for amorphous carbonaceous grains, as for these $X = C$. However, when determining the accretion rate of the different elements that compose a silicate grain, we ensure that the increase in dust mass corresponds to a decrease in metal mass in order to keep the stoichiometry of a given grain fixed. This means that at a given time, the abundance of a particular element X contributing to the silicate composition may be lower and/or the element X may experience a lower interaction rate with the grain, hence *limiting* the final growth of mass by accretion. More specifically, we make use of the following ‘frequentist argument’: considering the average Maxwellian thermal velocity⁹ given

⁹ Reaction rates use the Maxwellian average because reactions depend on the full velocity distribution — especially the high-energy tail — not on the most probable particle speed.

by $v_X = (8k_B T / (\pi m_X))^{1/2}$, we compute the *limiting* element parameters for the accretion time-scale using:

$$\frac{\rho_X v_X}{f_X} = \left(\frac{8k_B T}{\pi} \right)^{1/2} \min \left[\frac{\rho_\ell}{f_\ell m_\ell^{1/2}} \right]_{\ell = \text{Mg, Fe, Si, O}}, \quad (10)$$

where ℓ runs over the gas elements that contribute to the silicate composition and m_ℓ is the atomic mass of element ℓ .

The effective grain cross-section includes the contribution from electrostatic interactions between ionised gas and dust grains and requires knowing a dust grain's charge acquired through many ISM processes. We use the results from Section 2.2 to compute on-the-fly GCDs. We obtain the local Coulomb focusing factor F_C (Weingartner & Draine 1999):

$$F_C(a, T, Q_k) = \sum_{Q_g} f(Q_g, a) B(Q_g, Q_k, a, T), \quad (11)$$

where the sum goes over each charge state present in the distribution of the grain charge Q_g , Q_k is the charge of the ion k and where (Draine & Sutin 1987):

$$B(Q_{g,i}, Q_k, a, T) = \begin{cases} \exp\left(-\frac{Q_g Q_k e^2}{k_B T a}\right), & \text{if } Q_g Q_k > 0, \\ \left(1 - \frac{Q_g Q_k e^2}{k_B T a}\right), & \text{if } Q_g Q_k < 0, \\ 1 + \left(\frac{\pi Q_k^2 e^2}{2k_B T a}\right), & \text{if } Q_g = 0. \end{cases} \quad (12)$$

In practice, we compute these accretion timescales for the individual metal ion populations as predicted by the non-equilibrium solver in RAMSES-RTZ, hence depleting individual ions. To conserve charge and to not be forced to include this charge influx to the computation of equilibrium dust charge distributions, we assume that any given accreted ion instantaneously recombines. This assumes that charging timescales are much faster than accretion timescales, which is a fair assumption for dust grains with $a \gtrsim 50 \text{ \AA}$ (see Figure 5 in Ibanez-Mejia et al. 2019). In Fig. 5 we show the value of F_C for ISM phases traditionally considered in dust charging models (see Table 1 in Weingartner & Draine 1999). As an example, we use an ion with $Q_k = 1$ (e.g. C^+ or Mg^+), such that we can compare with the values of the Coulomb correction factor presented in Figure 1 of Weingartner & Draine (1999), for the CNM, the WNM and the WIM (as defined in their work) ISM phases. We note that in Weingartner & Draine (1999) the dust optical properties followed Draine et al. (1984) and Laor & Draine (1993), without the modifications to the small graphitic grains and the suppression of the absorption feature in silicates introduced in Weingartner & Draine (1999) and Li & Draine (2001). This makes the comparison with their work on dust charging and photo-electric heating particularly challenging, as well as with our choice of optical properties. Despite this, our results seem to suggest similar trends as the original work in Weingartner & Draine (1999): small grains are either neutral or negatively charge in the cold phases of the ISM, resulting in positive attraction with positive ions and therefore $F_C > 1$, while big grains are easily stripped of many electrons in the ISRF, resulting in accretion being slowed

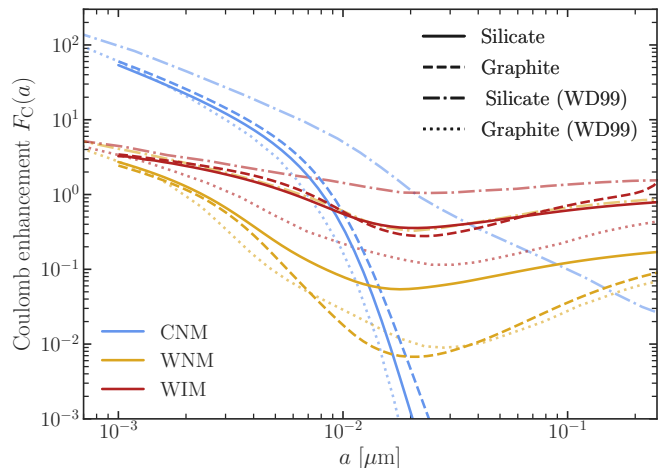


FIG. 5.—: Coulomb enhancement factor F_C as function of grain size for different ISM phases (CNM, blue; WNM, yellow; WIM, red) assuming a colliding ion with charge $Z_k = 1$. Solid-dashed and dotted lines correspond to the results of Weingartner & Draine (1999) for silicate and graphite, while solid and dashed correspond to our computed F_C for, respectively, silicate and graphite grains. Our results agree reasonably well with Weingartner & Draine (1999), except large deviations for silicate grains (see text for discussion).

down in the WNM and WIM, and completely halted in the CNM. As expected from different choice of optical properties for silicate grains, we find for this composition the largest discrepancy with Weingartner & Draine (1999). However, the size of this discrepancy in the CNM is concerning, because our results otherwise agree well with the charging model of Weingartner & Draine (2001a) (see Fig. A1 for the good agreement for large grains). This difference is unlikely to be driven by the adopted optical properties, which typically differ by no more than 20%. Instead, it appears to arise from their treatment of grain charging in the CNM: the large charge contrast between silicate and graphite grains that we obtain is not present in the CNM solutions of Weingartner & Draine (2001a) (see their figure 10). We therefore caution against using the plotted values of F_C from Weingartner & Draine (1999) without considering these limitations.

Efficient accretion occurs in the dense, cold phases of the ISM, which are barely reproduced by current cosmological galaxy simulations. In Dubois et al. (2024) they found that simulations with different maximum spatial resolution (from $\Delta x = 72 \text{ pc}$ to 9 pc resolution) led to a significant increase (up to a factor of 2) in the final DTM. This lack of numerical convergence for the DTM can be attributed to the lack of very cold and dense gas where accretion of metals from the gas phase is expected to be more efficient (see Eq. 9). To alleviate this problem, in Dubois et al. (2024), they employed a sub-grid model for the unresolved gas density similar to the one used in turbulence-driven star formation models (see e.g. Kimm et al. 2017). Sub-grid accretion is locally estimated by the gas density of the cell is actually the mean gas density \bar{n} of a log-normal PDF of gas densities shaped by

turbulence:

$$p(s) = \frac{1}{\sqrt{2\pi}\sigma_s} \exp\left(-\frac{(s-s_0)^2}{2\sigma_s^2}\right), \quad (13)$$

where $s = \ln(n/\bar{n})$, $s_0 = -\sigma_s^2/2$ and $\sigma_s = \ln(1 + b^2\mathcal{M}^2)$, with b the compression ratio (we take $b = 0.4$ for a mixture of compressible and solenoidal turbulence which is the same value later used in the for the star formation efficiency, see section 4) and \mathcal{M} the turbulent Mach number. The effective accretion timescale $t_{\text{acc,eff}}$ is obtained by integrating the mass accretion rate over the log-normal PDF for a given set of mean density, temperature and metallicity $(\bar{n}, \bar{T}, \bar{Z})$, hence:

$$\frac{t_{\text{acc}}(\bar{n}, \bar{T}, \bar{Z})}{t_{\text{acc,eff}}} = \int_{-\infty}^{s_{\text{max}}} \frac{t_{\text{acc}}(\bar{n}, \bar{T}, \bar{Z})}{t_{\text{acc}}(n, T, Z)} \frac{n}{\bar{n}} p(s) ds, \quad (14)$$

up to a maximum density $s_{\text{max}} = \ln(n_{\text{max}}/\bar{n})$, where the maximum density is $n_{\text{max}} = 10^4 \text{ H cm}^{-3}$, i.e. the density where grains start to be significantly coated with a water ice mantle ($n \geq 10^3 \text{ H cm}^{-3}$, Cuppen & Herbst 2007; Hollenbach et al. 2008; Lamberts et al. 2014; Elyajouri et al. 2024) which suppresses the accretion of refractory material onto the grain surface. This unresolved density distribution should also give rise to an unresolved temperature and gas metal density distribution. However, there is no simple correspondence between these three random fields. Instead, we assume that the average metal fraction and temperature are those given by the local value of these quantities (i.e. $T = \bar{T}$ and $n_X/n_H = \bar{n}_X/\bar{n}_H$). This leads to:

$$\begin{aligned} \frac{t_{\text{acc}}(\bar{n}, \bar{T}, \bar{Z})}{t_{\text{acc,eff}}} &= \int_{-\infty}^{s_{\text{max}}} \exp(2s) p(s) ds \\ &= \frac{e^{\sigma_s^2}}{2} \text{Erfc}\left(\frac{3\sigma_s^2/2 - s_{\text{max}}}{\sqrt{2}\sigma_s}\right), \end{aligned} \quad (15)$$

where Erfc is the complementary error function.

Many different expressions have been suggested in the literature for the sticking coefficient $\alpha(T)$ (see the discussion in Zhukovska et al. 2016), but much of our knowledge of the sticking probability of gas phase atoms onto grain surfaces is based on the physical-chemistry modelling and experiments that have studied the sticking of H atoms to form molecular hydrogen either by the Langmuir-Hinshelwood or the Eley-Rideal mechanisms (see e.g. Chaabouni et al. 2012; Le Bourlot et al. 2012; Bron et al. 2014, but also Section 2.10). It remains unclear how heavier atoms (that are also found in different ionisation states in the ISM) stick to surface grains, which has resulted in one-zone models simplifying the problem by assuming $\alpha = 1$ (e.g. Asano et al. 2013; McKinnon et al. 2016; Vogelsberger et al. 2019; Li et al. 2019; Lewis et al. 2022; Choban et al. 2022; Hu et al. 2023, either at all T or only for a range of low temperatures $\lesssim 300 \text{ K}$). Zhukovska et al. (2016) have shown that using a fixed value of $\alpha = 1$ tends to over predict the depletion of gas-phase metals in the Galactic ISM, and instead argues that a lower value of $\alpha = 0.3$ is more appropriate to match current constraints of metal depletion (e.g. Jenkins 2009). We identify the choice of $\alpha(T)$ as a significant source of uncertainty in our model (as it has been for previous implementations of dust evolution in one-

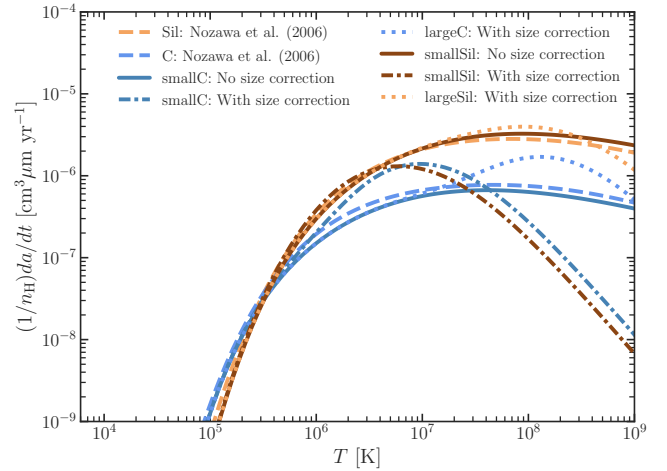


FIG. 6.—: Erosion rate (i.e. $(da/dt)/n_H$) by thermal sputtering given by Eq. A6 for each dust species. These have been computed for a gas composition of $Z = 10^{-4}Z_\odot$. We compare the results of Nozawa et al. (2006) to our updated model that considers the finite size of the grain for the effective energy deposited by ions. This results in small grains being less sputtered for $T \sim 10^7 \text{ K}$.

zone models and hydrodynamical simulations Hirashita & Kuo 2011; Grassi et al. 2014; Zhukovska et al. 2016; Aoyama et al. 2017; Gjergo et al. 2018) and leave the sticking coefficient as a free parameter. Sticking coefficients values we explored are detailed in appendix D of Dubois et al. (2024).

2.5. Thermal sputtering

Dust particles in high temperature coronal gas are subject to the destructive effect of collisions with fast moving ions. If the kinetic energy of the collision is sufficiently large, the energy of a dust grain may be able to overcome the dust grain binding energy. This process of sputtering is capable of removing a large fraction of the dust grain mass in high temperature gas and is hence of high importance for the hot phase DTM. We follow a derivation similar to the one outlined in Kirchschrager et al. (2019), which is similar to the original approach in Tielens et al. (1994) but considers the finite size a of the target dust grain and the effect of grain charge in the interaction energy. Our implementation is detailed in Appendix A.1, where we have modified previous theoretical derivations by using more updated atomic experimental data and by considering more appropriate theoretical modelling for these sub-relativistic ion-solid interactions.

In order to compare to the rates obtained by Nozawa et al. (2006), we have computed thermal sputtering for a gas with $10^{-4}Z_\odot$ (see Fig. 6). Our vanilla rates (solid brown and blue lines) closely follow the shape and absolute values obtained by Nozawa et al. (2006) (dashed orange and blue lines), confirming the higher sputtering yield predicted for silicate grains compared to carbonaceous. When the finite size correction is applied (dotted lines), our large and small grain rates deviate from each other at temperatures above $\sim 10^6 \text{ K}$, resulting in rates that clearly peak at different temperatures. The

¹⁰ Across this work we assume the Asplund et al. (2009) solar metallicity value of $Z_\odot = 0.01345$.

most remarkable result of these updated erosion rates is their decrease by $\gtrsim 2$ dex and $\gtrsim 1$ dex for small and large grains above 5×10^7 K. This could have a significant effect on the sputtering timescale of dust grains in SN and shock heated X-ray gas within galaxy clusters (Vogelsberger et al. 2019). We pre-compute these rates for individual ions for each grain species and size, allowing on-the-fly interpolation to determine the combined sputtering rates of the ions followed in RAMSES-RTZ.

2.6. Gas collisional cooling/heating

So far, we have not explicitly detailed the direct collisional transfer of energy between dust grains and gas atoms. In Section 2.5, we introduced how high velocity collisions that take place at high temperature cause sputtering of atoms from dust grains. This fragmentation reaction takes place via the transfer of thermal energy of the gas to the internal energy of the grain, which effectively means an additional source of cooling for gas enriched with dust. Collisional heating may be an important source of dust heating (gas cooling) in high density shocks, which could explain the infrared-to-X-ray (IRX) relation observed for SNRs in the Galaxy and the LMC (e.g. Graham et al. 1987; Seok et al. 2015). Furthermore, in highly obscured dense regions, collisional heating significantly impacts the equilibrium temperature of dust grains (Hollenbach & Mckee 1989; Glover & Jappsen 2007; Dopcke et al. 2011). Dust-gas collisional cooling has been implemented in various ISM chemistry models (e.g. Wolfire et al. 2003; Grassi et al. 2014; Krumholz 2014; Bialy & Sternberg 2019; Kim et al. 2023; Katz et al. 2022) and hydrodynamical simulations with explicit dust modelling (e.g. Vogelsberger et al. 2019; Granato et al. 2021; Dubois et al. 2024). Models of dust cooling are primarily based on the seminal work by Hollenbach & Mckee (1979) and Dwek & Werner (1981), and indeed the high-temperature dust-electron collisional cooling in our original dust model for RAMSES (Dubois et al. 2024) is based on a fitting function provided in Appendix A of Dwek & Werner (1981). However, we would like to emphasise that these models have been applied, within the ISM and galaxy formation community, with little scrutiny as to the extent of their applicability. In Appendix A.2 we review these aspects and propose a more appropriate modelling of dust-grain collisional cooling.

For the low temperature regime ($T \lesssim 10^4$ K), we use the *soft cube* model from Burke et al. (1974), which is implemented for dust collisional cooling in shocks by Hollenbach & Mckee (1979). The prediction of this model for our small silicate grains ($a = 0.005 \mu\text{m}$) is shown in Fig. 7 for H (dashed blue line) and He (dotted blue line) collisional partners. The quantity h (Eq. A28) in Fig. 7 encapsulates the efficiency of energy transfer in individual grain-atom collisions. As we argue in Appendix A.2, the *soft cube* model is only applicable for neutral atoms and low energies for which the interaction is limited to inelastic collisions with the grain surface. For hot ionised gas ($T > 10^4$ K), we instead need to consider the energy deposited by atoms that penetrate the grain material. This is the regime of interactions developed by Dwek & Werner (1981) and that we have updated for CALIMA in Section 2.5. Therefore, for ionised gas we simultaneously predict the gas cooling due to ion-grain collisions and the consequent the sputtering of grain material. We show the

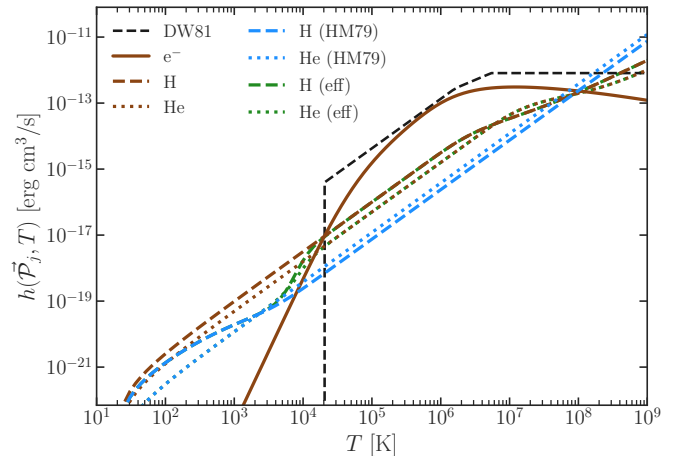


FIG. 7.— Collisional cooling efficiency h as defined by Eq. A28 for small silicate ($a = 0.005 \mu\text{m}$) at different gas temperatures, and computed for electrons (solid brown line), H (dashed brown line), and He (dotted brown line). We compare our results to the model at low temperature from Hollenbach & Mckee (1979) for H (dashed blue line) and He (dotted blue line), and at high temperature cooling from electrons by Dwek & Werner (1981) (dashed black line). To transition between the neutral and ionised gas regimes, we apply a logistic smoothing at $T \sim 10^4$ K represented by the green lines (dashed for H and dotted for He).

results of this computation in Fig. 7 for small silicate grains considering electrons (solid brown), H (dashed brown) and He (dotted brown). We compare our electron cooling efficiency to the fitting equation from Appendix A in Dwek & Werner (1981) (dashed black line), which is the main cooling agent in previous works (e.g. Vogelsberger et al. 2019; Granato et al. 2021; Dubois et al. 2024). Our treatment of finite grain size results in deviations from their modelling at high temperature, while the correct treatment of low energy collisions allows us to extend the efficiency to lower temperature than the limit imposed in Dwek & Werner (1981).

Inversely to the *soft cube* model, the hard-sphere regime of ion collisions is not applicable for sufficiently low energy collisions that result in minimal grain penetration. Therefore, we adopt a combination of the *soft cube* model and the high-energy collisional cooling by means of a smoothly transitioning from one to the other using a logistic factor at $T \sim 10^4$ K in logarithmic space with width of 10. We show how this appears in practice for H and He collisions with the dashed and dotted green lines in Fig. 7.

2.7. Non-thermal sputtering in SN shocks

SNe (type II and Ia) destroy dust already present in the ISM, where the dust destruction is produced by inertial (non-thermal) sputtering and grain-grain collisions (Kirchschlager et al. 2020; Vasiliev 2025; Vasiliev & Nath 2025). As opposed to thermal sputtering, non-thermal sputtering is independent of temperature, and the energy of the collision is instead related to the kinetic energy imparted by a travelling shock wave in the ISM (i.e. a SN shock). The amount of SN-destroyed dust $\Delta M_{\text{SN},j}$ is a fraction of the mass of gas M_{100} shocked to

velocities above 100 km s^{-1} defined as

$$\Delta M_{\text{SN},j} = \varepsilon_{\text{SN}}(a_j) \min\left(\frac{M_{100}}{M_{\text{gas}}}, 1\right) M_{\text{d},j}, \quad (16)$$

with a size-dependent destruction efficiency given by [Aoyama et al. \(2020\)](#) (their equation 11):

$$\varepsilon_{\text{SN}}(a_j) = 1 - \exp\left(-\frac{\delta_{\text{SN},j}}{a_{0.1,j}}\right), \quad (17)$$

and M_{gas} is the gas mass in the current cell, $M_{\text{d},j}$ the local dust mass in bin j , $a_{0.1,j}$ the dust grain size in units of $0.1 \mu\text{m}$, and $\delta_{\text{SN},i}$ the destruction efficiency. Small grains are more efficiently decelerated by drag forces, trapping them near the shock region where, opposite to large grains, thermal sputtering can quickly destroy them ([Nozawa et al. 2006](#)). The dependence of the destruction efficiency Eq. 17 on grain size a reflects this. The mass of shocked gas is determined by the Sedov solution in a medium of homogeneous gas density (i.e. $M_{100} = 6800 E_{\text{SN},51} M_{\odot}$ [McKee et al. 1989](#)), where $E_{\text{SN},51}$ is the energy of the SN explosion in units of 10^{51} erg. Multiple SNe occur in one time step Δt (each individual SN engulfing the gas swept up by the previous explosion), following (see [Hou et al. 2017](#)):

$$\Delta M_{\text{SNe},j} = \left[1 - \left(1 - \frac{\Delta M_{\text{SN},j}}{M_{\text{d},j}}\right)^{N_{\text{SN}}}\right] M_{\text{d},j}, \quad (18)$$

with N_{SN} the number of SNe. We emphasise that in this model the SN blast wave does not destroy the dust newly formed in stellar ejecta. It only destroys pre-existing dust: the dust condensation efficiency (see Section 2.1) implicitly takes this into account.

We use a different value of the dust destruction efficiency for carbonaceous (0.10) and silicate (0.15) grains, following results from hydrodynamical simulations of dust sputtering in a turbulent multiphase ISM ([Hu et al. 2019](#)), where approximately 50 percent more silicate grains are destroyed than carbonaceous grains. Grain-grain collisions in shocks could also lead to efficient shattering of large grains into small grains (e.g. [Jones et al. 1996](#); [Nozawa et al. 2006](#); [Serra Díaz-Cano et al. 2008](#); [Bocchio et al. 2014](#); [Slavin et al. 2015](#); [Kirchschlager et al. 2021](#)). It has been argued that this shattering in SN shocks could allow for the formation of large PAH clusters ($< 15 \text{ \AA}$) from up to $\sim 10\%$ of the carbon dust in shocks with $v_s \sim 100 \text{ km s}^{-1}$ ([Jones et al. 1996](#)). Nevertheless, there is still little evidence for the formation of very small grains in SN shocks (see e.g. [Tielens 2008](#), for a discussion of the problem), and it is not clear how much of these new small grains will survive in the hot post-shock gas. CALIMA therefore allows for different small grain production efficiencies in SN shocks, leaving them as free parameters of the model.

2.8. Turbulent shattering of large grains

As particles suspended in gas, dust grains experience collisions and mixing in the turbulent ISM (see e.g. [McKee & Ostriker \(2007\)](#); [Elmegreen & Scalo \(2004\)](#) for reviews about the presence of turbulence in the ISM). Close-range interactions can lead to elastic collisions or can compromise the physical integrity of dust grains, by

deformations, coagulation or shattering. In this section we begin by detailing how large energy collisions can cause grains to shatter into smaller fragments, strongly altering their size distribution and, consequently, the extinction curve. Small grains account for the majority of the cross-sectional area of the dust distribution, and thus they are of great importance to modelling the dust-radiation coupling as well as the chemistry on the surface of grains (e.g. H_2 formation). Hence the top-down processing of the dust distribution from large grain to their transformation into small grains, ultimately including PAHs, cannot be neglected in a dust model for galaxy formation (e.g. [Seok et al. 2014](#); [Narayanan et al. 2023](#)).

The statistical properties of magnetised, compressible gas turbulence are fundamental for determining the motion of dust grains. The dynamics of grains is primarily driven by hydrodynamic drag and Lorentz force acceleration. Efficient dust grain acceleration (against damping mechanisms) occurs via gyroresonance when the Doppler-shifted frequency of the fast magnetosonic wave in the frame of reference of the grain is a multiple of the gyrofrequency of the grain in the local magnetic field. In the original work of [Yan et al. \(2004\)](#) (see [Lazarian & Yan 2001](#); [Yan & Lazarian 2002](#), for the theoretical MHD turbulence framework), large grains ($a \geq 0.2 \mu\text{m}$) can decouple from the turbulent flow in the WNM (due to a higher ratio of stopping time to flow characteristic time, i.e. Stokes' number) and be accelerated to $\sim 1 \text{ km s}^{-1}$, (i.e. above the shattering threshold) by the Lorentz force ([Jones et al. 1996](#)). However, the computations in [Yan et al. \(2004\)](#) are limited to grains with $a \geq 0.01 \mu\text{m}$, and to specific thermodynamical conditions rather than the full multiphase conditions that arise in realistic galaxy formation simulations. Full modelling of dust dynamics in MHD turbulence remains a difficult problem (e.g. [Fromang & Nelson 2009](#); [Zhu et al. 2015](#); [Lee et al. 2017](#); [Commerçon et al. 2023](#)), and translating the results of simulations where the large grain decoupling is resolved ($\ll 0.01 \text{ pc}$) to galactic scales simulations without magnetic fields is not a trivial task. We leave further developments of the dust and MHD coupling within the RAMSES code (see e.g. [Lebreuilly et al. 2019](#); [Moseley et al. 2022](#); [Commerçon et al. 2023](#); [Moseley & Teyssier 2025](#), for current efforts) to future work.

Instead, we follow the purely HD formulation of turbulent-induced collision velocities for dust grains by [Ormel & Cuzzi \(2007\)](#) and the fragmentation modelling by [Kobayashi & Tanaka \(2010\)](#) with the material properties of [Jones et al. \(1996\)](#) (see Appendix A.3 for further details).

2.9. Turbulent coagulation of small grains

When two grains collide at sufficiently low velocities, they can fuse together, coagulating into a larger grain. In CALIMA we consider both the coagulation of small grains to form large grains, and the coagulation of small and large grains. The process of dust grain coagulation has been invoked to explain the lack of small grains contributing to the $60 \mu\text{m}$ emission at ISM gas densities $\gtrsim 10^3 \text{ cm}^{-3}$ (e.g. [Stepnik et al. 2003](#); [Roy et al. 2012](#)) and the flattening of the extinction curve in the near-IR and mid-IR (e.g. [Moore et al. 2005](#); [Foster et al. 2013](#); [Li et al. 2023](#)). Coagulation has been extensively explored in the study of proto-stellar core collapse ([Ormel et al.](#)

2009; Guillet et al. 2020; Marchand et al. 2021; Kawasaki et al. 2022b; Lebreuilly et al. 2022) with the unanimous conclusion that dust grains grow by coagulation in high density gas. Previous models including coagulation (e.g. Chokshi et al. 1993; Hirashita & Yan 2009; Aoyama et al. 2017; Yan et al. 2004) assume that coagulation between grains i and j only takes place below a threshold velocity

$$v_{\text{coa}}^{ij} = 21.4 \left[\frac{a_i^3 + a_j^3}{(a_i + a_j)^3} \right]^{1/2} \frac{\gamma^{5/6}}{E^{1/3} R_{i,j}^{5/6} s^{1/2}}, \quad (19)$$

above which bouncing (i.e. elastic collision) will be the end result of the collision. Again, a_i and a_j are the radii of target and projectile grains. This expression depends on a series of material properties of the dust grains (see Table 3 of Chokshi et al. 1993, for the values of γ , the grain material surface energy per unit area, $R_{ij} = a_i a_j / (a_i + a_j)$, the reduced radius of the grains, and E , which is related to the Poisson’s ratios and Young’s modulus of the grain material). Experimental studies with micron-size silica spheres (Poppe et al. 1997) have shown that there is a sharp transition velocity from coagulation to grain bouncing, but the estimate from Eq. 19 is 4 times lower than what is expected for grains with icy mantels. Consistent with our maximum density $n_{\text{H}} = 10^4 \text{ cm}^{-3}$ for accretion of refractory materials limited by the formation of icy mantles (see Section 2.4), we consider that above a $n_{\text{H}} \geq 10^4 \text{ cm}^{-3}$ water, CO and CH₄ ices freeze on the surfaces of dust grains (Hollenbach et al. 2008; Silsbee et al. 2021). Therefore, we increase the velocity threshold for coagulation by a factor of 4 (Guillet et al. 2020) compared the one predicted by Eq. 19. Similar to the shattering timescales, we compute coagulation timescales using the models for the relative collision velocities from Appendix A.3. Additionally we also apply the un-resolved turbulence enhancement of the gas density¹¹ as done for accretion (see Section 2.4).

Instead of abruptly shutting off coagulation when $\Delta V_{ij} > v_{\text{coa}}$, we apply a sigmoidal smoothing that returns a maximum t_{coa} of 10^5 Myr (i.e. one order of magnitude larger than the Hubble time) in order to effectively stop coagulation. Previous works (e.g. Asano et al. 2014) have shown that the extinction curve of the MW cannot be explained by a sharp cutoff in coagulation.

2.10. Molecular hydrogen formation on dust surfaces

Molecular hydrogen is the most abundant molecule in the Universe (e.g. Fraser et al. 2002; Bolatto et al. 2013). It strongly influences the thermal state of star-forming gas as well as the formation of other molecules in the ISM. While primordial H₂ formation plays a dominant role in the dust-free formation of the first stars (e.g. Abel et al. 2000; Abel et al. 2002), H₂ is believed to be primarily formed via catalytic reactions on dust grain surfaces. The consistent, on-the-fly modelling of H₂ formation on dust grains is then one of the strengths of CALIMA. We follow the modelling of molecular hydrogen formation developed by Cazaux & Tielens (2002, 2004) through the

¹¹ In the vanilla dust model for RAMSES that we have presented in Dubois et al. (2024) we do not consider the un-resolved density PDF. Instead, we assume that half the gas mass above $n_{\text{H}} > 10 \text{ cm}^{-3}$ has an actual density of 10^3 cm^{-3} .

Langmuir-Hinshelwood and the Eley-Rideal processes. In practice, we compute the contribution of each grain size bin to the total local formation rate of molecular hydrogen, considering the on-the-fly dust temperature T_{d} . We use the physical parameters for olivine silicate surfaces and amorphous graphite given by Cazaux et al. (2004), which are themselves derived from the experimental results from laboratory irradiation of grain surfaces performed in Pirronello et al. (1996); Pirronello et al. (1997); Pirronello et al. (1999). We emphasise that the self-consistency in dust-mediated H₂ formation is a singular feature of CALIMA, compared to efficiencies usually fixed to an empirically derived value for the MW Wolfire et al. (e.g. 2008); Gnedin et al. (e.g. 2009).

2.11. Dust optical properties

We use the optical properties for graphite and “UV smoothed” astronomical silicates by Draine et al. (1984) (see also Laor & Draine 1993; Weingartner & Draine 2000)¹² for our carbonaceous and silicate grains. The total local dust optical depth is given by:

$$\tau(\lambda) = L \sum_i C_{\text{ext},i}(\lambda) n_{\text{d},i}, \quad (20)$$

where L is the path length for light propagating through a medium of dust density $n_{\text{d},i}$, $C_{\text{ext},i}$ is the wavelength dependent extinction cross-section, and the sum is over dust components (large, small, silicate, carbonaceous grains, PAHs, etc.).

Based on these optical properties, we can derive the dust temperature T_{d} in the equilibrium approximation using the local radiation properties¹³. Ignoring the small amount of energy that goes into luminescence or photoelectrons for regular grains (e.g. Weingartner & Draine 2001a), the heating rate of a grain by absorption of radiation is:

$$\frac{dE_{\text{abs}}}{dt} = \int \frac{u_{\nu} d\nu}{h\nu} ch\nu C_{\text{abs}}(\nu), \quad (21)$$

where $\frac{u_{\nu} d\nu}{h\nu}$ is the number density of photons with frequencies in the range $[\nu, \nu + d\nu]$ for the radiation field energy density u_{ν} . In practice, we compute a spectrum-averaged¹⁴ absorption cross-section for each radiation bin j in RAMSES-RTZ:

$$\bar{C}_{\text{abs},j} = \frac{\int_{\lambda_{\text{min}}^j}^{\lambda_{\text{max}}^j} \lambda C_{\text{abs}}(\lambda) u_{\lambda} d\lambda}{\int_{\lambda_{\text{min}}^j}^{\lambda_{\text{max}}^j} \lambda u_{\lambda} d\lambda}, \quad (22)$$

¹² We use the publicly available optical properties from Bruce T. Draine’s personal website (<https://www.astro.princeton.edu/~draine/dust/dust.diel.html>).

¹³ This is only performed for regular dust grains, while PAH photo-heating is described in Section 3.9 within the description of photo-dissociation

¹⁴ This is based on the stellar-polling approximation in RAMSES-RT, which recomputes the average spectrum in each radiation bin at every coarse timestep by performing a weighted average over all stellar sources in the simulation volume (e.g. Rosdahl et al. 2018). In the case of including radiation from other bright sources with very different spectrum to the dominant stellar emission (e.g. the active galactic nuclei radiation from the accretion disc of a supermassive black hole) this approximation may fail in capturing the effective radiation field near the secondary source, and would require the use of photon tracer algorithms (e.g. Trebitsch et al. 2021).

where the integral is over the minimum λ_{\min}^j and maximum λ_{\max}^j wavelengths covered by radiation bin j . The energy loss due to IR emission is given by:

$$\frac{dE_{\text{em}}}{dt} = \int d\nu 4\pi B_\nu(T_d) C_{\text{abs}}(\nu), \quad (23)$$

with B_ν being Planck's blackbody function. To simplify this calculation at runtime, we can compute a Planck-averaged emission efficiency defined as:

$$\bar{C}_{\text{abs},T_d} = \frac{\int d\nu B_\nu(T_d) C_{\text{abs}}(\nu)}{\int d\nu B_\nu(T_d)}, \quad (24)$$

which allows us to write the IR emission rate as:

$$\frac{dE_{\text{em}}}{dt} = 4\bar{C}_{\text{abs},T_d} \sigma_{\text{SB}} T_d^4, \quad (25)$$

with σ_{SB} the Stefan-Boltzmann constant. With these simplifications, we can determine the steady state temperature for grain bin i (Draine 2011) based on the balance of absorbed energy for all radiation bins (below the Lyman limit of 13.6 eV) and collisional heating sources (Eq. A18 and A27, see Section 2.6):

$$4\bar{C}_{\text{abs},T_{d,i}} \sigma_{\text{SB}} T_{d,i}^4 = \sum_j \bar{C}_{\text{abs},i,j} u_j c + \sum_k H_{\text{coll},k}(\vec{P}_j, T, n_k) \quad (26)$$

where k loops over all gas species contributing to the collisional heating and \vec{P}_j is the vector of grain material properties (see Eq. A27 for the expression of H_{coll}) and:

$$u_i = \int_{\lambda_{\min}^i}^{\lambda_{\max}^i} \lambda u_\lambda d\lambda. \quad (27)$$

We set a floor for the dust temperature given by the current CMB temperature ($T_{\text{CMB}}(z)$) at redshift z .

3. POLYCYCLIC AROMATIC HYDROCARBONS IN GALAXY FORMATION

In this section we detail our extension of the two-size grain approximation to account for the properties of very small particles containing C atoms: PAHs. By computing the ratio of flux in IR emission features (attributed to PAHs) to the far-IR flux, one can obtain the fraction of UV flux that is absorbed by PAHs and, by adopting standard dust parameters (Allamandola et al. 1989), predict the fraction of C locked in different PAHs. We again follow the modified log-normal distribution in Section 2 for each PAH bin. The original small carbonaceous (small C) grains centroid of $5 \times 10^{-3} \mu\text{m}$ (as in Dubois et al. 2024) has been displaced to $1 \times 10^{-2} \mu\text{m}$ to account for the higher discretisation of very small grains allowed by our two PAH bins. Our choice of PAH centroids is based on the abundance constraints of the MW SED (Allamandola et al. 1989; Draine & Li 2007) in resemblance to Table 2 in Tielens (2008). We separate traditional PAHs (composed here of $N_C = 54$ carbon atoms per PAH corresponding to circumcoronene) that are photolytically stable in the ISM (Guhathakurta et al. 1989) from large PAH clusters (here $a = 10 \text{ \AA}$, i.e. $N_C = 418$), which contribute to the emission plateau underlying the IR emission features Tielens (2008). The effective radius

a of a PAH molecule is given by Equation 8 in Draine et al. (2021):

$$a = 10 \left(\frac{N_C}{418} \right)^{1/3} \text{ \AA}. \quad (28)$$

3.1. PAH optical properties

For flexibility, we use the optical properties for PAHs derived by Li & Draine (2001) and publicly available¹⁵, allowing us to obtain GSD-averaged cross-sections for any choice of PAH centroid a_0 (see Eq. 1). The intrinsic spectral properties of PAHs vary primarily because of their ionisation state (the $3.3 \mu\text{m}$ is reduced in ionised PAHs, and the features at the 11-15 μm are considerably boosted Bauschlicher et al. 2008) and the size of the molecule (contribution to the mid-IR plateau increases with increasing size, and the peak position of the major bands becomes more stable, see Hudgins et al. 1999; Bauschlicher et al. 2008). The optical properties in Li & Draine (2001) allow us to capture these changes in the strength of the different features and the scale of the mid-IR continuum with different charge states and sizes.

3.2. PAH seeding

There is tentative evidence for the formation of PAHs in carbon-rich AGB stars (Allamandola et al. 1989; Sloan et al. 2007; Smolders et al. 2010; Matsuura et al. 2014; Sloan et al. 2017). However, observations are not uniform in their estimated production efficiencies, since the detections are only in post-AGB phases or in binary systems where there is enough UV flux to excite the PAH molecule. Despite this, these estimates appear to suggest that AGB stars do not deplete more than a few percent of their carbon in PAHs. Theoretical modelling of PAH formation in winds was pioneered in Frenklach et al. (1989) and Cherchneff et al. (1992), with predictions suggesting that it is only efficient in the narrow temperature window between 900 and 1100 K. However, the predicted efficiency was confined to $10^{-5} - 10^{-4}$ of their carbon production, orders of magnitude lower than the observed abundances. Even when considering more complex and realistic wind models (Cau 2002), these estimates reach at most 3.3×10^{-3} . Wolf-Rayet binaries have also been observed to show the distinctive mid-IR aromatic features attributed to PAHs (e.g. Marchenko & Moffat 2017; Taniguchi et al. 2025). However, their PAH formation efficiencies are even more uncertain than for AGB stars, since yields are highly dependent on companion presence, wind mixing, and local physical conditions. We leave an exploration of PAH seeding mechanisms for future work, and just assume a condensation efficiency of 3.3×10^{-3} for C-rich AGB winds and equally shared in mass fraction between small and large PAHs.

3.3. PAH growth

The formation of PAHs directly from the gas phase probes the molecular origins of these interstellar particles. The theoretical foundations of bottom-up PAH formation originate in combustion chemistry (see the mechanistic review by Altarawneh & Ali 2024), where

¹⁵ Again, from B. T. Draine's personal website (<https://www.astro.princeton.edu/~draine/dust/dust.diel.html>).

the formation of soot in hydrocarbon flames was extensively studied from the 1970s onward (e.g. Frenklach et al. 1989; Frenklach 2002). These studies showed that aromatic rings could form efficiently from small hydrocarbons (e.g. acetylene) through radical-driven reaction sequences activated at high-temperature ($T \sim 10^3$ K), moderate-density conditions, as was expected for carbon-rich AGB stellar winds (see Section 3.2).

As these models matured (e.g. see the review by Reizer et al. 2022), several distinct bottom-up mechanisms were identified, each predicting efficiencies that depended differently on the local temperature, UV field, and ionisation state. The most widely explored pathway is the hydrogen abstraction-acetylene addition (HACA) mechanism, in which the PAH growth happens via continuous abstraction of peripheral hydrogen atoms followed by accretion of C_2H_2 (e.g. Frenklach et al. 1989; Cherchneff et al. 1992; Richter & Howard 2002). However, the effectiveness of the HACA mechanisms is limited to high gas temperatures ($T \sim 10^3$ K) and densities ($n_H \sim 10^9 - 10^{11} \text{ cm}^{-3}$), which propelled a search for alternative growth mechanisms that could be more appropriate for ISM gas conditions. One such alternative is the hydrogen abstraction-vinylacetylene addition (HAVA) mechanism, which replaces acetylene with C_4H_4 , enabling faster ring growth per reaction cycle (Zhang et al. 2010; Parker et al. 2012; Liu et al. 2019; Zhao et al. 2018). The HAVA* further extends this pathway by reducing the reaction barrier thanks to vibrationally or electronically excited radicals (Shukla & Koshi 2012; Zhao et al. 2018). In parallel, laboratory cross-beam experiments demonstrated that radical-radical reactions between PAH compounds, summarised under the phenyl addition cyclisation framework (Shukla et al. 2008; Shukla & Koshi 2010; Zhang et al. 2025), can drive efficient PAH growth through largely barrier-less pathways. These developments significantly broadened the parameter space for bottom-up PAH formation, suggesting that PAH growth could occur not only in hot circumstellar envelopes, but also in cooler, UV-irradiated or shock-processed regions of the ISM. Recent JWST observations, including results from the PDRs4All program (ID 1288), reveal tight spatial correlations between PAHs, C_2H , and excited H_2 in PDRs and molecular interfaces, providing strong empirical support for radical-mediated growth channels (e.g. Goicoechea et al. 2025; Khan et al. 2025).

Observations of the Taurus Molecular Cloud (TMC-1) have been of particular relevance to the understanding of radical-mediated PAH growth mechanisms (e.g. Burkhardt et al. 2021; Cernicharo et al. 2021a; McGuire et al. 2021; Wenzel et al. 2024, 2025; Cabezas et al. 2025). Cyclopentadiene (e.g. Cernicharo et al. 2021b; McCarthy et al. 2021; Kelvin Lee et al. 2021) and benzene have been abundantly detected in TMC-1 (e.g. McGuire et al. 2018; Loru et al. 2023), molecules, with respectively $N_C = 5$ and 6, that are considered building blocks in the formation of larger aromatic molecules. However, astrochemical models still predict too-low abundances for many of the PAH precursors (e.g. McGuire et al. 2021; Cernicharo et al. 2022; Mallo et al. 2025), and fundamental intermediate products in the formation sequence to cyclopentadiene and benzene have not been observed yet (e.g. 1,3-butadiene Agundez et al. 2025). Furthermore,

these routes to the formation of benzene have been recently challenged by laboratory experiments (Koehler et al. 2025), leaving the issue of bottom-up PAH formation an unsolved problem at the time of writing (e.g. Loison et al. 2025). Given these large uncertainties, we do not explore a direct coupling of astrochemical models of PAH precursors with CALIMA in this work and leave this exploration for future work.

We instead opt by following the simpler approach of direct C accretion onto pre-existing PAHs. In previous works that have predicted the PAH mass fraction via aromatisation of carbonaceous grains (Rau et al. 2019; Hirashita & Murga 2020; Narayanan et al. 2023), this takes place following the same framework as was considered for regular dust grains (see e.g. Section 2.4). Experiments have shown that C^+ accretion can be fairly efficient (Canosa et al. 1995), but if not balanced by an efficient process of C desorption from the PAHs could lead to the almost complete depletion of interstellar C within a few Myr (e.g. Snow et al. 2008; Omont & Bettinger 2021). In this work we have instead used the results from Omont et al. (2025) with respect to the photostability of [C-PAH] complexes: small anion and neutral PAHs have a 20% probability of accreting C^+ without releasing acetylene (Marciniak et al. 2021) if they are hydrogenated. The hydrogenation state is computed based on Section 3.10 and we also apply the sub-grid density enhancement from Section 2.4.

3.4. PAH sputtering

In the same manner as for classical dust grains, PAHs immersed in a hot gas experience frequent collisions with energetic ions. These collisions may impart sufficiently large energies to cause PAH molecular dissociation. The survival of PAHs in hot supernova gas remains a debated topic, with some observations presenting tentative evidence of PAH emission co-spatial with known SNRs (Reach et al. 2005; Tappe et al. 2006). Extra-galactic observations find that PAH emission follows ionised gas in starburst winds (McCormick et al. 2013; Bolatto et al. 2024). Therefore, understanding the processing of PAHs in hot gas is a fundamental step in modelling the PAH life-cycle within a realistic galactic environment. We follow the modelling of thermal sputtering of PAHs presented in Micelotta et al. (2010a), with a series of modifications and adaptations to our PAH model (see Appendix A.4). Our resulting sputtering rates are separated by electrons, H, He, C and O ions (dominant sputtering species), such that interpolated rates can be computed on-the-fly by CALIMA considering the effects of local ionisation states and abundances. We compute the sputtering timescale as:

$$\tau_{\text{sput}}(N_C) = \frac{N_C}{2R_{\text{elec}} + \sum_k (2R_e^k + R_n^k)}, \quad (29)$$

where electron excitations (either by electron collision R_{elec} or by nuclear collision R_e^k) are multiplied by 2 as each dissociation event leads to the ejection of two carbon atoms. The sum is over the k ions.

We also include non-thermal sputtering in SN shocks for PAHs, as we did for regular grains (Section 2.7). Again, we do not track the properties of individual shocks in CALIMA, but instead determine the amount of PAHs

destroyed based on the amount of gas mass shocked above 100 km s^{-1} (McKee et al. 1989). We use the results of Micelotta et al. (2010b) and assume that small PAHs are fully destroyed in all gas above 100 km s^{-1} , but only 50% of the large PAHs are destroyed. This lost mass is returned to the local carbon gas-phase density.

3.5. Photo-electric heating by PAHs

In Section 2.3 we introduced the physical process of photo-electric heating by classical dust grains. Within our PAH modelling, we can now extend this physical process into the molecular regime, by first considering a fundamental difference between large dust grains and very small grains. Since the absorption depth of far-UV radiation ($\sim 100 \text{ \AA}$) can be significantly smaller than the mean free path of emitted electrons, the free electron yield quickly decreases for large grains. Additionally, large grains easily acquire a positive charge (see Section 2.4), making it even harder for an electron to escape the electric potential of the grain. This means that in practice $\gtrsim 50\%$ of the PEH for an MRN-like GSD originates in grains with $N_C < 1500$ (Bakes et al. 1994), and grains larger than $a > 100 \text{ \AA}$ have a secondary contribution. Therefore, for a long time, PAHs have been recognised as fundamental contributors to the very small dust grain PEH (Verstraete et al. 1990). Recently, Berné et al. (2022) developed an updated model of the PAH contribution to the PEH using new molecular parameters from laboratory experiments and quantum mechanical calculations. They show that with only the contribution of small PAHs (i.e. circumcoronene, $N_C \sim 54$) one can reconcile the observed ratio of gas emission in the IR (by cooling lines like [CII] and [OI]) and the total IR emission also including the dust emission (Okada et al. 2013). We follow a modified version of the model in Berné et al. (2022) for the contribution to PEH by small and large PAHs (see Appendix A.5). The benefit of this approach is that solving for the PAH charge distribution is not as computational and memory expensive as for regular dust grains, allowing the full computation of the photo-emission, attachment and recombination network on-the-fly in CALIMA. Therefore, self-consistent PEH modelling of PAHs renders CALIMA as a unique tool for understanding the role of PAHs in coupling the sub-ionising UV radiation field with the thermal state of the gas in the ISM.

3.6. PAH clustering

The high polarisability of PAH molecules results in large van der Waals forces, providing a strong bonding force between aromatic planes of PAHs (Zacharia et al. 2004) and the formation of PAH clusters. We follow the dimerisation (or clustering) of small PAHs to form large PAH clusters in light of kinetic theory and the binding energy of monomers forming large carbon clusters (e.g. Rapacioli et al. 2005, 2006; Tielens 2021; Khabazipur & Eaves 2023). At low temperatures ($\sim 10 \text{ K}$)¹⁶, the collision energy is significantly smaller than the interaction energy, which implies that long-lived compounds easily

form in the interaction, allowing for the PAH monomers to re-arrange into the most energetically favoured orientations (in the case of circumcoronene monomers stacking generally yields the most stable cluster; Rapacioli et al. 2005). However, if the collision imparts too much energy to the system, monomer evaporation may occur before this re-orientation can take place. We extend the above rates by considering a variable sticking efficiency C_{eff} fitted to numerical results in Figure 10 of Totton et al. (2012):

$$C_{\text{eff}}(T) = \frac{1}{1 + A[\log_{10}(T)]^B}, \quad (30)$$

where the fitting parameters are $A = 9.928 \times 10^{-7}$ and $B = 1.38$. In this case, the timescale for coalescence is given by:

$$\tau_{\text{clus}} = (\sigma_{\text{smallPAH,col}} \Delta V C_{\text{eff}} n_{\text{smallPAH}})^{-1}, \quad (31)$$

where $\sigma_{\text{smallPAH,col}} = 4\pi a_{\text{smallPAH}}^2$ is the cross-section for collision between two small PAHs, ΔV is the collision velocity given by Brownian motion (Eq. A30), and n_{smallPAH} is the local number density of small PAHs.

3.7. PAH evaporation

We also consider PAH cluster evaporation (Rapacioli et al. 2006). Similar to the photo-dissociation of small PAH molecules due to excitation by UV photons, large PAH clusters may lose their monomers (in our case, circumcoronene molecules) if their internal energy exceeds the monomer binding energy. Therefore, determining the dissociation rate requires the calculation of the full energy probability distribution for a PAH cluster exposed to a given photon energy E . This is achieved by using the Arrhenius expression derived from the Rice-Ramsperger-Kassel-Marcus (RRKM) theory (Tielens 2005). While solving these equations for thermal collisions (see Section 3.4) can be simplified by assuming that the probability of dissociation changes very little after each IR photon emission, for the case of the absorption of UV photons by large PAH clusters one needs to fully compute the energy probability distribution in an iterative fashion. Indeed, the larger heat capacity of these systems (Bakes et al. 2001; Tielens 2005) allows them to maintain a significant fraction of their internal energy between UV excitations (or equivalently, the cooling rate is slower than the absorption rate). This means that for these large molecular clusters the dissociation rates deviate from the linear scaling with the radiation intensity in the Habing band G_0 , instead needing more photons to dissociate (e.g. 3 – 4 photons for the dissociation of $\text{C}_{96}\text{H}_{24}$; Montillaud et al. 2013). This multi-photon tracking of the heating/cooling of large PAHs, either via Monte-Carlo methods (e.g. Lange et al. 2021, 2023) or statistical iterative methods (Purcell et al. 1976; Bakes et al. 2001; Andrews et al. 2016; Montillaud & Joblin 2014), is beyond the scope of our current modelling. We instead refer to the work of Rapacioli et al. (2006) and Montillaud & Joblin (2014) on the effective dissociation rate of large PAH clusters. Considering that the large PAHs used in CALIMA ($N_C \sim 400$) are formed from the clustering of our small PAHs (circumcoronene, $\text{C}_{54}\text{H}_{18}$), we use the results by Montillaud & Joblin (2014) for the evaporation timescales of circumcoronene clusters with a

¹⁶ We note that this implies that for higher CMB temperatures at high redshift, efficient clustering may be halted by the overall hotter gas temperature.

number of monomers ranging from 4 to 12. They find that for these large monomer clusters the evaporation time scales more steeply than $1/G_0$, until the radiation field becomes very intense ($G_0 \sim 10^6$), at which point the time between two UV photon absorptions becomes shorter than the cooling timescale. We thus use a scaling of the evaporation time given by the maximum of two functions fitted to their results:

$$\tau_{\text{evap}} = \max \left[\frac{0.19306}{G_0}, 10^{-3.169x+13.564} \right], \quad (32)$$

where $x \equiv \log_{10}(G_0)$.

3.8. PAH freezing

Similar to PAH or grain coalescence (Sections 3.6 and 2.9 respectively), we also consider the adsorption of small and large PAHs on dust grains (also called freeze-out or sequestration of PAHs). For this, we follow exactly the same procedure as in Section 2.9 for the coagulation of small grains, but computing the relative velocity (ΔV , Eq. A33) between the small and large PAHs and the small and large carbonaceous grains¹⁷. With a similar argument as for the threshold velocity for coagulation (Section 2.9), we impose the requirement that the collision energy does not exceed the van der Waals bond energy (see also Lange et al. 2023) attaching the PAH molecule/cluster to the grain surface (~ 1 eV; Rapacioli et al. 2006):

$$\tau_{\text{free}} = (\sigma_{\alpha\beta} \Delta V_{\alpha\beta} \psi_{\text{vdW}}(E) n_{\text{d},\beta})^{-1}, \quad (33)$$

where the indices α and β go over the combination of PAH sizes (β) and carbonaceous grain sizes (α), respectively, $\sigma_{\alpha\beta} = \pi(a_\alpha + a_\beta)^2$ is the collision geometrical cross-section, and E is the kinetic energy of the collision in eV, used to compute the efficiency for the adsorption via van der Waals forces:

$$\psi_{\text{vdW}}(E) = \frac{1}{1 + \exp[(E - 1)/0.1]}. \quad (34)$$

3.9. PAH photo-dissociation

Due to the temperature spikes experienced by a small PAH, there is a non vanishing probability that it can eject H, H₂ or even C₂H₂ when it experiences an intense UV radiation field in the diffuse ISM and in PDRs (Jochims et al. 1994; Allain et al. 1996; Le Page et al. 2001). There is observational evidence of this destruction effect around young stellar clusters and in H II regions (Galametz et al. 2016; Relano et al. 2016), which suggests that PAH fractions (or VSG fractions) can be used to trace the UV radiation field intensity (Pilleri et al. 2012; Bouteraon et al. 2019). When a molecule is photo-excited, it divides its energy among vibrational degrees of freedom via intra-molecular vibrational redistribution. An assumption of the uni-molecular dissociation reaction (e.g. Le Page et al. 2001; Tielens 2005) is that there exists a transition state (C₅₄H_n)* that, if reached, will lead to bond dissociation (e.g. H-loss). In the reverse process, H atoms can be re-attached to the molecule (Rauls et al.

2008; Goumans et al. 2011; Jones et al. 2014). The balance of these two reactions determines the hydrogen covering fraction of the molecule, termed the hydrogenation state of the PAH. Similar to Sections 3.4 and 3.6, the acetylene (C₂H₂) dissociation rate can be treated using a statistical approach based on RRKM theory (e.g. Tielens 2005; Montillaud et al. 2013; Andrews et al. 2016). However, at the photon energies common of PDRs and the diffuse ISM, photo-dissociation by loss of H and H₂ is faster by ~ 2 dex compared to the loss of acetylene (Allain et al. 1996; Le Page et al. 2001; Montillaud et al. 2013; Andrews et al. 2016; Castellanos et al. 2018a). Experiments have shown that for small PAHs, H-loss dominates over C-loss (Jochims et al. 1994), and for larger PAHs stripping of hydrogen atoms takes place before the C-loss starts (Zhen et al. 2014, 2015; Castellanos et al. 2018b). Therefore, a prior requirement for the fragmentation of aromatic rings in a small PAH is its full de-hydrogenation. This requires tracking the hydrogen coverage of our PAH bins, adding further computational cost to our model. We present here an alternative approach. One can define the dissociation parameter:

$$\psi = \frac{p_{\text{d}} k_{\text{UV}}}{k_{\text{a}} n_{\text{H}}}, \quad (35)$$

where p_{d} is the probability for H dissociation, k_{UV} is the photon absorption rate, k_{a} is the H attachment rate and n_{H} the hydrogen number density. This parameter effectively captures the hydrogenation balance of a PAH. Considering an attachment rate of $k_{\text{a}} = 2 \times 10^{-8} \sqrt{N_{\text{C}}/50} \text{ cm}^3 \text{ s}^{-1}$ and an average UV absorption rate $k_{\text{UV}} \simeq 2.3 G_0 \text{ s}^{-1}$, one arrives at the relation $\psi \propto p_{\text{d}} G_0 / n_{\text{H}}$ (Tielens 2005; Berne & Tielens 2011). Numerical computation of the hydrogenation of small and intermediate size PAHs has shown that the transition from fully de-hydrogenated to normally hydrogenated is very sharp in the G_0 - n_{H} plane (Montillaud et al. 2013; Andrews et al. 2016). Since the relevant quantity for C-loss is the fraction of small PAHs that are de-hydrogenated (χ_{dH}), we use fitting functions for the limiting region between de-hydrogenated and normally hydrogenated circumcoronene provided in figure 10 of Montillaud et al. (2013), allowing for a 1 dex dispersion, where PAHs transition from being 10% to 90% totally de-hydrogenated. We then assume that upon photon absorption, the energy is either spent on IR emission or on C-loss. Therefore, the probability for dissociation of a PAH upon absorption of a photon with energy E is given by (see also Section 3.4):

$$P_{\text{diss}}^{\text{C}_2\text{H}_2}(E) = \frac{k_{\text{diss}}^{\text{C}_2\text{H}_2}(E)}{k_{\text{diss}}^{\text{C}_2\text{H}_2}(E) + k_{\text{IR}}/(n_{\text{max}} - 1)}, \quad (36)$$

where we compute the dissociation rate as in the thermal sputtering calculation of Section 3.4 (see also Murga et al. 2020). From this, one can calculate the dissociation rate for a Draine et al. (1979) radiation field in the Habing band as:

$$R_{\text{diss}}^{\text{C}_2\text{H}_2}(G_0) = \int_{6\text{eV}}^{13.6\text{eV}} \chi_{\text{dH}} \sigma_{\text{PAH}}(E) P_{\text{diss}}^{\text{C}_2\text{H}_2}(E) \frac{F(E)}{E} \text{d}E. \quad (37)$$

¹⁷ We do not consider freezing of PAHs on silicate grains, as this would alter their chemical composition.

The numerical value of this rate for diffuse ISM conditions ($n_{\text{H}} = 0.1 \text{ cm}^{-3}$ and $G_0 = 1$) is $4.68 \times 10^{-17} \text{ s}^{-1}$.

3.10. Molecular hydrogen formation mediated by PAHs

In Section 2.10 we based our modelling of molecular hydrogen formation on the assumption that the attachment surface for hydrogen on dust grains can be separated into physisorbed and chemisorbed sites. The former are characterised by weak van-der-Waals forces of a few tens of meV, which implies that when the dust temperature increases beyond $\sim 20 \text{ K}$ H atoms quickly evaporate from the grain surface. This causes a drop in the H_2 formation efficiency, since beyond this point the total formation rate relies solely on the recombination via the Eley-Rideal mechanism on chemisorbed sites. This appears to be in disagreement with observations of PDRs (Habart et al. 2003b; Allers et al. 2005), where estimated formation rates close to $\sim 3 \times 10^{-17} \text{ cm}^3 \text{ s}^{-1}$ are well above the predictions for dust at high temperature. This points to additional physical mechanisms that can efficiently form H_2 in these regimes in which traditional dust grain formation mechanisms appear to fail.

Recently, more accurate modelling of PAH photo-physics (e.g. Montillaud et al. 2013; Boschman et al. 2015; Andrews et al. 2016; Barrera et al. 2023) and accelerated progress in experimental studies of PAH-hydrogen reactivity (e.g. Thrower et al. 2012; Boschman et al. 2012; Mennella et al. 2012; Castellanos et al. 2018a) enable to re-evaluate the pathways to H_2 formation in the ISM (see the review by Wakelam et al. 2017). Observed correlations between H_2 and PAH emission (Habart et al. 2003a,b) appear to support the scenario where PAHs can efficiently form H_2 in a highly excited state within PDRs. We therefore include molecular hydrogen formation catalysed by PAHs in CALIMA.

H_2 formation on PAHs is usually considered to take place via two possible routes:

- A hydrogen atom forms a covalent bond with a PAH molecule, and then it is abstracted by a second colliding hydrogen atom.
- UV photon absorption by a super-hydrogenated PAH molecule leads to relaxation by the loss of H_2 .

Molecular hydrogen abstraction has been observed in desorption experiments on coronene deuterium bombardment (Thrower et al. 2012), as well as predicted by theoretical modelling (Rauls et al. 2008). The abstraction (as well as the hydrogenation) is subject to energy barriers in neutral coronene (Boschman et al. 2012) of 10 meV, while Bauschlicher et al. (2001) predicts no barriers for H_2 abstraction from coronene and circumcoronene anions. Given the experimentally determined abstraction cross-section of 0.06 \AA^2 per coronene C atom, we assume for all abstraction of super-hydrogenated anion and neutral PAHs (both small and large) the Eley-Rideal rate:

$$k_{\text{ER}} \simeq 8.7 \times 10^{-13} \sqrt{\frac{T}{100\text{K}}} \left(\frac{n_{\text{H}}}{1\text{cm}^{-3}} \right) \text{ cm}^3 \text{ s}^{-1}. \quad (38)$$

We now need to determine what fraction of the PAH population is in a super-hydrogenated state. Similar to

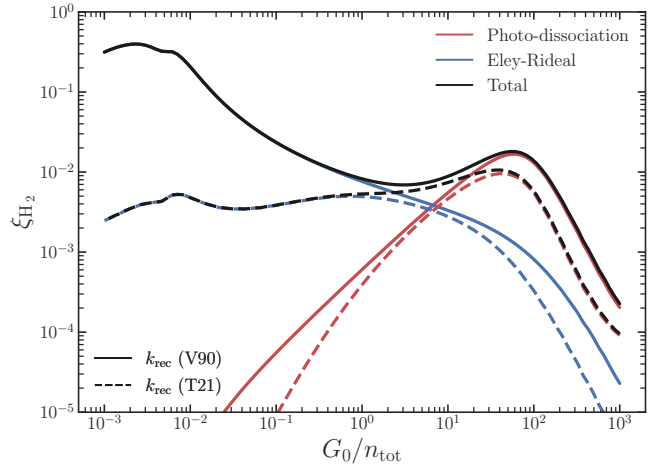


FIG. 8.—: Molecular hydrogen formation efficiency by small PAHs (circumcoronene). We fix the radiation field intensity to the Habing parameter $G_0 = 100$, the free electron fraction to $X_e = 0.1$, and assume half of the H abundance is already in H_2 . Molecular hydrogen is formed via two mechanisms: Eley-Rideal desorption (blue lines) of H_2 for neutral super-hydrogenated PAHs, and photo-desorption (red lines) of H_2 from normal and partially de-hydrogenated PAHs. The former dominates at high gas density in low radiation field, while the latter is important in a narrow regime at low density before radiation strips circumcoronene of all its H atoms. We compare the resulting efficiencies following two different models for electron recombination on PAHs by Verstraete et al. (1990) and Tielens (2021).

the approximations made in Section 3.9, it is safe to assume that the transition from normally hydrogenated to super-hydrogenated is very sharp in G_0 - n_{H} space (see Figure 9 in Andrews et al. 2016), and that this transition is approximately independent of size for PAHs with $N_{\text{C}} \geq 54$. We obtain a transition curve given by:

$$\log_{10} G_0 = 0.995 \log_{10} \left(\frac{n_{\text{H}}}{1\text{cm}^{-3}} \right) - 1.945, \quad (39)$$

with the width of the transition being $\Delta \simeq 0.05$ in log-log space as extracted from figure 9 in Andrews et al. (2016). H_2 abstraction is only allowed for anion and neutral PAHs.

For normally hydrogenated and partially de-hydrogenated PAHs, the absorption of a UV photon may give rise to the loss of an H atom or an H_2 molecule (Allain et al. 1996). Following the microcanonical description of bond dissociation used in Sections 3.4 and 3.9, we compute the H_2 photo-desorption rate as:

$$k_{\text{H}_2} = \int_{E_{\text{min}}}^{13.6\text{eV}} \frac{k_{\text{diss}}(\text{H}_2)}{k_{\text{diss}}(\text{H}_2) + k_{\text{diss}}(\text{H}) + k_{\text{IR}}/(n_{\text{max}} + 1)} \times \chi_{\text{pdH}} \sigma_{\text{PAH}}(E) \frac{F(E)}{E} dE, \quad (40)$$

where $F(E)$ is the flux density of the radiation field at energy E , $E_{\text{min}} = n_{\text{max}} \Delta \epsilon$ (see Section 3.4), χ_{pdH} is the fraction of partially de-hydrogenated PAHs, and the dissociation rates k_{diss} are given by Eq. A54. We note that in this case we cannot use directly the fraction of de-hydrogenated PAHs χ_{dH} to compute the rate of

dissociation from normally to partially de-hydrogenated PAHs. As the PAH molecules becomes completely de-hydrogenated, relaxation upon UV photon absorption is no longer available through H or H₂ loss, but rather C-loss becomes important (see Section 3.9). Hence, to maintain consistency across our model and prevent unrealistic H₂ production from fully de-hydrogenated PAHs, we suppress the fraction of de-hydrogenated PAHs χ_{dH} when it exceeds 99% of the total PAH population, assuming at this point that all de-hydrogenated PAHs are bare carbon skeletons. This is done by applying a logistic equation correction to the fraction of de-hydrogenated PAHs to compute the fraction of partially de-hydrogenated PAHs:

$$\chi_{pdH} \equiv \frac{\chi_{dH}}{1 + \exp[(\chi_{dH} - 0.99)/8 \times 10^{-4}]}, \quad (41)$$

which reproduces the width of the transition to fully de-hydrogenated PAHs in [Montillaud et al. \(2013\)](#) and [Andrews et al. \(2016\)](#). We note that this is only applied for small PAHs, as H₂ photo-desorption is not an efficient process for our large PAH clusters because UV absorption is instead followed by evaporation of the circumcoronene monomers (Eq. 32). Large PAHs only contribute to H₂ formation via the Eley-Rideal mechanisms.

In Fig. 8 we present the H₂ formation efficiency for small PAHs in an environment with $G_0 = 100$, with a fixed free electron fraction $X_e = 0.1$, and half of the H abundance already in the form of H₂. The H₂ formation efficiency is defined as ([Andrews et al. 2016](#); [Castellanos et al. 2018a](#)):

$$\xi_{H_2}(Z) = \sum_i \frac{2k_{H_2}(Z, i)f(Z, i)}{k_{col}^i(Z)}, \quad (42)$$

where $f(Z, i)$ is the fraction of PAHs with charge Z , and the sum is over all hydrogenation states for a PAH with charge Z and k_{col}^i its hydrogen collisional rate. For neutral species we use a collisional rate with the average H addition energy barrier ([Rauls et al. 2008](#); [Boschman et al. 2015](#)) of $E_{add} = 60$ meV:

$$k_{col}^0 = n_H \sigma_{geo} \sqrt{\frac{8k_B T}{\pi m_H}} \exp\left(-\frac{E_{add}}{k_B T}\right), \quad (43)$$

where σ_{geo} is the PAH geometrical cross section. For anions and (di-)cations, we follow [Andrews et al. \(2016\)](#) and consider fiducial rates of $k_{col}^- = 7.8 \times 10^{-10} n_H \text{cm}^3 \text{s}^{-1}$ and $k_{col}^{+/2+} = 1.4 \times 10^{-10} n_H \text{cm}^3 \text{s}^{-1}$. The charge population of PAHs is obtained from the method described in Section 3.1. We have computed separately the contribution from Eley-Rideal (blue lines) and photo-dissociation (red lines) to the total molecular hydrogen formation efficiency (black lines). While keeping G_0 fixed, we vary the value of the total gas density ($n_{tot} = n_H + 2n_{H_2}$), exploring a slice in G_0 - n_H space. We find that at high G_0/n_{tot} photo-dissociation dominates H₂ formation for a narrow range of values, quickly dropping as the PAH population becomes dominated by totally bare carbon skeletons. H₂ abstraction via the Eley-Rideal mechanism is the dominant route of molecular hydrogen formation at low G_0/n_{tot} . Eley-Rideal at high densities is highly reliant on the abundance of neutral and anionic PAH species. As discussed in Section 3.5, the charge state

in those regimes depends on the assumptions regarding electron recombination and attachment. [Tielens \(2021\)](#) predict a dominant anion population at very high gas/electron number densities, for which the collision rate is larger, resulting in a lower efficiency. This effect can be appreciated by comparing the solid curves using the Spitzer recombination rate modified by [Verstraete et al. \(1990\)](#), and the dashed curves using the [Tielens \(2021\)](#) recombination rate. Overall, we find that maximum efficiencies are on the order of $\xi_{H_2} \sim 1\%$, in agreement with previous models of H₂ formation on PAHs (e.g. [Le Page et al. 2009](#); [Boschman et al. 2015](#); [Andrews et al. 2016](#); [Castellanos et al. 2018a](#)).

4. NUMERICAL VALIDATION

4.1. Equilibrium temperature

To begin validating the predictions from CALIMA, we perform a one-zone, static test of the equilibrium temperature at varying densities. We perform this by smoothly interpolating between 10^{-2} and 10^5H cm^{-3} and allowing the chemistry solver to reach thermal equilibrium (i.e. balance of heating and cooling processes), while maintaining the density fixed. All cells are initialised with $T = 10^4 \text{K}$ and with all ions fully neutral. A constant $G_0 = 1$ and cosmic ray ionisation rate of $\eta_{CR} = 10^{-16} \text{s}^{-1} \text{H}^{-1}$ are fixed across all densities. We assume that all cells have the same total metallicity Z , with solar abundances given by [Asplund et al. \(2009\)](#). Depletions onto dust are taken from [Zubko et al. \(2004\)](#) for oxygen, and from [Dopita et al. \(2000\)](#) for iron, magnesium, silicon and carbon. Direct sum of these depletions result in a DTM of 0.4 or a gas-to-dust (GTD) of 162. Since we force CALIMA to maintain the stoichiometry of the silicate grain (see Section 2.4) we compute the true silicate dust mass using Eq. 10, which instead result in a DTM of 0.391. We then distribute dust mass in each grain size by following the resulting small-to-large (STL) ratio found in [Dubois et al. \(2024\)](#) for the G10 simulation as in agreement with the extinction curve of the MW (i.e. $\sim 20\%$ of the dust mass in small grains). We then extend this to include 13.42% of the carbon dust into PAHs ([Zubko et al. 2004](#)), with equal mass in small and large PAHs. In panel a) of Fig. 9 we show (black solid line) the equilibrium curve for this elemental and dust abundances without dust evolution and using the vanilla ISM model in PRISM. In agreement with previous models (e.g. [Wolfire et al. 2003](#); [Bialy & Sternberg 2019](#); [Kim et al. 2023](#)), we find that the thermal instability is triggered for $n_H > 1 \text{cm}^{-3}$. For $n_H \gtrsim 10^3 \text{cm}^{-3}$ we find a rise in temperature, related to heating from H₂ formation and destruction. The red points are observational inferred kinetic temperatures from [C II] observations of the Galactic plane by [Gerin et al. \(2015\)](#). The no-evolution curve appears to deviate from these observations, predicting a steeper decrease in temperature at $10 < n_H < 10^2 \text{cm}^{-3}$. This results from our choice of C depletion of 0.4991 from [Dopita et al. \(2000\)](#) instead of the larger value of 0.630 the BARE-GR-S model assumed ([Zubko et al. 2004](#)). Together with a fixed DTM across all n_H , it results in increased cooling from more available [C II] and lower H₂ heating due to a lower H₂ formation for a lower dust mass compared to CALIMA at high n_H . This demonstrates how small variations in depletion

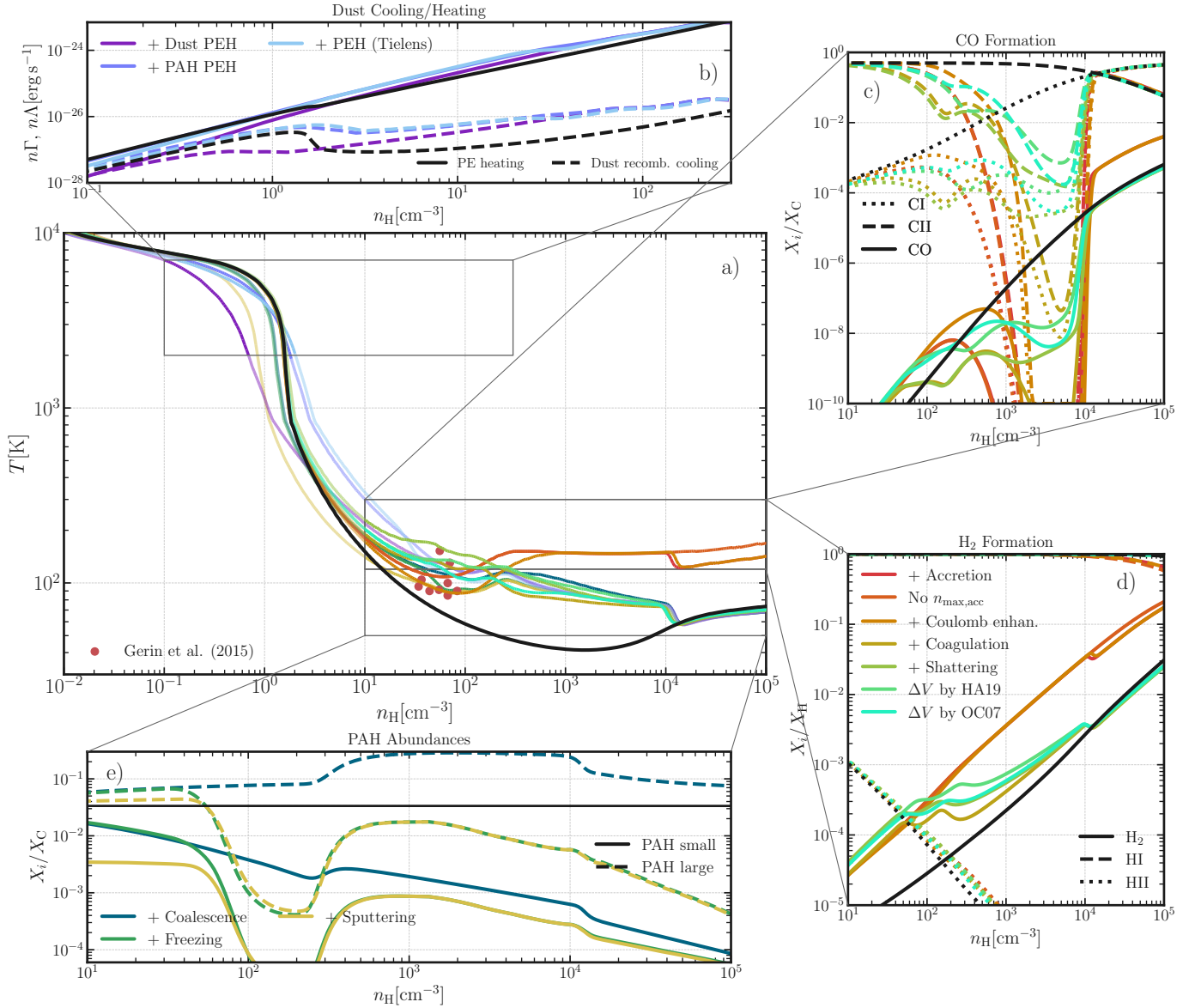


FIG. 9.— Temperature-density equilibrium curve comparing the fixed dust (solid black line) to the CALIMA model (colour lines). Each line progressively add on top to the previous line another dust/PAH process, starting from accretion (red line) and ending in the ones including PEH from PAHs (dark and light cyan lines). From the central panel and going clockwise: a) temperature-density, b) volumetric PEH and dust recombination cooling, c) fraction of C atoms depleted on neutral C, C $^+$ and CO, d) fraction of H atoms on molecular H $_2$, neutral HI, and ionised H II, and e) fraction of C atoms depleted on small and large PAHs. Red points in panel a) are the inferred temperatures from [C II] observations of the Galactic plane by Gerin et al. (2015). See text for further details.

of key elements for the cooling and heating of the ISM can have non negligible effects in the equilibrium curves, again raising a point made in Katz et al. (2022) that modulating abundances/depletion factors within the uncertainties of the Galaxy can return the curves into agreement with these observations.

We now test how the growth of dust mass via gas-phase accretion can leave a signature on the final equilibrium curve. In panel (a) of Fig. 9 we highlight the influence of dust processes on the equilibrium curve within $10 < n_H < 10^5$ cm $^{-3}$ in the middle inset box. Including accretion, coagulation and shattering leads to growth of the overall mass as well as shattering of mass between different grain sizes. Accretion (red and orange lines) alone

is seen as a clear deviation from the fixed curve for densities above $n_H \gtrsim 10$ cm $^{-3}$, leading to significantly higher gas temperatures above this density. The origin of this difference is caused by a simultaneous decrease in the O I and C II cooling due to accretion of these gas-phase ions, and the increased H $_2$ heating from larger dust mass/surface area. In panel d) we show the signature of the latter on the H $_2$ fraction (solid lines). Dust growth is faster for smaller grains due to their larger surface-to-mass ratio, and for the same dust composition and temperature, results in a larger H $_2$ formation rate (Cazaux et al. 2004). For fixed silicate stoichiometry, Fe is fully depleted in our initial conditions. This means that while silicates cannot experience a large growth in mass from

gas-phase ions, carbon is depleted to $\sim 50\%$. Therefore, carbonaceous grains compete with CO for the available free carbon. However, in our idealised test there is no inclusion of attenuation of the ISRF at high densities. This means that while CO would be expected to rapidly grow at these higher densities (e.g. Glover et al. 2010; Glover & Clark 2012), the continuous destruction via our unattenuated G_0 releases carbon that can be accreted by grains that are definitely not destroyed at these densities and temperatures. This can also be appreciated on panel c), where gas at $10^2 < n_{\text{H}} < 10^4 \text{ cm}^{-3}$ shows large depletions of C I and C II compared to the fixed dust curves (black lines). This leads to complete suppression of CO at this density regime when equilibrium is reached. It is only prevented for $n_{\text{H}} > 10^4 \text{ cm}^{-3}$ when dust grains start to become covered with ice mantles and the accretion efficiency is highly suppressed (see the curve with no $n_{\text{max,acc}}$). Coulomb enhancement appears to have a non-negligible effect on these results, by preventing efficient accretion for $10^2 < n_{\text{H}} < 10^3 \text{ cm}^{-3}$ due to the prevalent positive grain charge in these neutral phases (see e.g. Fig. 3).

We also explore the influence of turbulent collisions between grains in the H_2 and CO formation. This is a static numerical experiment, so we do not have a direct measure of the gas dynamics for each density. Since this is a fundamental input for the subgrid turbulence models in CALIMA, we have opted by a choice of gas velocity dispersion scaling laws. We use the Larson relation (Larson 1981; Hennebelle & Falgarone 2012) as obtained by Colman et al. (2024) for a large range of MHD simulations of turbulent molecular clouds:

$$\sigma = 5.67 \left(\frac{\langle n_{\text{H}} \rangle}{10^2 \text{ cm}^{-3}} \right)^{-0.25} \text{ km s}^{-1}, \quad (44)$$

where $\langle n_{\text{H}} \rangle$ is the spatial average hydrogen number density, which in our case would be the cell hydrogen number density. Neither coagulation nor shattering alter the total dust mass, but since they can transfer mass between grains of different sizes they can affect the surface-to-volume ratio and hence the accretion and H_2 formation rates. Adding coagulation on top of accretion leads to a rapid transfer of mass from the small to the large grains, leading to significantly lower depletions of carbon in the $10^2 < n_{\text{H}} < 10^4 \text{ cm}^{-3}$ regime, as well as lower H_2 fractions, resembling the fixed dust fractions for $n_{\text{H}} > 10^4 \text{ cm}^{-3}$. This is due to the fact that while accretion is halted at very high densities due to ice formation, coagulation can still take place, highly depleting the reservoirs of small grains. Adding shattering on top of coagulation allows for a return of some of the coagulated mass back into the small grain bin, particularly at $n_{\text{H}} < 10^3 \text{ cm}^{-3}$. This can be seen as a higher H_2 fraction in panel d). We have also compared the influence of different prescriptions for the grain relative velocity ΔV . Given that the model from Hirashita & Aoyama (2019) predicts slightly lower ΔV than Ormel & Cuzzi (2007), we find both higher coagulation and shattering rates. This results in shattering operating at higher densities (hence larger carbon depletion due to higher abundance of small grains), and coagulation at lower densities (hence lower carbon depletion due to lower abundance of small grains). We note that the inclusion of coagula-

tion and shattering is very important in the final equilibrium temperature at these densities, displacing the gas at $10^2 < n_{\text{H}} < 10^4 \text{ cm}^{-3}$ from $\sim 150 \text{ K}$ to $\sim 70 \text{ K}$.

Similarly, in panel e) we examine the influence of PAH evolution on the abundances of small and large PAHs (bottom inset box of panel a) in Fig. 9). Coalescence of small PAHs to form PAH clusters is a very fast process within the high density phases, giving rise to a very steep decrease with gas density in the fraction of carbon atoms depleted onto small PAHs. Adding freezing on regular carbonaceous grains (green lines) leads to even lower abundance of small PAHs, but the more drastic difference is seen for large PAHs, which now become highly depleted at high densities. Freezing is particularly effective at $50 < n_{\text{H}} < 300 \text{ cm}^{-3}$. This is caused by the narrow region in which relative velocity between PAHs and grains is sufficiently slow to allow for van-der-Waals surface bonds, but not high enough density that depletes the majority of the grain mass into large grains with lower surface-to-volume ratio. Sputtering is also shown in panel e) (yellow lines) to illustrate the higher efficiency of destruction of PAHs in warm gas compared to regular grains.

Given our direct modelling of photo-electric heating and charging for grains and PAHs, we also compare the the results from our approach to MRN-averaged heating and recombination cooling (i.e. Bakes et al. 1994; Weingartner & Draine 2001a). In panel b) of Fig. 9 we show the photoelectric heating rate $n\Gamma$ (solid lines) and the recombination cooling rate $n\Lambda$ (dashed lines), comparing the result of the fixed dust model (black lines) with our live dust modelling. These models include all the processes referenced before: accretion, Coulomb enhancement, coagulation, shattering, coalescence, freezing and sputtering of PAHs, but now computing directly the efficiencies of heating and cooling from the models in Sections 2.3 and 3.5. Firstly, only including direct photo-electric heating from dust grains presents a significantly lower turnover in the temperature curve (see purple line in panel a)). This is in agreement with the result that large grains have a secondary contribution to photo-electric heating (e.g. Bakes et al. 1994). However, for $n_{\text{H}} \gtrsim 2 \text{ cm}^{-3}$ the injected energy is larger than the fixed model ratio, due to a larger dust mass caused by gas-phase accretion. Adding to this the injected energy from PAHs, this difference is even larger, which causes the turnover of these curves (violet and cyan) to be at higher densities and significantly less steep compared to the fixed dust model. However, this difference with the only-dust phot-electric heating becomes negligible for $n_{\text{H}} \gtrsim 30 \text{ cm}^{-3}$, as much of the PAH mass is frozen onto regular grains. We have also included a modification to the PAH charge modelling given by more efficient electron recombination from Tielens (2021) (see also Section A.5). We find this to have a minimal effect on the final efficiency.

We end this numerical benchmarking by noting that although the experiment was not designed to pass through the Gerin et al. (2015), variations in dust and PAH processes encompass the scatter and slope of their result, while the fixed dust model fails to do so.

4.2. Isolated galaxy simulations

4.2.1. Methods

We explore the results of CALIMA in a dynamical system by considering isolated galaxy simulations. We make use of the G8 initial conditions presented in Rosdahl et al. (2015) (see their table 1). These were also used for the original implementation of dust evolution in RAMSES (Dubois et al. 2024) as well as in PRISM (Katz et al. 2022). The G8 galaxy has a halo mass of $10^{10} M_{\odot}$ (circular velocity of 30 km s^{-1}), with a galaxy mass (gas and stars) that adds up to 3.8% of the halo mass, hence $3.8 \times 10^8 M_{\odot}$. The gas mass fraction is 0.171951. In order to reduce the extent of the initial starburst caused by the initial conditions of an isolated galaxy, we introduced a perturbation in the initial vertical gas velocity of 30 km s^{-1} modulated by two sinusoidal functions in the x and y axis of the cartesian box with wavelength of 200 pc. The initial metallicity Z_{init} of G8 is set to 0.1, 0.3, and $0.5 Z_{\odot}$, using the Asplund et al. (2009) abundance ratios of elements and an initial DTM = 10^{-3} , with the depletion ratios used in Section 4.1 scaled to this lower DTM. Instead of using a profile of decreasing metallicity with radius (e.g. Katz et al. 2022), we use a uniform metallicity and DTM across the disc, with gas outside of the disc at a metallicity of $10^{-4} Z_{\odot}$ and no dust. We track the abundance in O, N, C, Mg, Si, S, Fe and Ne. The ion chemical network employs eight ionisation states of O, seven for N, six for C, ten for Mg and Ne, and eleven for Si, S, and Fe. We also follow all ionisation states of H and He, in addition to H_2 and CO. For the latter two molecular species, we also apply the correction to density coming from the unresolved turbulent density distribution (see Section 2.4). The disc is initialised atomic and with all metals fully neutral, while the halo gas is set as fully ionised and with all metals in their highest ionisation state. We employ the ‘fast’ solver in Katz (2022). In order to provide a comparison with non-evolving dust models, we also run a suite of twin simulations with the same initial conditions and gas-phase metallicities as the CALIMA simulations, but setting the dust abundances based on the scaled DTM and PAH mass fraction scaling with $12 + \log(\text{O}/\text{H})$ from Rémy-Ruyer et al. (2014, 2015). The grain size distributions are initialised to follow the equilibrium distribution obtained for the G8 simulations in Dubois et al. (2024), which predicts a ~ 0.2 total dust mass in small grains. For these simulations, we turn off the dust evolution, only allowing for dust and PAH injection due to stellar processes (e.g. SNe and AGB winds). We also use the dust chemistry (e.g. cooling, heating, H_2 formation) from the original version of PRISM (Katz et al. 2022).

Star formation is modelled using the gravo-turbulent criteria (Kimm et al. 2017) to determine local star formation efficiencies. Star formation is only allowed if the local turbulent Jeans length is unresolved and if $n_{\text{H}} \geq 10 \text{ cm}^{-3}$. The formed stellar particles are integer multiples of $1830 M_{\odot}$. We include feedback from SNII and SNIa using the mechanical feedback prescription of Kimm & Cen (2014), as well as stellar winds (Agertz et al. 2021). Core-collapse SNe take place by stochastically sampling the SNII progenitors that leave the main sequence during each time step, using the main-sequence lifetime-mass relation by Schaerer et al. (1993). In order to be consistent with our choice of

yields (Limongi & Chieffi 2018), we assume that stars with $8 \leq m_{*}/M_{\odot} \leq 25$ explode as SNeII with the canonical energy of 10^{51} erg . We also include a minimal model for the gas pre-processing caused by OB stars in the immediate gas surrounding the stellar particle, allowing for a larger amount of momentum injection (Geen et al. 2015)¹⁸. Our choice of yields follows the implementation in the MEGATRON simulations Katz et al. (2024). This uses the individual element yields for SNeII from Limongi & Chieffi (2018), for SNeIa from Seitenzahl et al. (2013), and for AGB winds from Ritter et al. (2018). We direct the interested reader to Katz et al. (2024) for further details. We use these yields to directly compute the seeding of dust grains and PAHs, using the prescriptions in Section 2.1 and 3.2.

We make use of on-the-fly radiation transfer with the M1 moment method in RAMSES-RT (Rosdahl et al. 2013; Rosdahl & Teyssier 2015), using the GLF scheme to construct intercell fluxes. We track eight radiation bins from the IR to the EUV (see Table 2), employing the reduced speed of light approximation setting $\tilde{c} = 0.01c$. The radiation and thermo-chemistry steps are subcycled up to 500 times per each hydrodynamic step. In practice, the number of subcycles falls from 7-8 after the first star is formed to 2-3 when the first SN goes off. Radiation is emitted from stellar particles based on their mass, age, and metallicity using the BPASS v2.2.1 SED (Stanway & Eldridge 2018), with the Chabrier initial mass function and a maximum mass of $300 M_{\odot}$. The mean cross-section for each radiation bin is computed based on the stellar-polling method of RAMSES-RT (see Section 2.11). In addition, the simulation is filled with a $z = 0$ UV background (Haardt & Madau 2012) with a self-shielding prescription that exponentially decreases the intensity of the background for $n_{\text{H}} \geq 10^{-2} \text{ cm}^{-3}$. We also consider effects of radiation pressure for single scattering of UV and optical and multi-scattering in the IR (Rosdahl & Teyssier 2015).

Cosmic-rays are not self-consistently seeded in these simulations, so we use a fixed cosmic-ray background ionisation rate of $\eta_{\text{CR}} = 10^{-16} \text{ s}^{-1} \text{ H}^{-1}$. We employ the AMR capabilities of RAMSES to reach spatial resolutions of 4.5 pc in the highest level of refinement. We refine when a cell hosts eight times its initial mass in stars or in order to resolve the Jeans length by four cells.

We emphasise that our choice of initial conditions is not intended to resemble any particular galactic system, rather we use these G8 simulations to test CALIMA in a dynamical, galactic environment.

4.2.2. Variation in dust and PAH properties across ISM phases

We begin by examining density-weighted projections of our G8 galaxy. In Fig. 10 we show face-on (first and third row) and edge-on (second and fourth rows) projections of the $Z_{\text{init}} = 0.3 Z_{\odot}$ at 200 Myr, after the initial starburst has subsided and the SFR has stabilised ($\sim 0.02\text{--}0.04 M_{\odot}/\text{yr}$). The galaxy exhibits a multi-phase ISM with cold, dense clumps and filaments embedded within a diffuse warm medium. Several large hot gas bubbles are visible, driven by recent star formation and

¹⁸ This is included since at $\sim 4 \text{ pc}$ H II regions are mainly unresolved.

Group Name	E_{low} [eV]	E_{high} [eV]	Function
IR	0.1	1.0	Infrared radiation pressure
Opt.	1.0	5.6	Radiation pressure, charging of large grains
FUV	5.6	11.2	PAH cluster evaporation, photo-electric heating, Mg I, Si I, S I, Fe I ionisation
LW	11.2	13.6	H ₂ dissociation, PAH dissociation, charging of small grains and PAHs, C I ionisation
EUV ₁	13.6	15.2	H I, N I, O I, Mg II ionisation
EUV ₂	15.2	24.59	H ₂ , C II, Si II, S II, Fe II, Ne I ionisation
EUV ₃	24.59	54.42	He I, O II, C III, N II, N III, Si III, Si IV, S III, S IV, Ne II, Fe III ionisation
EUV ₄	54.42	∞	He II, O III+, N IV+, C IV+, Mg III+, S V+, Si V+, Fe IV+, Ne III+ ionisation

TABLE 2: Details of our choice of radiation spectrum discretisation. We indicate the photon group name, the lower and upper energy limits in eV, as well as their main roles in our thermochemistry modelling. We include ions that have their ionisation potential within each of the bins limits.

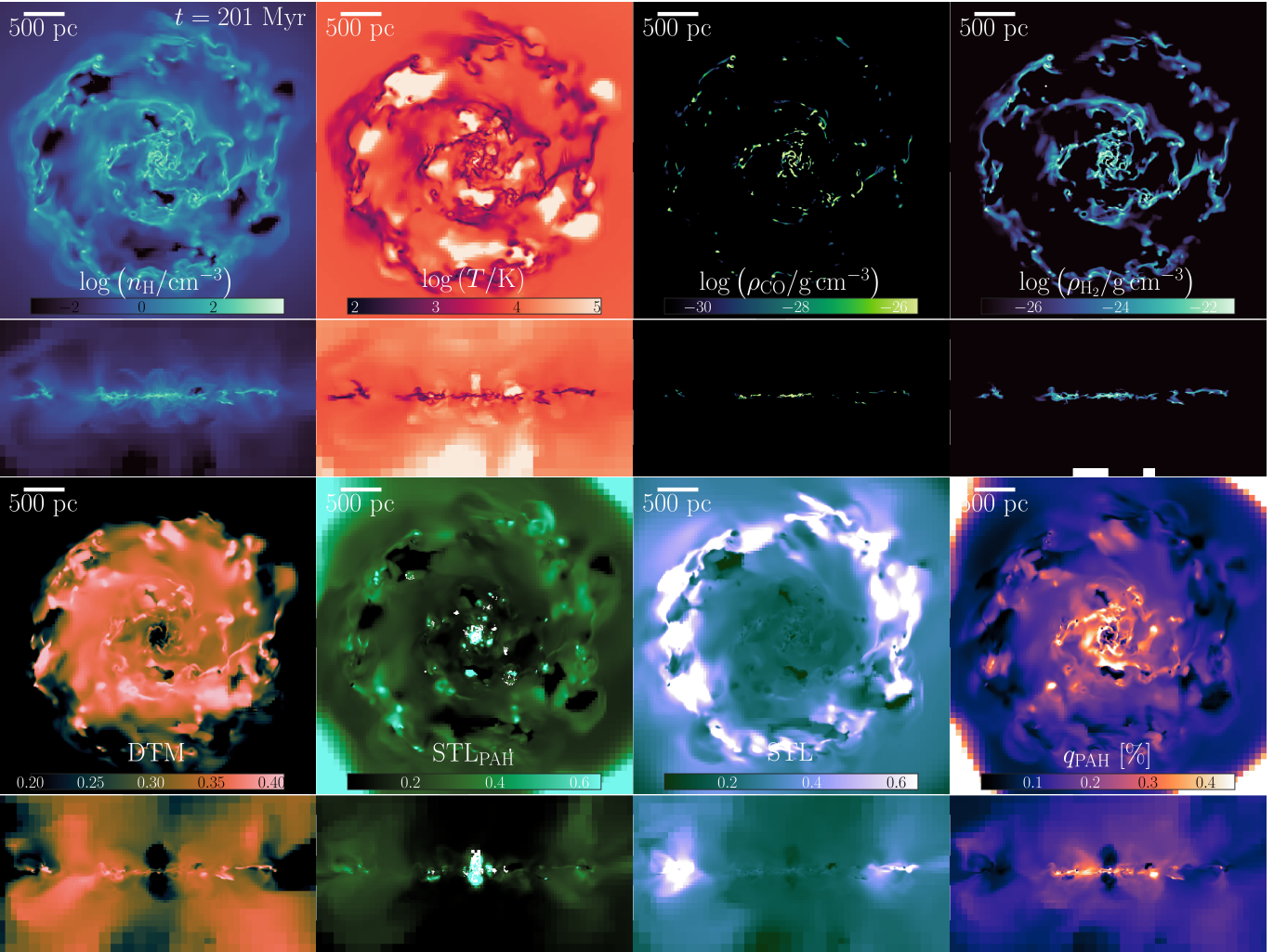


FIG. 10.—: Density-weighted projection of the G8 galaxy with initial metallicity of $0.3Z_{\odot}$ at 200 Myr after the beginning of the simulation. The projection has a horizontal width of 4 kpc and a depth of 0.8 kpc. From top-left corner in clockwise order: (1) hydrogen number density, (2) gas temperature, (3) CO mass density, (4) H₂ mass density, (5) q_{PAH} , ratio of PAH mass to total dust and PAH mass, (6) smallt-to-large (STL), ratio of small dust grain mass to large grain mass, (7) STL_{PAH} , ratio of small PAH mass to large PAH mass, and (8) DTM, fraction of metal mass depleted onto dust and PAHs. First and third rows show G8 face-on, while second and fourth show it edge-on.

SN energy injection. In the edge-on projections the disc appears razor-thin, with hot outflows piercing through the dense ISM and propelling filaments and shells outside of the plane. By looking at the projections of CO and H₂ density it is clear that the cooler phases of the ISM are spatially constrained to the plane of the disc, with CO particularly limited to the very high density gas clumps exceeding $\gtrsim 100 \text{ cm}^{-3}$. In order to quantify the relative importance of dust mass and different dust properties, we define the following useful quantities:

- Dust-to-metal (DTM) mass ratio as:

$$\text{DTM} = \frac{M_{\text{dust}}}{M_Z + M_{\text{dust}}},$$

where M_Z is the mass in gas phase metals,

- Small-to-large (STL) mass ratio for all dust grains (not including PAHs):

$$\text{STL} = \frac{M_{\text{smallC}} + M_{\text{smallSil}}}{M_{\text{largeC}} + M_{\text{largeSil}}},$$

as well as an equivalent for PAHs:

$$\text{STL}_{\text{PAH}} = \frac{M_{\text{smallPAH}}}{M_{\text{largePAH}}},$$

- q_{PAH} is the ratio of mass in PAHs to the total dust and PAH mass:

$$q_{\text{PAH}} = \frac{M_{\text{PAH}}}{M_{\text{dust}} + M_{\text{PAH}}}.$$

The DTM distribution shows weak correlation with the highest-density regions, instead exhibiting variations of ~ 2 across the disc. Some low-DTM regions within the disc coincide with low-density, hot gas, while the inner region shows lower DTM values. This central depletion is consistent with the ‘DTM cavity’ found in the NewCluster cosmological simulation (Byun et al. 2025), which they attribute to efficient dust destruction within rapidly growing bulges at high redshift. In our case, a strong outflows appears to be forming at the centre of the disc, easily seen in the edge-on projections as two bubbles with low DTM, STL and q_{PAH} .

The STL_{PAH} and STL projections (lower centre panels of Fig. 10) reveal preferential destruction and growth of small grains and PAHs. Outside the disc, dust properties reflect the initial conditions ($\text{STL} \sim 0.2$, $\text{STL}_{\text{PAH}} \sim 1$), but these regions contribute negligibly to the total dust and PAH budget (see DTM and q_{PAH} projections) and are excluded from further analysis. Within the disc, both ratios show strong spatial variations: regions of efficient small grain destruction coincide with high gas temperatures, while zones of enhanced small grain and PAH growth align with cold, dense clumps and filaments. PAHs exhibit larger variations than silicate/carbonaceous grains due to their shorter destruction timescales, producing stronger contrasts between ISM phases. The STL_{PAH} projection shows a distinctive pattern around recent star formation sites: small PAH-dominated clumps (bright green) are surrounded by channels of very low PAH mass (white pixels). This spatial sequence traces PAH photo-destruction: large PAHs

are first destroyed (Section 3.7), releasing small PAHs and increasing STL_{PAH} , followed by acetylene loss from small PAHs (Section 3.9), which decreases STL_{PAH} .

The q_{PAH} projection (lower right of Fig. 10) shows complex behavior. While large-scale features of enhanced q_{PAH} correlate with molecular gas (CO and H projections) and dust-enriched regions (DTM projection), many high- q_{PAH} structures lack corresponding features in the dense ISM tracers. Notably, some high- q_{PAH} clumps exhibit low- q_{PAH} cores, while the corresponding CO and H distributions show no density depletion at these locations. This break in CO-PAH correlation could be related to the one observed in resolved studies of local star-forming galaxies (e.g. Kim et al. 2025), and to the observability of PAH emission in star forming regions (e.g. Rodríguez et al. 2025). Combined with the presence of PAHs in diffuse ISM phases, these results suggest that using PAHs as molecular gas and star formation tracers may be more complex than commonly assumed.

In Fig. 11 we show temperature-density phase diagrams of the CALIMA simulations with (from left to right) $Z_{\text{init}} = 0.1, 0.3$, and $0.5 Z_{\odot}$. These have been computed by stacking all outputs between 100–200 Myr, for a cylindrical volume centred on the G8 galaxy with radius of 1.5 kpc and height above and below the disc of 2 kpc. In the top row each bin in T - n_{H} space is colour-coded with the mass-weighted median DTM. Median values of DTM show a stiff dependence on Z_{init} , with effective gas-phase accretion turning on for $Z_{\text{init}} > 0.1 Z_{\odot}$, in agreement with the results from Dubois et al. (2024) and observations (e.g. Rémy-Ruyer et al. 2014; De Vis et al. 2019; Konstantopoulou et al. 2022). In the lowest metallicity G8 simulation we can appreciate that accretion only appears to significantly modify the median DTM for $n_{\text{H}} \gtrsim 10^2 \text{ cm}^{-3}$. We note that the cold phase shows a significantly broader distribution in temperature, with the lowest DTM gas capable of reaching lower gas temperatures. To aid in this analysis, we have also included contour maps showing bins in T - n_{H} space that contribute 10^{-4} (dashed yellow) and 10^{-3} (solid yellow) to the total gas mass budget. This feature of low-DTM, low- T gas appears to be increasingly erased as the gas-phase metallicity is increased while maintaining the same properties of the G8 galaxy (i.e. gas fraction, stellar mass, SFR). We will further explore in Section 4.2.5 how the live dust modelling in CALIMA directly affects the equilibrium gas distribution, particularly the cold ISM. All metallicities show an overall lower DTM for $T \gtrsim 10^4 \text{ K}$, with clear signatures of thermal sputtering decreasing further the DTM for $T \gtrsim 10^6 \text{ K}$. However, the low metallicity run shows a consistently higher DTM at the very tip of the hot gas phase. We argue that this is the freshly injected dust from SN.

The growth, destruction and evolution of dust grains are highly dependent on their size, so we expect important variations in STL across different gas phases. The bottom row of Fig. 11 shows the same stacked histograms but colour-coded with STL. Small grains do not survive for long for $T \gtrsim 10^6 \text{ K}$, and the choice of large grain-dominated SN ejecta means that we do not see freshly injected small grains within SN-heated gas. For neutral gas, we find that the STL approaches overall values close to the ones used in the fixed dust simulations (~ 0.2), but there also regions (shown as white pixels) that also

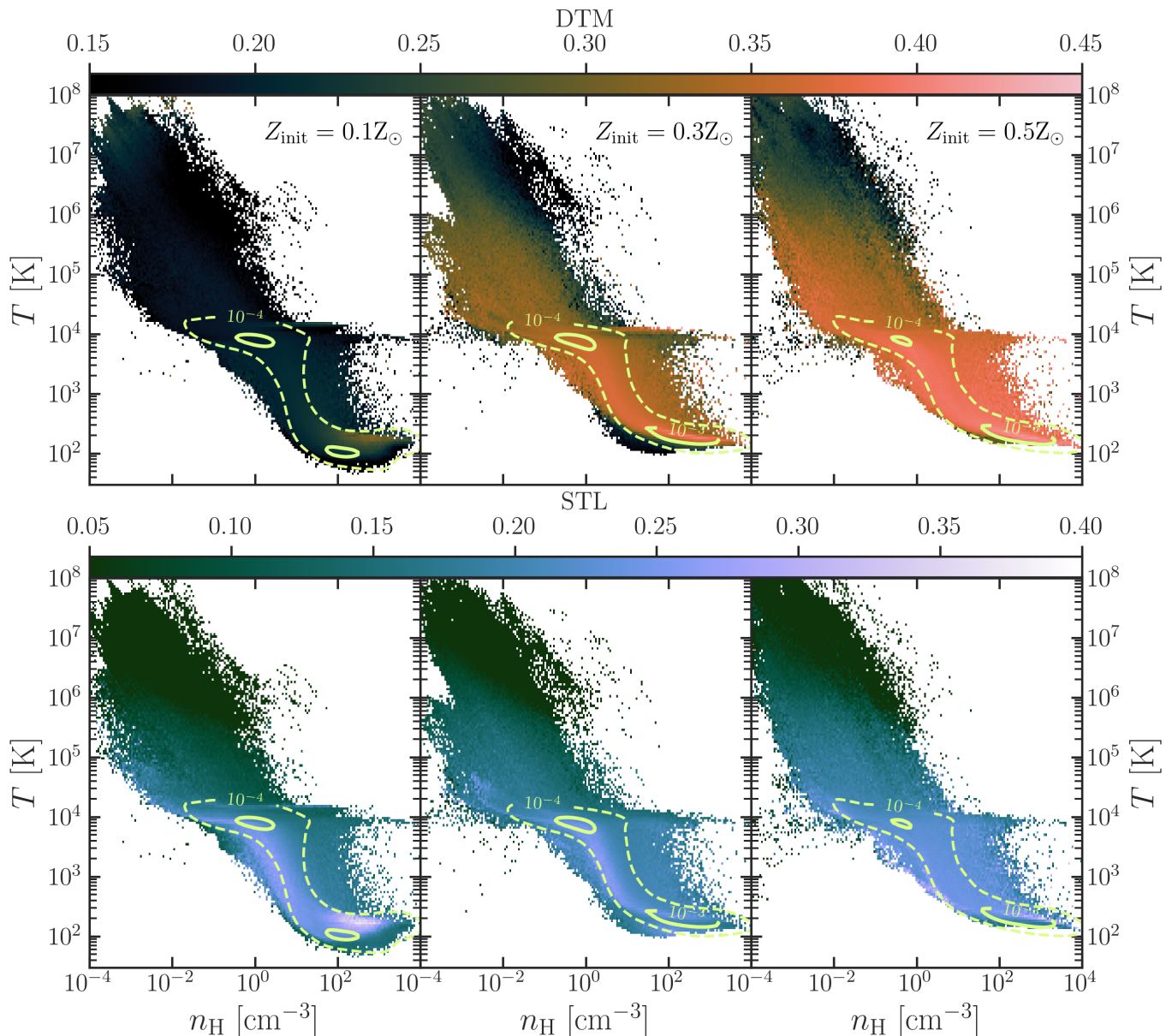


FIG. 11.—: Mass-weighted DTM (top row) and STL (bottom row) distributions for the temperature-density phase diagrams of the G8 simulations using CALIMA. These are computed by stacking all outputs between 100-200 Myr. Yellow contours indicate bins in T - n_{H} space that contribute 10^{-4} (dashed) and 10^{-3} (solid) to the total gas mass budget. Overall DTM increase is a stiff function of Z_{init} , with $Z_{\text{init}} = 0.1 Z_{\odot}$ showing a significantly lower DTM compared to the higher metallicity runs. All simulations show an overall lower DTM for $T \gtrsim 10^4$ K, with effective destruction of dust taking place for $T \gtrsim 10^6$ K. Small grains do not contribute for $T \gtrsim 10^6$ K and appear to show a larger contribution to the dust budget in a band following the shape of the mass distribution. Maximum values of STL decrease with Z_{init} , but the median value over the warm, diffuse ISM increases with Z_{init} .

indicate enhanced small grain abundance. The artificially enhanced metallicity of $0.5 Z_{\odot}$ (compared to the mass-metallicity relation) for a galaxy as low-mass as G8 results in a warm neutral and cold ISM with particularly high STL, but in the 0.1 and $0.3 Z_{\odot}$ simulations the high STL appears as band that follows the shape of the gas mass distribution (i.e. dashed and solid yellow contours). The low density warm ISM shows the effects of small grain production in the turbulent shattering of large grains, with efficient gas-phase accretion on small grains taking over at higher gas densities (see the high

STL cloud for $n_{\text{H}} \gtrsim 10^2 \text{ cm}^{-3}$ in the $Z_{\text{init}} = 0.1 Z_{\odot}$). We note that the cold gas that can cool well below 100 K shows low small mass fraction at high n_{H} , directly linking the growth of dust mass at high density to the minimum gas temperature of the cold phase.

A unique capability of CALIMA is its self-consistent calculation of grain charging in every simulation cell. Fig. 12 presents the mean charge for largeSil grains¹⁹

¹⁹ We do not show the mean charge for smallSil and the carbonaceous grains as the qualitative behaviour is similar to largeSil with only changes in relative charging.

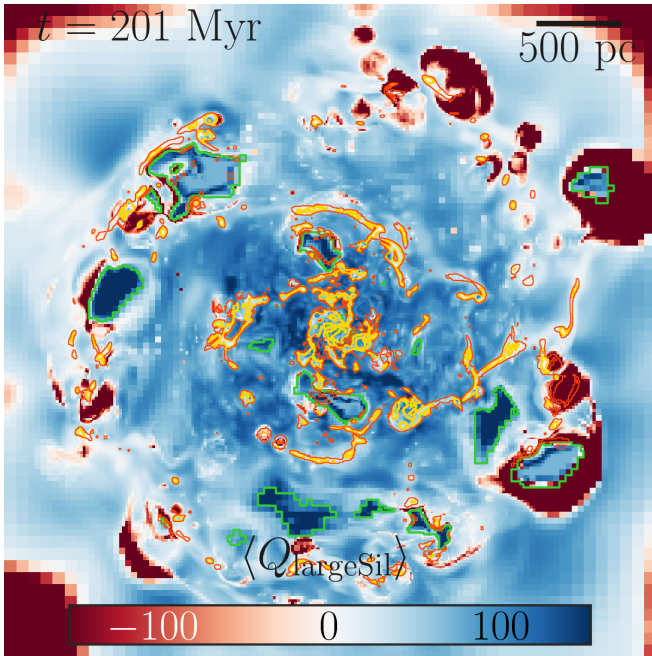


FIG. 12.—: Same projection as Fig. 10 but showing the density-weighted mean largeSil grain charge. Green line contours indicate ionised gas ($x_{\text{HII}} \geq 0.99$), yellow lines gas with $n_{\text{H}} \geq 10^2 \text{ cm}^{-3}$, and red lines dust collisional cooling rates exceeding $3 \times 10^{-27} \text{ erg s}^{-1}$. The inset shows a detailed view of a young H II region in which the transition from positively to negatively charge grains can be seen across the ionisation front, leading to enhanced dust collisional cooling.

in the G8 simulation with $Z_{\text{init}} = 0.3 Z_{\odot}$ at 200 Myr. The grain charge distribution is a result of the balance between photo-ejection and collisions with free electrons (see Section 2.2). Across most of the ISM, grains remain positively charged, though they approach neutrality in dense, shielded regions (highlighted by yellow contours, $n_{\text{H}} \geq 10^2 \text{ cm}^{-3}$). Inside H II regions (green contours indicate $x_{\text{HII}} \geq 0.99$), grains become highly positively charged due to the intense radiation field (high charging parameter γ). Notably, we observe a sharp transition to negative charges at the ionization fronts (see dark red cells in the inset). This is in agreement with our predictions for high $T \gtrsim 10^4 \text{ K}$ and low γ (Fig. 3): immediately outside the H II region, but lower G_0 —reducing photoelectric emission—while the free electron density remains sufficient to drive the equilibrium distribution toward the negative limit. As we have discussed, grain charging has an important effect in the evolution of dust grains as well as in their interaction with the ISM. For example, by modifying the effective cross-section of the grain due to Coulomb enhancement (see e.g. Section 2.4) ion collision rates with grains increase. This can affect, alongside other processes, the efficiency of collisional dust cooling (Section 2.6). In Fig. 12 we have also added red contour lines representing an excess of collisional cooling rate. The majority of these dust-cooled cells are co-spatial with the previously mentioned high gas density contours (dashed yellow lines). However, some of them are co-spatial with gas cells dominated by negative charge grains, easily distinguished in the H II re-

gion within the inset plot. We will further discuss the role of dust collisional cooling in Section 4.2.5.

Given the contentious nature of PAH formation from the gas phase (see the discussion in Section 3.3), a careful examination of the PAH abundance with respect to other dust mass content (i.e. q_{PAH}) is a subject that we will explore extensively in forthcoming work. Nonetheless, we provide preliminary analysis of q_{PAH} for the three G8 simulations in Fig. 13. We have computed these by stacking the results of all snapshots between 100–200 Myr, considering all gas cells inside a cylinder co-planar with the disc of radius 1.5 kpc and height of 2 kpc above and below the disc plane. To guide the eye, we also include solid red contours indicating the bins in T – G_0 that contribute 10^{-4} and 10^{-3} to the total gas mass budget. For the $Z_{\text{init}} = 0.3, 0.5 Z_{\odot}$ simulations (middle and right panels) the formation of PAH via C^+ accretion can clearly be distinguished as the horizontal region at $T \sim 100 \text{ K}$ extending towards low values of G_0 . In the modelling used for C^+ accretion, this process only becomes slightly efficient for anion and neutral PAHs, which requires highly shielded gas (as in e.g. TMC-1, Chen et al. 2022, where $A_V \gtrsim 4$). We also find that for these simulations, the values of $q_{\text{PAH}} \gtrsim 0.3\%$ are not limited to the cold ISM, but also extend to the warm neutral gas. This is a signature of efficient production of PAHs via shattering of dust grains in the turbulent warm ISM (Section 2.8). However, there is still a clear distinction in PAH size between these two phases. We have included contours indicating the regions where the mass-weighted STL_{PAH} exceeds 0.2 (dashed lime lines) and 1.0 (solid lime lines). It shows that for these metallicities, the low G_0 and low T phases are dominated by largePAHs (i.e. to the left of the dashed lines), while there is a dominant contribution of small-PAHs at cold and warm phases with $G_0 \gtrsim 10^2$. This overabundance of smallPAHs in this ISM phase is caused by the transfer of mass from largePAHs to smallPAHs via cluster evaporation (Section 3.7). We note that this prediction is in direct contradiction with the suggested dominance of large PAHs close to ionising sources (e.g. Knight et al. 2021; Baron et al. 2025; Chown et al. 2024). Nevertheless, we still recover the efficient destruction of PAHs in ionised gas ($T \gtrsim 10^4 \text{ K}$) with $G_0 \gtrsim 10$ – 100 , as suggested by the decrease of PAH mid-IR emission to total IR emission within H II regions (e.g. Chastenet et al. 2023; Egorov et al. 2023; Egorov et al. 2025).

In the low-metallicity simulation ($Z_{\text{init}} = 0.1 Z_{\odot}$), q_{PAH} growth via accretion is strongly suppressed by the reduced abundance of gas-phase C^+ . This strong dependence on metallicity for the growth of PAHs is in agreement with observationally inferred PAH abundances in the local (e.g. Draine et al. 2007; Galliano et al. 2008a; Rémy-Ruyer et al. 2015; Whitcomb et al. 2024) and high-redshift Universe (e.g. Shivaie et al. 2017; Shivaie et al. 2024). Consequently, the majority of PAHs reside in the diffuse, irradiated ISM, identifying the shattering of carbonaceous grains as the dominant mechanism driving PAH evolution in low-metallicity environments. Given also the low abundance of smallPAHs, clustering is not sufficiently efficient, rendering the phases with larger q_{PAH} dominated by smallPAHs.

We further explore the evolution of PAHs from the diffuse to the high ionisation medium using the unique capa-

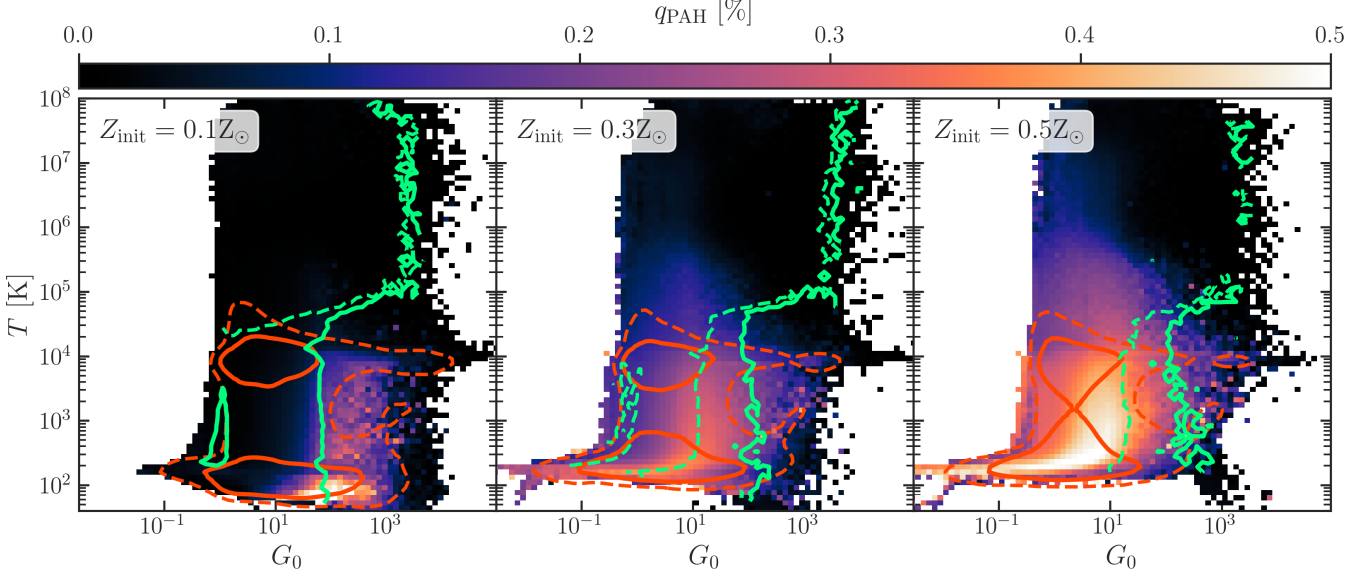


FIG. 13.—: Mass-weighted distribution of q_{PAH} for different gas temperatures and Habing band strengths G_0 . This is a result of stacking all snapshots for the G8 simulations with CALIMA between 100–200 Myr, including all gas within a cylinder centred on the galaxy with radius 1.5 kpc and height below and above the disc of 2 kpc. Red contour lines indicate the regions where individual T – G_0 bins contribute 10^{-4} (dashed) and 10^{-3} (solid) to the total gas mass budget in the cylinder. Lime open contours show regions with $\text{STL}_{\text{PAH}} \geq 0.2$ (right side of dashed lines) and with $\text{STL}_{\text{PAH}} \geq 1$ (right side of solid lines). PAHs are more abundant for highly shielded and cold gas, quickly becoming destroyed for $G_0 \gtrsim 10^2$ and $T \gtrsim 10^4$ K. In the lowest metallicity galaxy (left panel) PAHs are predominantly present next to cool, irradiated gas, resulting from destruction processes of carbonaceous dust grains. Large PAHs dominate for $T \gtrsim 10^5$ K for all metallicities and G_0 , becoming important in the diffuse gas at lower G_0 for lower metallicities. Large PAHs dominate the cold, shielded gas. Small PAHs are more important in the low T , high G_0 gas.

bilities of CALIMA. Observationally, the relative amount of PAH mass to dust mass (i.e. q_{PAH} is usually computed by comparing the IR luminosity in the MIR to the total IR luminosity (e.g. Engelbracht et al. 2005; Sandstrom et al. 2010; Chasten et al. 2023; Sutter et al. 2024). In order to compute the IR luminosity of each region of our G8 simulations, we have performed mock data cubes using the Monte-Carlo radiative transfer code SKIRT (Camps & Baes 2015; Baes et al. 2022). These have been obtained for the three metallicity simulations at 200 Myr, obtaining face-on data cubes with a resolution of ~ 4 pc per pixel and the full spectrum from $0.09 \mu\text{m}$ to $1000 \mu\text{m}$. Stellar sources for radiation are taken from the stars formed during the simulation runtime and sourcing photon packets from the BPASS v2.2.1 SED (Stanway & Eldridge 2018) using the same settings as we have used in the simulations and considering their age, metallicity and initial mass. Absorption of UV-optical light is taken into account using the predicted abundances and properties of each dust and PAH bin for each simulation cell, following the optical properties and underlying GSD for each bin used in CALIMA. We compute an observed proxy of q_{PAH} as defined by the parametrisation (Egorov et al. 2025):

$$R_{\text{PAH}}^* = \frac{2.57 \times \text{F770W}_{\text{SS}}}{C \times \text{F2100W}}, \quad (45)$$

where F2100W is the flux density in the JWST F2100W filter, $\text{F770W}_{\text{SS}} = \text{F770W} - 0.22 \times \text{F300M}$ is the starlight-subtracted correction of F770W flux density using the F300M filter (Sutter et al. 2024), and $C = -8.32 \times$

$10^{-3} \log(L_{\nu}(\text{F770W}_{\text{SS}}))^2 + 0.4881 \log(L_{\nu}(\text{F770W}_{\text{SS}})) - 6.01$ is a correction to account for the missing information from the F1130W filter. In Egorov et al. (2025) the H II region ionisation parameter is measured using the proxy given by the $[\text{S III}]_{\lambda 9069,9532\text{\AA}}/[\text{S II}]_{\lambda 6717,6731\text{\AA}}$ line ratio. These can be directly obtained since RAMSES-RTZ tracks the non-equilibrium abundances of individual ion populations, allowing trivial face-on projections (also at ~ 4 pc resolution) of the luminosity between the $[\text{S III}]$ and $[\text{S II}]$ lines. In practice, the $[\text{S III}]_{\lambda 9532\text{\AA}}$ line lies beyond the MUSE wavelength range used in Egorov et al. (2025), and instead they use the theoretical ratio $[\text{S III}]_{\lambda 9532\text{\AA}} = 2.5 \times [\text{S III}]_{\lambda 9069\text{\AA}}$. We apply the same strategy for these mock observational analysis. We note that our comparison is not fully on the same grounds as the original observational sample: we do not introduce instrumental noise, nor convolve our images to the spatial resolution of the observations performed with JWST and MUSE. Furthermore, we do not perform circular integration around each H II region, and instead obtain R_{PAH}^* and $\log([\text{S III}]/[\text{S II}])$ on a per-pixel basis. However, we limit our analysis to pixels that have a sufficiently high $[\text{S III}]_{\lambda 9069\text{\AA}}$ luminosity compared to $\text{H}\alpha$ (i.e. $L([\text{S III}]_{\lambda 9069\text{\AA}})/L(\text{H}\alpha) \geq 0.3$).

In the G8 simulations, individual pixels span a range of $\log([\text{S III}]/[\text{S II}])$ and R_{PAH}^* comparable to the low-metallicity ($12 + \log(\text{O}/\text{H}) < 8.2$) H II regions and SNRs studied by Egorov et al. (2025). Given the low metallicity of the simulations explored in this work, we do not reproduce the observed R_{PAH}^* for their high metallicity sample ($12 + \log(\text{O}/\text{H}) > 8.2$, red contour lines), al-

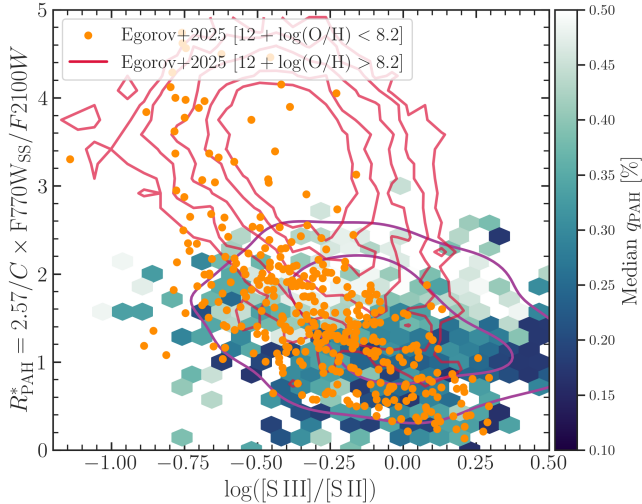


FIG. 14.—: Histogram of an observational proxy of the PAH mass fraction, R_{PAH}^* (Egorov et al. 2025), against an observational proxy of the ionisation parameter, the $[\text{S III}]_{\lambda 9069,9532 \text{ \AA}}/[\text{S II}]_{\lambda 6717,6731 \text{ \AA}}$ line ratio. Hexagonal bins show the location of H II regions in the G8 simulations using CALIMA, colour coded by the median q_{PAH} in each bin. Magenta contours indicate the 70th and 90th percentile of the pixel distribution. We include the observations of individual H II regions and SNR from the PHANGS survey extracted in Egorov et al. (2025), separated in their low metallicity bin ($12 + \log(\text{O}/\text{H}) < 8.2$, orange points) and high metallicity bin ($12 + \log(\text{O}/\text{H}) > 8.2$, red contours). The distribution of H II regions in the G8 simulations agree with the low metallicity bin, but there is no clear trend between R_{PAH}^* and q_{PAH} .

though a subset of pixels begins to populate that region. Despite the broadly consistent trend of lower R_{PAH}^* for higher $\log([\text{S III}]/[\text{S II}])$, there are notable differences from the observed data. For $\log([\text{S III}]/[\text{S II}]) \gtrsim 0$, the simulations predict systematically higher R_{PAH}^* compared to the low metallicity distribution, although these have preferentially lower q_{PAH} . These results combined into a shallower distribution, as shown by the 70th and 90th percentile contours (magenta lines). This could be another indicative of slow PAH destruction in high ionisation environments, as we have mentioned in the analysis of Fig. 13. We have colour coded the bins in this histogram with the median q_{PAH} , which appear to show a preference of higher q_{PAH} for higher R_{PAH}^* and lower $\log([\text{S III}]/[\text{S II}])$. However, the limited number of H II regions in just three simulations does not provide a reliable statistics, making a correlation between R_{PAH}^* and q_{PAH} . In addition, it appears that while the simulations indicated q_{PAH} values exceeding 0.5%, the gas cells that are sampled by these observations do not appear to be a direct measure of the median q_{PAH} in the G8 galaxies. We emphasise that these mock observations have not been fully tailored for a one-to-one comparison with Egorov et al. (2025), but they already suggest that the relationship between observational PAH mass parametrisations and the underlying PAH mass budget is non-trivial and warrants further investigation (e.g. Sandstrom et al. 2010; Sutter et al. 2024). This comparison also illustrates

the unique capability of CALIMA to link theoretical models of dust and PAH evolution to direct observables.

4.2.3. Radiation transfer with evolving dust properties

As we saw in Fig. 13, the value of G_0 can vary by many orders of magnitude at a given gas temperature. In our equilibrium tests (Section 4.1) we assumed a fixed value of $G_0 = 1$, therefore affecting the relative role of different heating mechanisms (i.e. PEH, H_2 pumping, etc.) and the abundance of molecules and PAHs. In our G8 simulations the value of G_0 is instead the result of the radiation emitted by stars formed and how it has been propagated through the ISM by RAMSES-RT. Fig. 15 shows the distribution of G_0 in mass-weighted projections of the G8 simulations with $Z_{\text{init}} = 0.3 Z_{\odot}$. We begin by examining the properties of the radiation field in the fixed dust simulations (right panels). We have calculated the mass-weighted distributions of G_0 for the separation of the ISM phases suggested by Kim & Ostriker (2017) based on the natural breaks in the temperature distribution of the Z_{\odot} ISM: 1) cold ($T < 184 \text{ K}$), 2) unstable ($184 \text{ K} < T < 5050 \text{ K}$), 3) warm ($5050 \text{ K} < T < 2 \times 10^4 \text{ K}$), 4) ionised ($2 \times 10^4 \text{ K} < T < 5 \times 10^5 \text{ K}$), and 5) hot ($T > 5 \times 10^5 \text{ K}$). The projection shows an average $G_0 \sim 1$ in the diffuse ISM, as supported by the location of the distribution peak. This projection also shows very localised variations of G_0 , attributed to high density, shielded clumps and filaments that have not formed stars yet, and the ones that are actively star-forming. This is the source of the broadness of the cold phase distribution in G_0 , spanning more than four orders of magnitude. The distribution of the rest of phases also show a significant broadness in G_0 , but they quickly drop for $G_0 \lesssim 1$. The similarity in the shape of these distributions for $G_0 > 1$ is a clear signature of the non-evolving dust abundances and properties of the fixed dust model.

The left panels of Fig. 15 compares the results of the fixed dust model to the G8 simulation using CALIMA. We note that both simulations have very similar star-formation rates²⁰, so the comparison in G_0 distributions can be considered to probe the transparency of the ISM between the CALIMA simulation and the fixed dust model. Already a qualitative comparison of the two projections indicate significant differences between the two models: young star-forming regions have much larger G_0 , while the obscuration of clumps and filaments appears to stand out even more against the diffuse background. This is clearly supported by the mass-fraction distribution of G_0 for the cold phase, showing a greater contribution of the values of G_0 away from $G_0 \sim 1$. This is a direct result of the varying DTM and STL across ISM phases allowed by CALIMA. In both projections we have included blue (red) contours indicating regions in which the local DTM exceeds (lags) the median DTM across the disc. It is clear that large dust destructions in the inner region of the disc (recall the DTM cavity observed in Fig. 10) gives rise to less obscure young star formation, while the growth of dust via accretion gives rise to regions of enhanced DTM and therefore lower G_0 . This result even extends to the unstable phase, with a tail towards $G_0 \sim 10^{-2}$ which was not present in the fixed dust model. For the rest

²⁰ All G8 simulations show star-formation rates, averaged over 10 Myr, in the range of $\sim 0.02 - 0.04 M_{\odot} \text{ yr}^{-1}$.

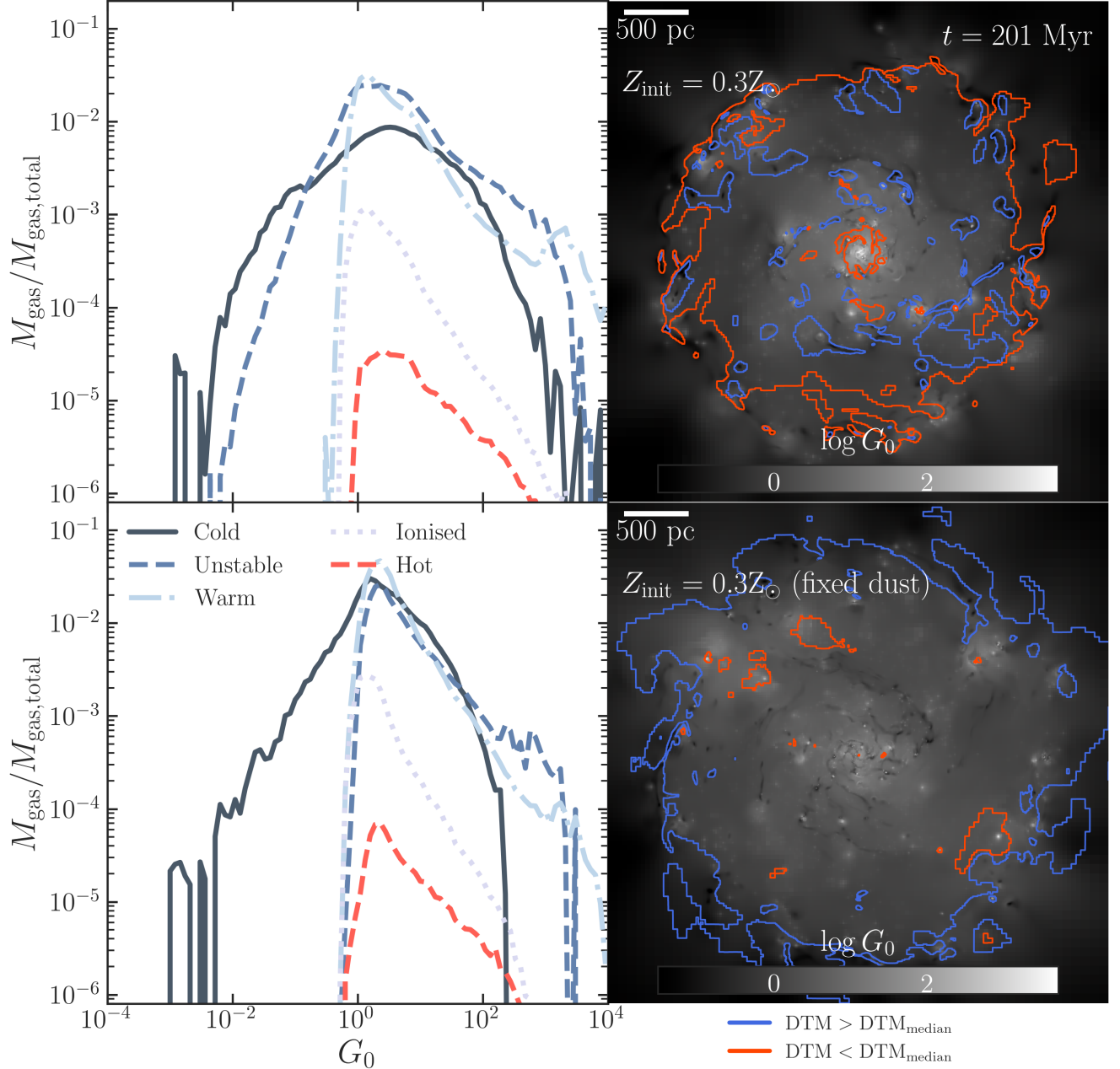


FIG. 15.—: Comparison of G_0 distribution for the G8 galaxy with $Z_{\text{init}} = 0.3 Z_{\odot}$ in the case of using CALIMA or a fixed dust evolution. Right panels are mass-weighted projections of G_0 with a width of 4 kpc and a depth of 0.8 kpc. To the left of each projection, we include the fraction of gas mass contributed by each bin to the total gas mass budget. We have also separated the gas mass within five different phases, using the natural breaks in the gas temperature distribution. Blue (red) contour lines indicate regions in which the local DTM exceeds (lags) the mass-weighted median DTM of each simulation. While with a fixed dust the distribution of G_0 is highly clustered around ~ 1 , CALIMA predicts broader distributions, with shifted peaks for different phases.

of phases, the distribution still shows a hard cut-off for $G_0 \sim 1$, but with broader peaks and larger contribution of cells with $G_0 \gtrsim 10^2$. These results clearly demonstrates the non-trivial properties of the ISRF with on-the-fly radiative transfer and self-consistent modelling of dust evolution.

4.2.4. Influence of dust on the molecular and neutral ISM

A direct consequence of variable dust content, grain properties, and G_0 is a variable efficiency of H_2 for-

mation in the ISM of the G8 galaxy. We explore the abundance of H_2 with respect to total hydrogen mass at different n_{H} in Fig. 16 by computing 2D mass-weighted histograms for the G8 simulation with $Z_{\text{init}} = 0.1 Z_{\odot}$ and using CALIMA. These are a stack of all simulation snapshots between 100–200 Myr, using only cells within a cylindrical volume centred in G8 with radius 1.5 kpc and height above and below the disc of 2 kpc. The median of the distributions for H I (dotted), H II (dashed) and H_2 (solid) are given by the green lines included over

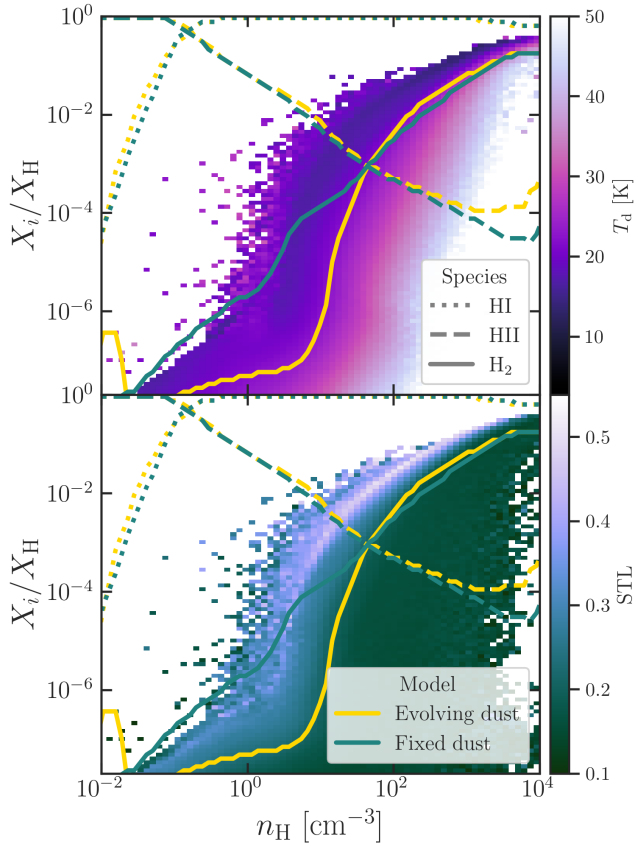


FIG. 16.—: Mass-weighted histogram of the fraction of hydrogen in H_2 at different n_{H} for all outputs between 100–200 Myr of the G8 simulation with $Z_{\text{init}} = 0.1 Z_{\odot}$. The dashed, dotted, and solid lines show the median HI, H II and H_2 , respectively. In the top panel we show the mass-weighted dust equilibrium temperature, and in the bottom panel the mass-weighted STL. For comparison, we also include the median HI, H II and H_2 for the equivalent G8 simulation with fixed DTM. CALIMA predicts a lower (higher) efficiency of H_2 formation for $n_{\text{H}} \lesssim 10 \text{ cm}^{-3}$ ($n_{\text{H}} \gtrsim 10 \text{ cm}^{-3}$) than with the fixed DTM model. Cells that at a fixed n_{H} have a higher H_2 fraction are dominated by cold dust ($\lesssim 20 \text{ K}$) and a larger fraction of small grains $\text{STL} \gtrsim 0.3$.

the 2D histograms of H_2 . We have colour coded the H_2 distribution with mass-weighted median dust temperature (top panel) and STL (bottom panel). We can see that the median mass distribution goes from being dominated by H II to HI at $n_{\text{H}} \gtrsim 0.1 \text{ cm}^{-3}$. Molecular hydrogen is negligible for $n_{\text{H}} \lesssim 10 \text{ cm}^{-3}$, steeply growing in mass fraction around this density and then developing a shallower slope with n_{H} . We compare the behaviour of the CALIMA simulation to the one with fixed dust (green lines). The largest difference with the CALIMA simulation is the evolution of the median H_2 mass fraction with n_{H} : the fixed dust model predicts much higher (up to three dex) molecular fraction for $n_{\text{H}} \lesssim 10 \text{ cm}^{-2}$, while above this density CALIMA predicts consistently larger H_2 fractions. In the equilibrium tests performed in Section 4.1 we also drew attention to this enhanced H_2 fraction using CALIMA compared to a fixed dust model. However, with higher DTM in the cold phase and in the presence

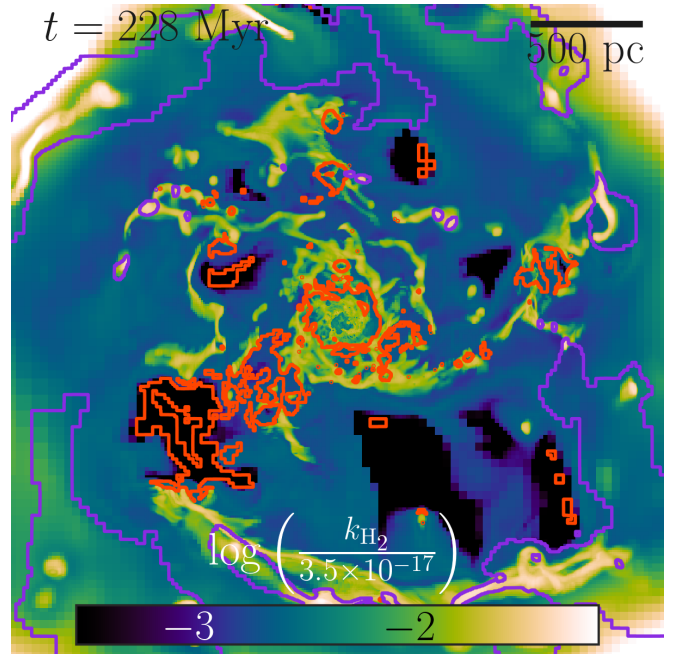


FIG. 17.—: Mass-weighted projection of the H_2 formation coefficient k_{H_2} for the G8 simulation with $Z_{\text{init}} = 0.1 Z_{\odot}$ at $t = 228 \text{ Myr}$. The rates have been normalised to the canonical value of $3.5 \times 10^{-17} \text{ cm}^3 \text{ s}^{-1}$ used in thermochemistry models including H_2 formation on dust grains (e.g. Gnedin et al. 2009; Bialy & Sternberg 2019). Red contours contain gas cells with dust temperature exceeding 30 K, while purple contours show regions where STL is larger than 0.35. Our predicted k_{H_2} only approaches the canonical for the highly shielded, dense clumps and filaments (inside purple contours), with the majority of the gas showing more than 2 dex slower H_2 formation, particularly where hot dust lives (i.e. inside red contours).

of self-shielding, the allowed H_2 fraction exceeds the predictions of the equilibrium model (see also Katz et al. 2022, for similar conclusions).

Molecular hydrogen formation on dust grains is considered to depend on the composition, size and temperature of the grain (Cazaux & Tielens 2002; Cazaux et al. 2004). By linking the dust properties to the H_2 formation, we are capable of directly predicting how an evolving dust distribution affects the H_2 fraction. The mass-weighted dust temperature shows that the median of the H_2 forming gas has dust with $T_{\text{d}} \sim 20 \text{ K}$ at low densities, and $T_{\text{d}} \lesssim 15 \text{ K}$ at higher gas densities. At a fixed density, the molecular gas fraction is larger in cells that both show a lower T_{d} and higher STL. This effect of higher efficiency caused by larger mass fraction of small grains, is particularly clear for densities around the critical density for H_2 formation ($n_{\text{H}} \sim 1\text{--}10 \text{ cm}^{-3}$). The reaction rate for H_2 formation in ISM models is usually set by (e.g. Gnedin et al. 2009; Bialy & Sternberg 2019):

$$R_{\text{d}} = k_{\text{H}_2} f_{\text{DTG}} C \sqrt{\frac{T}{100 \text{ K}}} \quad [\text{cm}^3 \text{ s}^{-1}], \quad (46)$$

where, f_{DTG} is the ratio of the local DTG to the mean value of the MW, C is a clumping factor, and the coefficient k_{H_2} with the empirically derived value of 3.5×10^{-17}

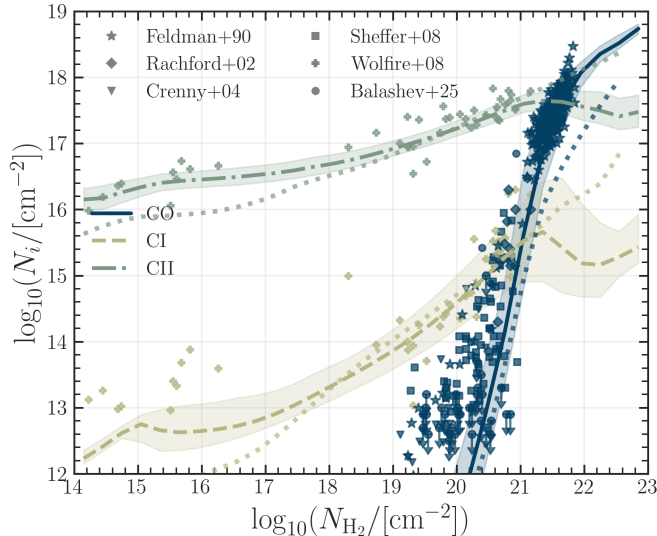


FIG. 18.— Median CO (solid blue), C I (dashed olive), and C II (dash-dotted seagreen) column densities for a stack of G8 ($Z_{\text{init}} = 0.1 Z_{\odot}$) snapshots from 100–200 Myr. Dotted lines indicate the equivalent medians but for the G8 simulation with fixed DTM. For comparison, we include the observations from galactic sight lines from Federman et al. (1990), Rachford et al. (2002), Crenny & Federman (2003), Wolfire et al. (2008), Sheffer et al. (2008) and for LMC and SMC sight lines (in absorption) from Balashev et al. (2025). CALIMA improves on the fixed dust modelling across all densities and C-bearing species (particularly for CO at high N_{H_2}), although the abundance of CI at low column densities remains low compare to observations.

by Wolfire et al. (2008). To further exemplify the influence of our live dust modelling on the H_2 formation efficiency, we show in Fig. 17 the effective local k_{H_2} for the CALIMA G8 simulation with $Z_{\text{init}} = 0.1 Z_{\odot}$ at $t = 228$ Myr. We have normalised this coefficient by the canonical value of 3.5×10^{-17} , such that for the same DTG, gas temperature and clumping factor, the influence of grain size and temperature drives deviations from the empirical value from Wolfire et al. (2008). The first result that can be extracted is that across the entire G8 galaxy the value of k_{H_2} is much lower than 3.5×10^{-17} . It only approaches this value within highly shielded and dense clumps. We also include purple contours indicating regions where the local STL exceeds 0.35, which are clearly linked with clumps of high H_2 efficiency. The diffuse ISM shows formation coefficients up to 2 dex lower than the canonical, particularly within regions that are dominated by high dust temperature (shown as red contours). We argue that since at fixed DTM the H_2 efficiency increases for a larger STL (i.e. larger surface-to-mass ratio) and decreases for larger dust temperature (i.e. due to lower residence time by adsorbed hydrogen), k_{H_2} is much lower in the ISM of a $0.1 Z_{\odot}$ galaxy for which the diffuse ISM is more transparent and the growth of small grains is halted due to low gas-phase abundance of metals. This variability is a direct benefit from an H_2 formation model coupled to an evolving grain size distribution and with on-the-fly radiative transfer.

As we have emphasised before, our G8 simulations do

not allow a direct comparison to a system like the Small Magellanic Cloud (SMC), even less for the Large Magellanic Cloud (LMC) or the MW. Despite this, comparing column densities of the ions and molecules tracing the molecular and neutral ISM is useful to understand the details of our model (e.g. Gong et al. 2019; Hu et al. 2021; Katz et al. 2022; Thompson et al. 2024). In Fig. 18 we have included observations for the column densities of H_2 , CO, C I and C II for various sight lines in the Magellanic Clouds and in the MW (Federman et al. 1990; Rachford et al. 2002; Crenny & Federman 2003; Sheffer et al. 2008; Wolfire et al. 2008; Balashev et al. 2025). Simulation results are obtained for the CALIMA simulation with $Z_{\text{init}} = 0.1 Z_{\odot}$ ²¹ by stacking all outputs between 100–200 Myr. Shaded regions indicate the second and third quartiles of the distribution of values at each H_2 column density N_{H_2} bin. We have also included the results for the equivalent G8 simulation but with fixed dust as dotted lines. We can see that the CALIMA model improves upon the predictions from the fixed dust model, by allowing for a larger CO abundance at $N_{\text{H}_2} \gtrsim 10^{21} \text{ cm}^{-2}$, and larger abundances of C I and C II at lower densities caused by lower DTM in the diffuse neutral gas. The boost in N_{CO} can be explained by a larger H_2 abundance at fixed DTM in CALIMA (see Fig. 16 for $n_{\text{H}} \gtrsim 10 \text{ cm}^{-3}$ and the equilibrium curve in Fig. 9).

4.2.5. Quantifying the relative role on the ISM of heating and cooling processes linked to dust and PAHs

We have established that at the same initial gas-phase metallicity, the G8 simulation using CALIMA results in larger H_2 mass fractions at $n_{\text{H}} \gtrsim 10 \text{ cm}^{-3}$ than a fixed dust model. Since H_2 can heat the gas by formation, dissociation, and UV pumping (see section 2.2.4 in Katz et al. 2022, for the modelling included in CALIMA), a larger H_2 fraction motivates an examination of the role of H_2 heating in the thermal state of the ISM. In order to explore the influence of an evolving dust and PAH population in the thermo-chemical properties of the ISM, we show in Fig. 19 the fractional contribution of (from left to right) photo-electric heating (PEH), H_2 heating, dust and PAH recombination cooling, and dust collisional cooling to the total heating (Γ_{total}) and total cooling (Λ_{total}). These fractional quantities are computed on a per-cell basis, and the final 2D histogram is constructed as the median mass-weighted value at each T - n_{H} bin for the stack of simulation outputs between 100–200 Myr for the G8 simulations with $Z_{\text{init}} = 0.1 Z_{\odot}$ with CALIMA (top row) and fixed dust (bottom row) models. Consistent with the analysis performed in previous sections, we only consider gas within a cylinder centred on G8 with radius 1.5 kpc and height below and above the disc of 2 kpc. To further guide the relevance of each process to the bulk of the ISM, we have also included yellow contour lines to indicate which bins in T - n_{H} space contribute 10^{-4} (dashed lines) and 10^{-3} (solid lines) to the total gas mass budget.

As described in Section 4.2.1, we initialised the G8 simulations with a fixed DTM and q_{PAH} based on their gas-phase metallicity and the scalings in Rémy-Ruyer et al.

²¹ We use the low metallicity simulation for this comparison with observations due to its more realistic gas-phase metallicity for a galaxy with a stellar mass of $10^8 M_{\odot}$ (e.g. Andrews & Martini 2013).

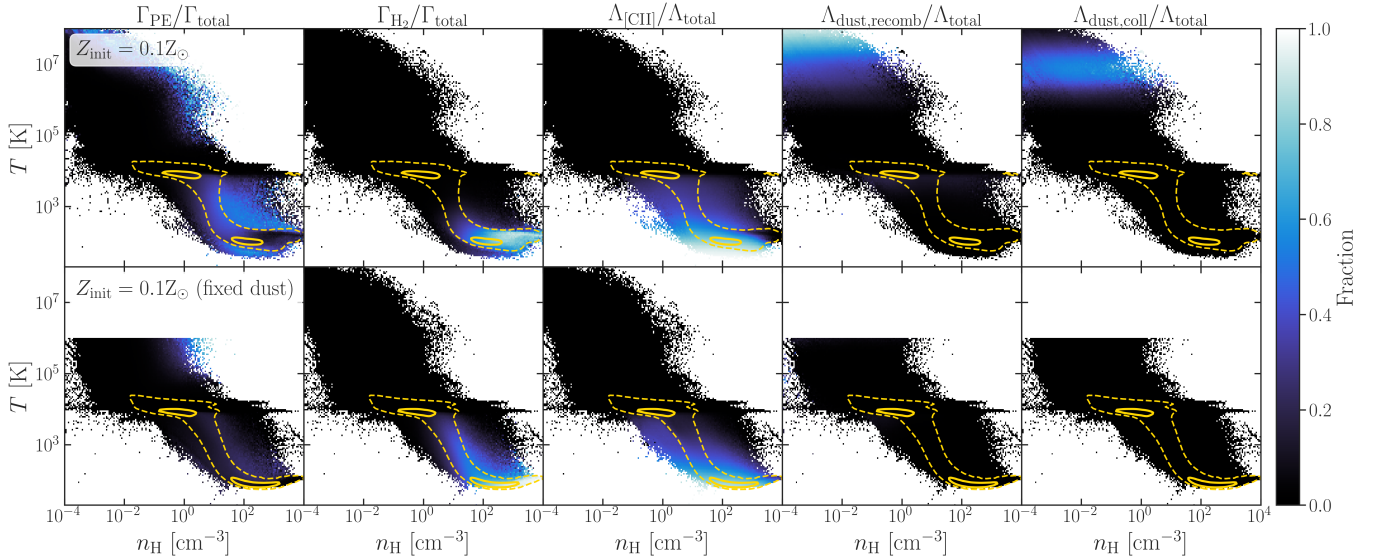


FIG. 19.—: Temperature-density diagrams for the G8 simulation with $Z_{\text{init}} = 0.1 Z_{\odot}$ showing the fraction of total contribution of heating and cooling processes—with direct link to dust and PAH evolution—to the total heating and cooling rates. These have been computed for a cylindrical region centred on the G8 galaxy with radius 1.5 kpc and height below and above the disc of 2 kpc. We also include yellow contours indicating bins in T – n_{H} space that contribute 10^{-4} (dashed lines) and 10^{-3} (solid lines) to the total gas mass budget. The top row is for the CALIMA model while the bottom row is for the fixed dust simulation.

(2014, 2015). Without dust and PAH evolution (only injection of dust by SN and PAHs by AGB winds) the G8 simulation with $Z_{\text{init}} = 0.1 Z_{\odot}$ and fixed dust model maintains a value of $q_{\text{PAH}} \sim 1\%$, more than twice the maximum values measured for the G8 simulation using CALIMA (see middle panel Fig. 13). Despite this difference, the fractional contribution of PEH within the diffuse unstable and cold phases is significantly increased in the CALIMA simulation compared to fixed dust. In the classical implementation of PEH, the heating rate is dependent on the charging parameter γ , the dust-to-gas ratio, and the abundance of PAHs (e.g. Katz et al. 2022), therefore becoming independent from the shape of the ISRF, the grain and PAH size distribution, the grain composition and/or the grain/PAH charge (see Sections 2.3 and 3.5). CALIMA raises important concerns about the effectiveness in capturing the variability (and full efficiency) of PEH with the classical implementations, using a single ISRF, a fixed GSD and dust/PAH properties. In future work, we will explore further the comparison between classical approaches and the self-consistent modelling of PEH for dust and PAHs in CALIMA (Rodríguez Montero et al., in prep.). We note that at low densities, the dominant heating mechanism is CR heating (see e.g. Figure 11 in Katz et al. 2022).

In terms of H_2 heating, the CALIMA model indeed shows a much larger range in density in which it affects or dominates the heating of the cold ISM, as a consequence of a larger H_2 fraction. We find that this region of enhanced H_2 heating aligns with the contours indicating the bulk gas mass distribution, thus positioning H_2 heating as an important driver of the dominant equilibrium distribution for the CALIMA simulation. When compared to the fixed dust simulation, this histograms show that while both simulations converge to similar equilibrium temperatures for $n_{\text{H}} \sim 10^4 \text{ cm}^{-3}$, the CAL-

IMA simulation shows a broad distribution in temperature for $n_{\text{H}} \sim 10^2 \text{ cm}^{-3}$. Additionally, H_2 appears to play a more significant role at $n_{\text{H}} \lesssim 10 \text{ cm}^{-3}$, as expected due to the higher H_2 fraction at these lower gas densities in the fixed model (see Section 4.2.4). Overall, the equilibrium gas distribution appears to lack the minimum in gas temperature at these densities observed in the fixed dust models. This goes in agreement with the results obtained for the equilibrium tests (see Section 4.1), where we argued this to be the consequence of large H_2 heating due to more efficient formation, and a lower $[\text{C II}]$ cooling caused by efficient C^+ accretion by carbonaceous dust grains at $n_{\text{H}} \sim 10^2$ – 10^4 cm^{-3} . To test this, the central column in Fig. 19 shows how the fractional contribution of $[\text{C II}]$ cooling differs from CALIMA to the fixed dust model. While the low temperature gas at $n_{\text{H}} \sim 10^2 \text{ cm}^{-3}$ shows a dominant contribution of $[\text{C II}]$ cooling, the variable DTM (i.e. see top left panel in Fig. 11) and the accretion of C^+ leads to a lower contribution of $[\text{C II}]$ cooling along the bulk of the gas mass distribution. This leads to a warmer unstable and cold phases of the ISM. We caution that these results are subject to our choice of initial conditions (i.e. low gas fraction, high metallicity, low star formation). However, this may point towards the possibility of using the thermal properties of the ISM (together with observations of $[\text{C II}]$) to constrain uncertain parameters in current dust accretion models.

To mimic thermal sputtering of dust and PAHs, in Katz et al. (2022) dust processes are turned off for $T > 10^6 \text{ K}$, which can be seen as the sharp cuts for dust-mediated processes above this gas temperature. While this may be a useful approximation, it appears to completely miss the role of dust recombination cooling and collisional cooling, as these appear to have an important role for gas temperatures above 10^6 K . The up-

dated modelling of dust thermal sputtering and collisional cooling (see Sections 2.5 and 2.6) result in SN heated gas to retain its dust mass for sufficiently longer timescales to allow a non-negligible contribution of these processes to the cooling. In fact, for the very high temperatures ($\sim 10^7$ – 10^8 K) dust recombination can dominate the cooling of the gas. We also find that CALIMA predicts a non-negligible ($\sim 20\%$) contribution from recombination cooling for warm gas between $\sim 10^3$ – 10^4 K, in agreement with the original predictions from (e.g. Bakes et al. 1994; Weingartner & Draine 2001a).

5. DISCUSSION

5.1. Comparison to previous dust models

In Section 1, we highlighted the recent surge of interest in dust evolution models, driven in part by the comprehensive overview of current approaches compiled by Parente et al. (2025). This renewed focus is motivated both by the need for self-consistent forward modelling of observations from ALMA and JWST across cosmic time, and by the demand for theoretical frameworks that capture the coupled evolution of dust, PAHs, and the multi-phase ISM. Much of the modelling developed in this work builds directly on the progress made by earlier implementations in the literature. To place CALIMA in this broader context, we summarise in Table 3 the dust and PAH processes included in our framework, and indicate the extent to which each has been implemented for the first time within a galaxy formation or ISM thermo-chemistry model.

CALIMA is based on the original implementation of live dust modelling within RAMSES introduced in Dubois et al. (2024). The modelling here has many features inherited from Dubois et al. (2024): a two-size approximation for regular dust grains, separation in carbonaceous and silicate compositions, log-normal distributions in each size bin, implementations for dust destruction in SN shocks and hot gas, shattering and coagulation, as well as a sub-grid turbulence model for gas-phase metal accretion. Despite these similarities, CALIMA include fundamentally different approaches to the coupling between dust evolution and the ISM. The modelling in Dubois et al. (2024) did not include on-the-fly radiative transfer, cooling/heating was not treated in the fully explicit, non-equilibrium approach in RAMSES-RTZ, but rather by indirectly affecting the cooling due to a lowering of the effective total metallicity Z used in the tabulated cooling rates in RAMSES from Sutherland & Dopita (1993) above 10^4 K and from Dalgarno et al. (1972) below 10^4 K. In order to isolate the influence of different choice of dust modelling, we have run the same equilibrium test runs as in Section 4.1 but at a lower metallicity of $0.1Z_{\odot}$. The thermo-chemistry parameters are chosen to be the same, but we modify the choice of dust evolution modelling:

- Accretion does not consider the predictions from grain charging and the gas-phase ion abundances, but instead assume that Coulomb factor $F_C = 1$, except for largeC and smallSil grains in the CNM with $T < 2 \times 10^4$ K and $n_H > 10 \text{ cm}^{-3}$, for which Dubois et al. 2024 adopted $F_C(0.1\mu\text{m}) = 0$ and $F_C(0.5\text{nm}) = 10$.
- Coagulation follows the modelling in Aoyama et al.

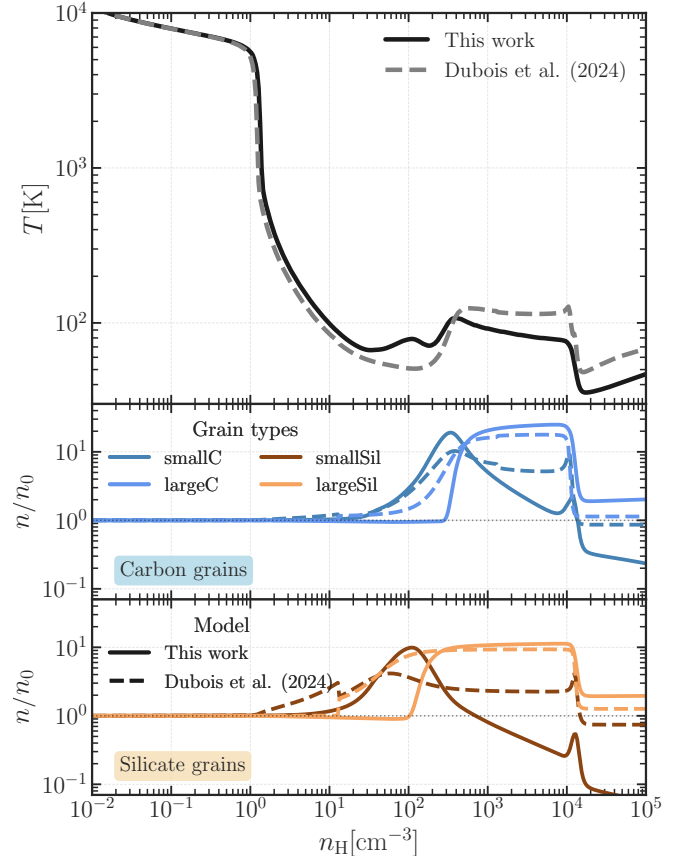


FIG. 20.—: Equilibrium temperature test for

(2017) which assumes that 0.5 of the gas mass-with unresolved Jeans length and with gas density above 0.1 cm^{-3} and temperature below 10^4 K-is at a density of 10^3 cm^{-3} . The small grain turbulent velocity is fixed at 0.1 km s^{-1} .

- Shattering is based on the scaling with n_H from Granato et al. (2021) that is equivalent to having a dispersion velocity varying from 10 km s^{-1} to 1 km s^{-1} from the WIM (1 H cm^{-3}) to the molecular cloud phase (10^3 H cm^{-3}).

In Dubois et al. 2024 PAHs are not modelled as a separate component, and grains are divided only into two sizes (5 nm and $0.1 \mu\text{m}$) and compositions (carbonaceous and silicates). We also note that in their model thermal sputtering follows the fitting curves from Hu et al. (2019) to the thermal sputtering yields obtained by Nozawa et al. (2006), but this is irrelevant for the temperature range of the equilibrium test.

Fig. 20 shows the comparison of CALIMA (solid lines) and the dust parameters of Dubois et al. (2024) (dashed lines) for the equilibrium temperature (top panel), smallC and largeC number densities (middle panel), and smallSil and largeSil number densities (bottom panel). The number densities are normalised by their values in the initial conditions (see Section 4.1 for more details on the initial dust abundances), in order to better capture the variations due to dust processes at a given n_H . By firstly examining the number densities of the different grain bins, it can easily be appreciated that shattering

Model feature	1st time?	Remarks
Seeding by stellar processes	✗	Injection of dust grains by SN and winds is implemented in many live dust models for galaxy formation (e.g. Aoyama et al. 2017; Hou et al. 2017; McKinnon et al. 2018; Granato et al. 2021; Parente et al. 2022; Choban et al. 2022; Dubois et al. 2024; Trayford et al. 2025).
Grain charging	✓	Grain charging directly connect to the local grain and ISM properties is present in photodissociation codes (e.g. Le Petit et al. 2006; van Hoof et al. 2004; Ercolano et al. 2008), but never in an ISM model nor on galaxy evolution.
Dust PEH	*	PEH is usually included in ISM models using size, and ISRF-averaged efficiencies (e.g. Bialy & Sternberg 2019; Kim et al. 2023; Katz et al. 2022), and with no self-consistent dependence on evolving dust properties.
Accretion	*	Gas-phase accretion is a fundamental component of many dust evolution models, but it has never been connected to individual ion abundances and direct grain charging within a non-equilibrium chemistry model.
Dust thermal sputtering	*	Grain-size and Coulomb effects have only been considered in post-processing tools for SN (Kirchschlager et al. 2019), but never for dust model within a galaxy formation simulation.
Dust collisional cooling	*	Implementations for low temperature cooling in clouds (Hollenbach & Mckee 1979) and high temperature, ionised gas (Dwek & Werner 1981) are present in different forms, but never considering the finite size of grains, their chemical properties, and the evolution of their size, composition and charge.
Dust non-thermal sputtering	✗	Destruction of grains for shocked gas is present in many dust evolution models.
Turbulent shattering and coagulation	*	Turbulent-induced collisions of dust grains is usually included using fixed velocity dispersions (e.g. Dubois et al. 2024), or with a scaling based on the local Jeans length (e.g. Li et al. 2021; Narayanan et al. 2023), but without direct measurement of the local turbulent properties as done in this work.
H ₂ formation on grains	*	While dust live models sometimes include the local dust mass to obtain H ₂ formation rates, they do not consider variations in efficiency due to the change in grain size, composition and temperature.
Dust and PAHs interaction with radiative transfer	*	Live dust models either only consider the local dust mass (Kannan et al. 2020), or directly do not include on-the-fly radiation transfer.
Stellar PAH seeding	✓	Direct injection of PAHs either by carbonaceous grain fragmentation in SN shocks or via C-rich AGB winds has not been included in previous galaxy formation simulations with PAHs (Narayanan et al. 2023).
PAH growth	*	PAH growth has been treated as to proceed in the same way as dust grains (Narayanan et al. 2023), without consideration of their molecular nature.
PAH thermal sputtering	✓	Never included in galaxy or ISM formation models.
PAH clustering	✓	Never included in galaxy or ISM formation models.
PAH evaporation	✓	Never included in galaxy or ISM formation models.
PAH freezing	✓	Never included in galaxy or ISM formation models.
PAH photo-dissociation	✓	Never included in galaxy or ISM formation models.
H ₂ formation on PAHs	✓	Never included in galaxy or ISM formation models.

TABLE 3: Summary of the dust and PAH processes included in CALIMA and their novelty in the current context of galaxy formation modelling. For each model feature, we indicate whether it is the first time is implemented in a galaxy formation/ISM model (✓), if it has been implemented to some extent but CALIMA introduces a more self-consistent and updated modelling (*), and if it was implemented before in other numerical implementations of live dust modelling (✗).

and coagulation start to have an effect on the grain size distribution at $n_{\text{H}} \sim 1 \text{ cm}^{-3}$ and $n_{\text{H}} \sim 10 \text{ cm}^{-3}$, respectively. These transitions occur at larger n_{H} and reaching higher values of small and large grains, in shattering- and coagulation-dominated regions, respectively. Therefore, we expect CALIMA to result in larger contrasts in the STL across phases than the Dubois et al. (2024) predicts. We also note that due to the fixed velocity dispersion used in the coagulation model of Aoyama et al. (2017), we predict significantly faster depletion of small grains for $n_{\text{H}} \gtrsim 10^2 \text{ cm}^{-3}$. These changes in the STL across density are also imprinted in the equilibrium temperature curve (top panel of Fig. 20). Since CALIMA predicts a higher (lower) abundance of small grains for $n_{\text{H}} \sim 10^2 \text{ cm}^{-3}$ ($n_{\text{H}} \gtrsim 3 \times 10^2 \text{ cm}^{-3}$), the temperature is higher (lower) than using the dust parameters in Dubois et al. (2024). This is caused by higher elemental addition (hence decreased metal line cooling) and higher H_2 production (therefore more H_2 heating) when there is a larger abundance of small grains. Overall, Dubois et al. (2024) tends to predict a larger fraction of small grains in the cold and molecular phases of the ISM, resulting in increased equilibrium temperatures compared to CALIMA.

5.2. Limitations of our modelling

Despite the proven practical utility of the two-size approximation modelling by Hirashita (2015), it possesses inherited issues of any model with a discretised GSD. While optical properties are computed as effective, locally averaged quantities obtained by weighting over the underlying GSD (see Section 2.11), many dust evolution processes (accretion, destruction, charging, etc.) are evaluated at the central grain size of each bin to limit the computational expense. As a result, the choice and resolution of the size discretisation can influence the inferred evolution timescales and relative importance of competing processes (e.g. see the comparison of CALIMA with Dubois et al. 2024 in Section 5.1). The immediate solution to such a problem is to increase the number of size bins (e.g. McKinnon et al. 2018; Aoyama et al. 2019; Li et al. 2021), but this imposes a significant increase in the memory imprint (the GSD is evolved for every cell in the simulation) and in the computational cost of CALIMA (shattering and coagulation operations increase like N_{bins}^2 in Smoluchowski-type equations). To maintain the minimal computational expense of running simulations with CALIMA, we propose instead to use the moment of methods adapted to dust processing (e.g. Mattsson 2016; Mattsson et al. 2020).

An assumption used in many models of dust evolution for galaxy formation is the dynamical coupling of dust grains with the gas flow (e.g. Zhukovska et al. 2016; Aoyama et al. 2017; Gjergo et al. 2018; Romano et al. 2022b; Choban et al. 2022; Dubois et al. 2024). Dust-gas coupling is governed by the ratio of the aerodynamic stopping time to the local gas flow timescale (see Appendix A.3 and Draine & Salpeter 1979). While grains of all sizes remain tightly coupled to the gas in dense and turbulent phases of the interstellar medium, large grains ($a \gtrsim 0.1 \mu\text{m}$) are expected to become marginally coupled or decoupled in hot, low-density environments and galactic outflows, where their stopping lengths can reach tens to hundreds of parsecs (e.g. Hopkins & Lee 2016;

Commerçon et al. 2023). In such regimes, the assumption of perfect dust-gas coupling may lead to inaccuracies in the predicted dust distribution and its interaction with the radiation field. An additional source of uncertainty in dust dynamics arises from the influence of magnetic fields and magnetohydrodynamic (MHD) turbulence. Charged dust grains interact with magnetic fields through Lorentz forces, which can significantly modify both their acceleration and drag, particularly in diffuse and ionised phases of the ISM where grain charging is efficient (see Section 4.2.2). In turbulent MHD flows, dust grains may experience gyro-motion, resonant interactions with Alfvénic fluctuations, and size-dependent acceleration, leading to preferential transport and spatial segregation relative to the gas (e.g., Yan et al. 2004; Moseley et al. 2022; Moseley & Teyssier 2025). These effects can alter effective drag timescales and enhance grain decoupling beyond what is expected from purely hydrodynamic considerations. Incorporating MHD-dependent dust forces and turbulence-driven acceleration represents an important avenue for future improvements.

A limitation of the present model is the appearance of an excess contribution of smallPAHs in regions characterised by high radiation field intensity G_0 and relatively low gas temperatures (i.e. Fig. 13 in Section 4.2.2). In such environments, the balance between smallPAH destruction and formation may not be fully captured in the current treatment. While top-down formation pathways—whereby largePAHs fragment into smallPAHs under energetic processing—are expected to operate in strongly irradiated regions (e.g. Maragkoudakis et al. 2026), observational predictions suggest that sufficiently intense radiation fields should still favour the survival and dominance of largePAHs due to their higher photostability (e.g. Knight et al. 2021; Chown et al. 2024; Baron et al. 2025). Based on the modelling in Sections 3.7 and 3.9 we have computed the ratio of largePAH evaporation to smallPAH dissociation timescales. Given that smallPAHs quickly become fully dehydrogenated at high G_0 and that the fitting to the results of Montillaud & Joblin (2014) is independent of n_{H} , we find that evaporation becomes faster than dissociation for $G_0 \gtrsim 10^2$, no matter the local gas density. Given that in these conditions PAH growth via accretion is negligible, an overabundance of smallPAHs points at the faster timescale of evaporation compared to dissociation at high G_0 . This may suggest that either our modelling of smallPAH dissociation predicts an incorrect dependence on G_0 or the simple scaling of evaporation time taken from Montillaud & Joblin (2014) predicts an incorrect resilience of largePAHs in intense radiation fields. Another possibility is that our description of largePAHs as PAH clusters formed from smallPAHs like circumcoronene is an incomplete approach to the evolution of PAH sizes in the ISM (e.g. Rapacioli et al. 2005), and instead PAHs grow by extending their planar structure instead of by stacking monomers (Roser & Ricca 2015). In future iterations of CALIMA we will explore direct modelling of PAH evaporation, hydrogenation, etc., instead of relying in the current fitting functions.

Closely related to the problem discussed above, PAH aromatisation is an unexplored component in the current version of the model. In CALIMA we track the hydrogenation

tion state of PAHs using parametrised prescriptions based on the results of Andrews et al. (2016) and Montillaud et al. (2013), allowing us to follow the number of hydrogen atoms attached to the carbon skeleton as function of local physical conditions. In this work, the hydrogenation state of PAHs is used as a *proxy* for the degree of UV processing and edge saturation. While changes in hydrogenation correlate with aromatisation and aliphatisation, the latter involve structural rearrangements (e.g. Jones et al. 2013; Murga et al. 2016) of the carbon skeleton that are not explicitly modelled (i.e. dominance of sp^3 electron orbital hybridisation compared to sp^2 in aromatic carbon structures). Aromatisation is expected to occur rapidly in strong radiation fields ($G_0 \gtrsim 10$ for PAHs larger than $\sim 50C$, Murga et al. 2019), whereas it can be significantly slower in shielded regions of the ISM. Moreover, the adapted hydrogenation modelling relies on empirical fits in G_0 – n_H space and lacks the same level of physical self-consistency as other components of the PAH photo-chemical modelling. Planned improvements to CALIMA include introducing a more complete treatment of aromatic fraction as an independent state variable, allowing for non-equilibrium evolution of both hydrogenation and aromatisation, and for these to be treated as related but distinct processes.

6. CONCLUSIONS

CALIMA provides a unified and self-consistent framework for evolving interstellar dust grains and PAHs on-the-fly in radiation-hydrodynamics simulations, embedding them as thermodynamically and radiatively active components of the multiphase ISM rather than passive tracers. It is built around a two-size (small/large), two-composition (amorphous carbonaceous/silicate) description of dust plus a dedicated PAH component (small and large clusters), so that variations in dust-to-metal ratio, small-to-large grain ratio, and PAH fraction emerge self-consistently from stellar seeding and ISM processing instead of being imposed through fixed scalings. Within this framework, the same evolving grain and PAH populations set opacities, photoelectric heating and grain-assisted recombination efficiencies, collisional gas–dust energy exchange, and H_2 formation rates, all computed in concert with on-the-fly radiative transfer and non-equilibrium thermo-chemistry.

We have revisited and extended a broad set of microphysical processes for both dust and PAHs in a way that is tailored to galaxy-scale simulations but retains close contact with the underlying laboratory and theoretical constraints. For bulk dust, we implement stellar dust injection from SNe and AGB stars; accretion of gas-phase metals that is explicitly modulated by a turbulence-informed sub-grid density PDF and by grain charging; shattering and coagulation driven by turbulent grain relative velocities; non-thermal destruction in supernova shocks; and updated thermal sputtering that accounts for finite grain size and modern ion–solid interaction physics. For PAHs, we include formation and seeding, clustering into larger aggregates, freezing onto regular grains, photo-dissociation and evaporation of clusters, thermal and non-thermal sputtering, and a detailed treatment of charge and hydrogenation balance that feeds into both photoelectric heating and H_2 formation. These ingredients are consistently mapped into

wavelength-dependent opacities and heating/cooling efficiencies, ensuring that radiation, thermochemistry, and grain/PAH physics evolve in synergy.

We have used equilibrium temperature–density tests to examine how dust–PAH evolution significantly modifies the canonical thermal and chemical structure of the ISM even at fixed metallicity. We highlight:

- Gas-phase metal accretion, especially onto small carbonaceous grains, produces strong, density-dependent depletions in C and O that suppress C II and O I cooling above $n_H \sim 10 \text{ cm}^{-3}$, shifting equilibrium temperatures upward in the unstable and cold neutral medium compared with fixed-dust models.
- The competition between accretion, coagulation, and shattering reshapes the small-to-large grain ratio across density, altering the surface-to-mass ratio and therefore H_2 formation and heating, with coagulation at high densities depleting small grains and shattering at intermediate densities partially replenishing them.
- PAH evolution (clustering, freezing, sputtering) rapidly depletes small PAHs in dense gas, transferring PAH carbon into clusters and grains, which in turn quenches PAH-driven photoelectric heating in the cold and molecular phases, while leaving PAHs far more abundant and radiatively active in diffuse and moderately dense gas.
- Direct computation of grain and PAH photoelectric efficiencies shows that MRN-averaged, fixed-efficiency recipes misestimate both the normalisation and density dependence of the heating rate, particularly once dust growth enhances small-grain mass and PAH depletion suppresses PAH abundance at higher densities.

Using isolated dwarf galaxy formations at various initial metallicities, we have explored how the same physics generates a rich, environment-dependent dust and PAH phenomenology and leaves a clear imprint on the thermodynamic and molecular structure of the ISM. The main results can be summarised as:

- The dust-to-metal ratio, small-to-large grain mass ratio, PAH fraction, and local radiation field strength develop strong variations across gas phases, with enhanced small-grain and PAH abundances closely tracing the bulk of the cold and thermally unstable gas, reduced DTM and small grain mass fraction in the hot phase, and destruction of PAHs in hot and highly irradiated phases.
- These spatial variations lead to warmer unstable and cold phases around $n_H \sim 10^2 \text{ cm}^{-3}$, a broader spread of equilibrium temperatures at intermediate densities, and a higher H_2 fraction at high densities than in fixed-dust runs, even though H_2 is suppressed at $n_H \lesssim 10 \text{ cm}^{-3}$ where dust growth and shielding are weaker. This is particularly interesting in the context commonly adopted H_2 formation efficiencies in chemistry models for the ISM.

- Line-of-sight column-density statistics show improved agreement with observed CO at high N_{H_2} and with C I/C II in diffuse gas when dust and PAHs are evolved.
- The emergent, highly structured distribution of dust and PAHs produces non-trivial spatial variations in extinction, UV transparency, and photoelectric heating efficiency, indicating that simple, globally scaled dust prescriptions struggle to capture the coupling between radiation, ISM phases, and molecular chemistry in galaxy discs.

Taken together, these developments show that allowing dust and PAHs to evolve and to feed back on radiation and thermochemistry is not a minor refinement but a necessary step towards realistic ISM and galaxy formation modelling. CALIMA is a major step in elevating dust and PAHs from static opacity and heating parameters to dynamically evolving agents that shape thermal stability, phase structure, and molecule formation, generating environment-dependent dust and PAH observables naturally from the underlying gas dynamics and radiation field. This establishes a pathway to interpret the rapidly growing body of dust- and PAH-sensitive observations—from C II and CO to mid-IR PAH bands and attenuation curves—in a framework where the microphysics of grain

evolution and the macroscopic evolution of galaxies and their ISM are treated as a single, self-consistent problem.

ACKNOWLEDGEMENTS

FRM thanks Dimitra Rigopoulou, Ismael García-Bernete, Fergus Donnan, Nathalie Ysard, Laurent Verstraete, Bruce T. Draine, Brandon S. Hensley, Ugo Lebreuilly, Patrick Hennebelle and Gabriel Verrier for helpful discussions. Simulation analysis made use of the Infinity Cluster hosted by Institut d’Astrophysique de Paris. We thank Stephane Rouberol for running it smoothly. The simulations included here made extensive use of the dp016 project on the DiRAC ecosystem. This work was performed using the DiRAC Data Intensive service at Leicester, operated by the University of Leicester IT Services, which forms part of the STFC DiRAC HPC Facility (www.dirac.ac.uk). The equipment was funded by BEIS capital funding via STFC capital grants ST/K000373/1 and ST/R002363/1 and STFC DiRAC Operations grant ST/R001014/1.

This project made use of the following packages: CMASHER ([van der Velden 2020](#)), MATPLOTLIB ([Hunter 2007](#)), NUMPY ([Harris et al. 2020](#)), and SCIPY ([Virtanen et al. 2020](#)). The authors acknowledge the use of OpenAI’s ChatGPT for assistance with code refactoring, and simulation analysis. The scientific analysis and results were independently verified by the authors.

REFERENCES

- Abel T., Bryan G. L., Norman M. L., 2000, *ApJ*, 540, 39
 Abel T., Bryan G. L., Norman M. L., 2002, *Sci*, 295, 93
 Abouelaziz H., et al., 1993, *JChPh*, 99, 237
 Agertz O., et al., 2021, *MNRAS*, 503, 5826
 Agundez M., Cabezas C., Marcelino N., Tercero B., Fuentetaja R., de Vicente P., Cernicharo J., 2025, *A&A*, 697, A82
 Allain T., Leach S., Sedlmayr E., 1996, *A&A*, 305, 602
 Allamandola J. L., Sandford A. S., Valero J. G., 1988, *Icar*, 76, 225
 Allamandola L. J., Tielens A. G. G. M., Barker J. R., Allamandola L. J., Tielens A. G. G. M., Barker J. R., 1989, *ApJS*, 71, 733
 Allers K. N., Jaffe D. T., Lacy J. H., Draine B. T., Richter M. J., 2005, *ApJ*, 630, 368
 Altarawneh M., Ali L., 2024, *Energy and Fuels*, 38, 21735
 Andersen H. H., Bay H. L., 1981, in Behrisch R., ed., , Vol. 47, Sputtering by Particle Bombardment I: Physical Sputtering of Single-Element Solids. Springer-Verlag, p. 145, [doi:10.1007/3540105212_9](https://doi.org/10.1007/3540105212_9)
 Andrews B. H., Martini P., 2013, *ApJ*, 765, 140
 Andrews H., Candian A., Tielens A. G. G. M., 2016, *A&A*, 595, A23
 Aoyama S., Hou K. C., Shimizu I., Hirashita H., Todoroki K., Choi J. H., Nagamine K., 2017, *MNRAS*, 466, 105
 Aoyama S., Hou K. C., Hirashita H., Nagamine K., Shimizu I., 2018, *MNRAS*, 478, 4905
 Aoyama S., et al., 2019, *MNRAS*, 484, 1852
 Aoyama S., Hirashita H., Nagamine K., 2020, *MNRAS: Letters*, 491, 3844
 Asano R. S., Takeuchi T. T., Hirashita H., Nozawa T., 2013, *MNRAS*, 432, 637
 Asano R. S., Takeuchi T. T., Hirashita H., Nozawa T., 2014, *MNRAS*, 440, 134
 Ashley J. C., Anderson V. E., 1981, *IEEE TranNucSci*, 28, 4131
 Asplund M., Grevesse N., Sauval A. J., Scott P., 2009, *ARA&A*, 47, 481
 Baes M., Camps P., Matsumoto K., 2022, *A&A*, 666, A101
 Bakes E. L. O., Tielens A. G. G. M., Bakes E. L. O., Tielens A. G. G. M., 1994, *ApJ*, 427, 822
 Bakes E. L. O., Tielens A. G. G. M., Bauschlicher Charles W. J., 2001, *ApJ*, 556, 501
 Balashev S. A., Kosenko D. N., Noterdaeme P., 2025, *A&A*, 696, L16
 Barlow M. J., Barlow J. M., 1978, *MNRAS*, 183, 367
 Baron D., et al., 2025, *ApJ*, 978, 135
 Barrera N. F., Fuentealba P., Muñoz F., Gómez T., Cárdenas C., 2023, *MNRAS*, 524, 3741
 Bauschlicher C. W., Bakes E. L. O., Bauschlicher C. W., Bakes E. L. O., 2001, *CP*, 274, 11
 Bauschlicher Jr. C. W., Peeters E., Allamandola L. J., 2008, *ApJ*, 678, 316
 Bekki K., 2013, *MNRAS*, 432, 2298
 Bendo G. J., et al., 2010, *A&A*, 518, 65
 Berné O., Tielens A. G. G. M., 2011, *PNAS*, 109, 401
 Berné O., Foschino S., Jalabert F., Joblin C., 2022, *A&A*, 667, A159
 Bethe H., Bethe H. 1930, *AnP*, 397, 325
 Bialy S., Sternberg A., 2019, *ApJ*, 881, 160
 Biener L., et al., 2005, *IAUS*, 231, 217
 Blair W. P., Davidson K., Fesen R. A., Uomoto A., MacAlpine G. M., Henry R. B. C., 1997, *ApJ Supplement Series*, 109, 473
 Bloch F., Bloch F. 1933, *AnP*, 408, 285
 Bocchio M., Micelotta E. R., Gautier A. L., Jones A. P., Bocchio M., Micelotta E. R., Gautier A. L., Jones A. P., 2012, *A&A*, 545, A124
 Bocchio M., Jones A. P., Slavin J. D., 2014, *A&A*, 570, A32
 Bohdanský J., 1984, *Nuclear Instruments and Methods in Physics Research B*, 2, 587
 Bohdanský J., Roth J., Bay H. L., Bohdanský J., Roth J., Bay H. L., 1980, *JAP*, 51, 2861
 Bolatto A. D., Wolfire M., Leroy A. K., 2013, *ARA&A*, 51, 207
 Bolatto A. D., et al., 2024, *ApJ*, 967, 63
 Boschman L., Reitsma G., Cazaux S., Schlathöler T., Hoekstra R., Spaans M., González-Magaña O., 2012, *ApJL*, 761, L33
 Boschman L., Cazaux S., Spaans M., Hoekstra R., Schlathöler T., 2015, *A&A*, 579, A72
 Boulanger F., Boissel P., Cesarsky D., Ryter C. 1998, *A&A*
 Boutéraon T., Habart E., Ysard N., Jones A. P., Dartois E., Pino T., 2019, *A&A*, 623, A135
 Brandt T. D., Draine B. T., 2011, *ApJ*, 744, 129
 Bréchnignac P., et al., 2014, *JChPh*, 141, 164325
 Bron E., Le Bourlot J., Le Petit F., 2014, *A&A*, 569, A100

- Burke J. R., Hollenbach D. J., 1983, *ApJ*, 265, 223
- Burke J. R., Silk J., Burke J. R., Silk J., 1974, *ApJ*, 190, 1
- Burkhardt A. M., et al., 2021, *ApJL*, 913, L18
- Byun G.-H., et al., 2025, *ApJ*, 992, 92
- Cabezas C., et al., 2025, *A&A*, 701, L8
- Calura F., Pipino A., Matteucci F., 2007, *A&A*, 479, 669
- Calzetti D., et al., 2007, *ApJ*, 666, 870
- Camps P., Baes M., 2015, *Astron. Comput.*, 9, 20
- Canosa A., et al., 1994, *CPL*, 228, 26
- Canosa A., Laubé S., Rebrion C., Pasquero D., Gomet J. C., Rowe B. R., 1995, *Chem. Phys. Lett.*, Volume 245, Issue 4, p. 407-414., 245, 407
- Cardelli J. A., Clayton G. C., Mathis J. S., Cardelli J. A., Clayton G. C., Mathis J. S., 1989, *ApJ*, 345, 245
- Carelli F., Grassi T., Gianturco F. A., 2013, *A&A*, 549, A103
- Castellanos P., Candian A., Zhen J., Linnartz H., Tielens A. G., 2018a, *A&A*, 616, A166
- Castellanos P., Candian A., Andrews H., Tielens A. G. G. M., 2018b, *A&A*, 616, A167
- Cau P., 2002, *A&A*, 392, 203
- Cazaux S., Tielens A. G. G. M., 2002, *ApJ*, 575, L29
- Cazaux S., Tielens A. G. G. M., 2004, *ApJ*, 604, 222
- Cazaux S., Tielens A. G. G. M., Cazaux S., Tielens A. G. G. M., 2004, *ApJ*, 604, 222
- Cernicharo J., Agúndez M., Cabezas C., Tercero B., Marcelino N., Pardo J. R., De Vicente P., 2021a, *A&A*, 649, 15
- Cernicharo J., Agúndez M., Kaiser R. I., Cabezas C., Tercero B., Marcelino N., Pardo J. R., De Vicente P., 2021b, *A&A*, 655, 1
- Cernicharo J., et al., 2022, *A&A*, 663, L9
- Chaabouni H., Bergeron H., Baouche S., Dulieu F., Matar E., Congiu E., Gavilan L., Lemaire J. L., 2012, *A&A*, 538, A128
- Chastenot J., et al., 2023, *ApJL*, 944, L11
- Chen L.-F., Li D., Quan D., Zhang X., Chang Q., Li X., Xiao L., 2022, *ApJ*, 928, 175
- Cherchneff I., Barker J. R., Tielens A. G. G. M., Cherchneff I., Barker J. R., Tielens A. G. G. M., 1992, *ApJ*, 401, 269
- Chiar J. E., Tielens A. G. G. M., 2005, *ApJ*, 637, 774
- Choban C. R., Kereš D., Hopkins P. F., Sandstrom K. M., Hayward C. C., Faucher-Giguère C.-A., 2022, *MNRAS*, 514, 4506
- Choban C. R., Kereš D., Sandstrom K. M., Hopkins P. F., Hayward C. C., Faucher-Giguère C. A., 2024, *MNRAS*, 529, 2356
- Chokshi A., Tielens A. G. G. M., Hollenbach D., Chokshi A., Tielens A. G. G. M., Hollenbach D., 1993, *ApJ*, 407, 806
- Chown R., et al., 2024, *A&A*, 685, A75
- Colman T., et al., 2024, *A&A*, 686, A155
- Commerçon B., Lebrouilly U., Price D. J., Lovascio F., Laibe G., Hennebelle P., 2023, *A&A*, 671, A128
- Compiègne M., et al., 2010, *A&A*, 525, A103
- Cosslett V. E., 1978, *J. Microsc.*, 113, 113
- Costantini E., Predehl P., Costantini E., Predehl P., 2001, *tysc*, p. 34
- Crenny T., Federman S. R., 2003, *ApJ*, 605, 278
- Cuppen H. M., Herbst E., 2007, *ApJ*, 668, 294
- D'Hendecourt L. B., Leger A., D'Hendecourt L. B., Leger A., 1987, *A&A*, 180, L9
- Dalgarno A., McCray R. A., Dalgarno A., McCray R. A., 1972, *ARA&A*, 10, 375
- De Cia A., Ledoux C., Mattsson L., Petitjean P., Srianand R., Gavignaud I., Jenkins E. B., 2016, *A&A*, 596
- De Vis P., et al., 2017, *MNRAS*, 464, 4680
- De Vis P., et al., 2019, *A&A*, 623, A5
- Dopcke G., Glover S. C., Clark P. C., Klessen R. S., 2011, *ApJL*, 729, L3
- Dopita M. A., Sutherland R. S., Dopita M. A., Sutherland R. S., 2000, *ApJ*, 539, 742
- Dorschner J., Henning T., 1995, *A&ARv*, 6, 271
- Dorschner J., Dorschner J. 1982, *Ap&SS*, 81, 323
- Draine B. T., 1978, *ApJ*, 36, 595
- Draine B., 2003a, *ARA&A*, 41, 241
- Draine B. T., 2003b, *ApJ*, 598, 1017
- Draine B. T., 2011, *Physics of the Interstellar and Intergalactic Medium*. Princeton University Press, doi:10.2307/j.ctvc4m4hzzr, <http://www.jstor.org/stable/10.2307/j.ctvc4m4hzzr>
- Draine B. T., Li A., 2001, *ApJ*, 551, 807
- Draine B. T., Li A., 2007, *ApJ*, 657, 810
- Draine B. T., Salpeter E. E., 1979, *ApJ*, 231, 77
- Draine B. T., Sutin B., 1987, *ApJ*, 320, 803
- Draine B. T., Tan J. C., 2003, *ApJ*, 594, 347
- Draine B. T., Salpeter E. E., Draine B. T., Salpeter E. E., 1979, *ApJ*, 231, 438
- Draine B. T., Lee H. M., Draine B. T., Lee H. M., 1984, *ApJ*, 285, 89
- Draine B. T., et al., 2007, *ApJ*, 663, 866
- Draine B. T., Li A., Hensley B. S., Hunt L. K., Sandstrom K., Smith J.-D. T., 2021, *ApJ*, 917, 3
- Dubois Y., et al., 2024, *A&A*, 687, A240
- Dwek E., 1998, *ApJ*, 501, 643
- Dwek E., Werner M. W., 1981, *ApJ*, 248, 138
- Egorov O. V., et al., 2023, *ApJ*, 944, L16
- Egorov O. V., et al., 2025, *A&A*, 703, A103
- Elmegreen B. G., Scalo J., 2004, *ARA&A*, 42, 211
- Elyajouri M., et al., 2024, *A&A*, 685, A76
- Engelbracht C. W., Gordon K. D., Rieke G. H., Werner M. W., Dale D. A., Latter W. B., 2005, *ApJ*, 628, L29
- Ercolano B., Young P. R., Drake J. J., Raymond J. C., 2008, *ApJS*, 175, 534
- Falgarone E., et al., 2017, *Nature*, 548, 430
- Federman S. R., Huntress W. T. J., Prasad S. S., Federman S. R., Huntress W. T. J., Prasad S. S., 1990, *ApJ*, 354, 504
- Federrath C., Banerjee S., 2015, *MNRAS*, 448, 3297
- Federrath C., Klessen R. S., 2012, *ApJ*, 763, 51
- Ferland G. J., et al., 2017, *RMxAA*, 53, 385
- Ferrara A., 2024, *A&A*, 689, A310
- Ferrara A., Pallottini A., Dayal P., 2022, *MNRAS*, 522, 3986
- Fitzpatrick E. L., 1999, *PASP*, 111, 63
- Foster J. B., Mandel K. S., Pineda J. E., Covey K. R., Arce H. G., Goodman A. A., 2013, *MNRAS*, 428, 1606
- Fraser H. J., McCoustra M. R., Williams D. A., 2002, *A&G*, 43, 10
- Frenklach M., 2002, *PCCP*, 4, 2028
- Frenklach Michael Feigelson D. E., 1989, *ApJ*, 341, 372
- Fromang S., Nelson R. P., 2009, *A&A*, 496, 597
- Galamez M., et al., 2016, *MNRAS*, 456, 1767
- Galliano F., Dwek E., Chaniel P., 2008a, *ApJ*, 672, 214
- Galliano F., Madden S. C., Tielens A. G. G. M., Peeters E., Jones A. P., 2008b, *ApJ*, 679, 310
- Geen S., Rosdahl J., Blaizot J., Devriendt J., Slyz A., 2015, *MNRAS*, 448, 3248
- Genzel R., et al., 1997, *ApJ*, 498, 579
- Gerin M., et al., 2015, *A&A*, 573, A30
- Gjergo E., Granato G. L., Murante G., Ragone-Figueroa C., Tornatore L., Borgani S., 2018, *MNRAS*, 479, 2588
- Glatzle M., Graziani L., Ciardi B., 2022, *MNRAS*, 510, 1068
- Glover S. C., Clark P. C., 2012, *MNRAS*, 421, 9
- Glover S. C. O., Jappsen A., 2007, *ApJ*, 666, 1
- Glover S. C. O., Mac Low M., 2007, *ApJS*, 169, 239
- Glover S. C., Federrath C., Low M. M., Klessen R. S., 2010, *MNRAS*, 404, 2
- Gnedin N. Y., Tassis K., Kravtsov A. V., 2009, *ApJ*, 697, 55
- Goicoechea J. R., et al., 2025, *A&A*, 696, A100
- Gomez H. L., et al., 2012, *MNRAS*, 420, 3557
- Gong M., Ostriker E. C., Wolfire M. G., 2019, *ApJ*, 843, 38
- Goumans T. P. M., Goumans M. T. P., 2011, *MNRAS*, 415, 3129
- Graham J. R., et al., 1987, *ApJ*, 319, 126
- Granato G. L., et al., 2021, *MNRAS*, 503, 511
- Grassi T., Bovino S., Schleicher D. R., Prieto J., Seifried D., Simoncini E., Gianturco F. A., 2014, *MNRAS*, 439, 2386
- Guhathakurta P., Draine B. T., Guhathakurta P., Draine B. T., 1989, *ApJ*, 345, 230
- Guillet V., Hennebelle P., Pineau des Forêts G., Marcowith A., Commerçon B., Marchand P., 2020, *A&A*, 643, A17
- Haardt F., Madau P., 2012, *ApJ*, 746, 125
- Habart E., et al., 2003a, *A&A*, 397, 623
- Habart E., Boulanger F., Verstraete L., Walmsley C. M., Forets G. P. d., 2003b, *A&A*, 414, 531
- Habing H. J., 1968, *BAIN*, 19, 421
- Hadjar O., Hoekstra R., Morgenstern R., Schlathölter T., Hadjar O., Hoekstra R., Morgenstern R., Schlathölter T., 2001, *PhRvA*, 63, 033201
- Harris C. R., et al., 2020, *Nat.*, 585, 357
- Hellyer B., 1970, *MNRAS*, Vol. 148, p. 383 (1970), 148, 383
- Helou et al., 2001, *ApJL*, 548, L73

- Hennebelle P., Falgarone E., 2012, *A&A Review*, 20, 55
- Hennebelle P., Bruy N., Colman T., Hennebelle P., Bruy N., Colman T., 2024, *arXiv*, p. arXiv:2404.17368
- Henning T., Henning Thomas 2010, *ARA&A*, 48, 21
- Hensley B. S., Draine B. T., 2021, *ApJ*, 906, 73
- Hirashita H., 2015, *MNRAS*, 447, 2937
- Hirashita H., Aoyama S., 2019, *MNRAS*, 482, 2555
- Hirashita H., Kuo T. M., 2011, *MNRAS*, 416, 1340
- Hirashita H., Li Z. Y., 2013, *MNRAS: Letters*, 434, L70
- Hirashita H., Murga M. S., 2020, *MNRAS*, 492, 3779
- Hirashita H., Yan H., 2009, *MNRAS*, 394, 1061
- Hollenbach D., Mckee C. F., 1979, *ApJ Supplement Series*, 41, 555
- Hollenbach D., Mckee C. F., 1989, *ApJ*, 342, 306
- Hollenbach D., Kaufman M. J., Bergin E. A., Melnick G. J., 2008, *ApJ*, 690, 1497
- Hopkins P. F., 2013, *MNRAS*, 430, 1880
- Hopkins P. F., Lee H., 2016, *MNRAS*, 456, 4174
- Hopkins P. F., Kereš D., Oñorbe J., Faucher-Giguère C. A., Quataert E., Murray N., Bullock J. S., 2014, *MNRAS*, 445, 581
- Hou K. C., Hirashita H., Nagamine K., Aoyama S., Shimizu I., 2017, *MNRAS*, 469, 870
- Hou K. C., Aoyama S., Hirashita H., Nagamine K., Shimizu I., 2019, *MNRAS*, 485, 1727
- Hu C.-Y., Zhukovska S., Somerville R. S., Naab T., 2019, *MNRAS*, 487, 3252
- Hu C.-Y., Sternberg A., van Dishoeck E. F., 2021, *ApJ*, 920, 44
- Hu C.-Y., Sternberg A., van Dishoeck E. F., 2023, *ApJ*, 952, 140
- Hudgins D. M., Allamandola L. J., Hudgins D. M., Allamandola L. J., 1999, *ApJL*, 513, L69
- Hunter J. D., 2007, *CISE*, 9, 90
- Ibanez-Mejia J. C., Walch S., Ivlev A. V., Clarke S., Caselli P., Joshi P. R., 2019, *MNRAS*, 485, 1220
- Iida S., et al., 2021, *PhRvA*, 104, 043114
- Iskef H., Cunningham J. W., Watt D. E., Iskef H., Cunningham J. W., Watt D. E., 1983, *PMB*, 28, 535
- Jenkins E. B., 2009, *ApJ*, 700, 1299
- Joblin C., Tielens M. A. G. G., Allamandola J. L., Geballe R. T., 1996, *ApJ*, 458, 610
- Jochims H. W., et al., 1994, *ApJ*, 420, 307
- Jochims H. W., Baumgaertel H., Leach S., 1996, *A&A*, 314, 1003
- Jones A. P., Tielens A. G. G. M., Hollenbach D. J., Jones A. P., Tielens A. G. G. M., Hollenbach D. J., 1996, *ApJ*, 469, 740
- Jones A. P., Fanciullo L., Köhler M., Verstraete L., Guillet V., Bocchio M., Ysard N., 2013, *A&A*, 558, A62
- Jones A. P., Ysard N., Köhler M., Fanciullo L., Bocchio M., Micelotta E., Verstraete L., Guillet V., 2014, *Faraday Discussions*, 168, 313
- Jones A. P., Koehler M., Ysard N., Bocchio M., Verstraete L., 2017, *A&A*, 602, A46
- Joy D. C., 1995, *Scanning Microscopy*, 17, 270
- Joy D. C., Luo S., Gauvin R., Hovington P., Evans N., 1996, *Scanning Microscopy*, 10
- Jurac S., Johnson R. E., Donn B., 1998, *ApJ*, 503, 247
- Kannan R., Marinacci F., Vogelsberger M., Sales L. V., Torrey P., Springel V., Hernquist L., 2020, *MNRAS*, 499, 5732
- Katz H., 2022, *MNRAS*, 512, 348
- Katz H., et al., 2022, *arXiv e-prints*, p. arXiv:2211.04626
- Katz et al., 2024, *arXiv*
- Kawasaki Y., Koga S., MacHida M. N., 2022a, *MNRAS*, 515, 2072
- Kawasaki Y., Kawasaki Y., Machida M. N., 2022b, *MNRAS*, 515, 6073
- Kelvin Lee K. L., et al., 2021, *ApJL*, 910, L2
- Kemper F., Friend W. J., Tielens A. G. G. M., 2004, *ApJ*, 609, 826
- Khabazipur A., Eaves N., 2023, *Proc. Combust. Inst.*, 39, 919
- Khan B., et al., 2025, *A&A*, 699, A133
- Khesali A. R., Ghoreyshi S. M., Nejad-Asghar M., 2012, *MNRAS*, 420, 2300
- Kim C.-G., Ostriker E. C., 2017, *ApJ*, 846, 133
- Kim C. G., Ostriker E. C., Kim W. T., 2013, *ApJ*, 776, 1
- Kim J.-G., Gong M., Kim C.-G., Ostriker E. C., 2023, *ApJS*, 264, 10
- Kim J., et al., 2025, *arXiv*, p. arXiv:2511.14833
- Kimm T., Cen R., 2014, *ApJ*, 788, 121
- Kimm T., Katz H., Haehnelt M., Rosdahl J., Devriendt J., Slyz A., 2017, *MNRAS*, 466, stx052
- Kirchschlager F., Schmidt F. D., Barlow M. J., Fogerty E. L., Bevan A., Priestley F. D., 2019, *MNRAS*, 489, 4465
- Kirchschlager F., Barlow M. J., Schmidt F. D., 2020, *ApJ*, 893, 70
- Kirchschlager F., Mattsson L., Gent F. A., 2021, *MNRAS*, 509, 3218
- Klessen R. S., Glover S. C. O., Klessen R. S., Glover S. C. O., 2016, *SAAS*, 43, 85
- Knight C., Peeters E., Stock D. J., Vacca W. D., Tielens A. G. G. M., 2021, *ApJ*, 918, 8
- Kobayashi H., Tanaka H., 2010, *Icarus*, 206, 735
- Kocheril G. S., Zagorec-Marks C., Lewandowski H. J., 2025, *Nat. Astro.*, 9, 685
- Konstantopoulou C., et al., 2022, *A&A*, 666, A12
- Konstantopoulou C., et al., 2024, *A&A*, 681, A64
- Krügel E., 2008, *An Introduction to the Physics of Interstellar Dust. Series in Astronomy and Astrophysics*, Taylor & Francis
- Krumholz M. R., 2014, *Phys. Rep.*, 539, 49
- Krumholz M. R., Dekel A., 2010, *MNRAS*, 406, 112
- Krumholz M. R., Thompson T. A., 2013, *MNRAS*, 434, 2329
- Kunz M. W., Mouschovias T. C., 2010, *MNRAS*, 408, 322
- Lamberts T., de Vries X., Cuppen H. M., 2014, *Faraday Discuss.*, 168, 327
- Lange K., Dominik C., Tielens A. G., 2021, *A&A*, 653, A21
- Lange K., Dominik C., Tielens A. G., 2023, *A&A*, 674, A200
- Langer W. D., Glassgold A. E., Langer W. D., Glassgold A. E., 1976, *A&A*, 48, 395
- Laor A., Draine B. T., 1993, *ApJ*, 402, 441
- Larson R. B., 1981, *MNRAS*, 194, 809
- Lazarian A., Yan H., 2001, *ApJL*, 566, L105
- Le Bourlot J., Le Petit F., Pinto C., Roueff E., Roy F., 2012, *A&A*, 541, A76
- Le Page V., Snow T. P., Bierbaum V. M., Le Page V., Snow T. P., Bierbaum V. M., 2001, *ApJS*, 132, 233
- Le Page V., Snow T. P., Bierbaum V. M., 2009, *ApJ*, 704, 274
- Le Petit F., Le Bourlot J., Roueff E., Nehmé C., 2006, *ApJ Supplement Series, Volume 164, Issue 2*, pp. 506-529., 164, 506
- Lebreuilly U., Commerçon B., Laibe G., 2019, *A&A*, 626, A96
- Lebreuilly U., Vallucci-Goy V., Guillet V., Lombart M., Marchand P., 2022, *MNRAS*, 518, 3326
- Lee H., Hopkins P. F., Squire J., 2017, *MNRAS*, 469, 3532
- Lewis J. S. W., Ocvirk P., Dubois Y., Aubert D., Chardin J., Gillet N., Thélie É., 2022, *MNRAS*, 000, 1
- Li A., Draine B. T., 2001, *ApJ*, 554, 778
- Li A., Greenberg J. M., 2003, in *Pirronello V., Krelowski J., Manicò G., eds, Solid State Astrochemistry*. Springer Netherlands, Dordrecht, pp 37–84
- Li Q., Narayanan D., Davé R., 2019, *MNRAS*, 490, 1425
- Li Q., et al., 2021, *MNRAS*, 507, 548
- Li J., Chen X., Li J., Chen X., 2023, *Univ*, 9, 364
- Limongi M., Chieffi A., 2018, *ApJ Supplement Series*, 237, 13
- Lindhard J., Nielsen V., 1962, *Phys. Lett.*, 2, 209
- Lindhard J., Scharff M., 1961, *Phys. Rev.*, 124, 128
- Lindhard J., Lindhard J. 1964, *Phys. Lett.*, 12, 126
- Ling Y., Lifshitz C., Ling Y., Lifshitz C., 1998, *JMSp*, 33, 25
- Lisenfeld U., Ferrara A., 1998, *ApJ*, 496, 145
- Liu P., Zhang Y., Li Z., Bennett A., Lin H., Sarathy S. M., Roberts W. L., 2019, *Combust. Flame*, 202, 276
- Logan R. M., Keck J. C., Logan R. M., Keck J. C., 1968, *JChPh*, 49, 860
- Loison J.-C., Rossi C., Solem N., Thissen R., Romanzin C., Alcaraz C., Jacovella U., 2025, *eprint arXiv:2506.13290*, p. arXiv:2506.13290
- Loru D., et al., 2023, *A&A*, 677, A166
- Low M. M. M., Klessen R. S., 2004, *Rev. Mod. Phys.*, 76, 125
- Luo S., Zhang X., Joy D. C., 1991, *Radiat. Eff. Defects Solids*, 117, 235
- Madden S. C., Galliano F., Jones A. P., Sauvage M., 2005, *A&A*, 446, 877
- Mallo M., Agúndez M., Cabezas C., Roncero O., Cernicharo J., Molpeceres G., 2025, *A&A*
- Mallocci G., Mulas G., Joblin C., Mallocci G., Mulas G., Joblin C., 2004, *A&A*, 426, 105
- Maragkoudakis A., et al., 2026, *arXiv*, p. arXiv:2601.23282
- Marchand P., Guillet V., Lebreuilly U., Mac Low M. M., 2021, *A&A*, 649, A50
- Marchenko S. V., Moffat A. F., 2017, *MNRAS*, 468, 2416

- Marciniak A., Joblin C., Mulas G., Mundlapati V. R., Bonnamy A., 2021, *A&A*, 652, A42
- Masson J., Chabrier G., Hennebelle P., Vaytet N., Commerçon B., 2015, *A&A*, 587, A32
- Mathis J. S., Rimpl W., Nordsieck K. H., Mathis J. S., Rimpl W., Nordsieck K. H., 1977, *ApJ*, 217, 425
- Mathis J. S., Mezger P. G., Panagia N., 1983, *A&A*, 128, 212
- Matsumoto K., et al., 2024, *A&A*, 689, A79
- Matsunami N., 1980, Technical Report IPPJ-AM-14, Energy dependence of sputtering yields of monatomic solids. Institute of Plasma Physics, Nagoya University, Nagoya, Japan
- Matsuura M., et al., 2014, *MNRAS*, 439, 1472
- Mattsson L., 2016, *Planetary and Space Science*, 133, 107
- Mattsson L., Mattsson Lars 2020, *MNRAS*, 491, 4334
- McCarthy M. C., et al., 2021, *Nature Astronomy*, 5, 176
- McCormick A., Veilleux S., Rupke D. S. N., McCormick A., Veilleux S., Rupke D. S. N., 2013, *ApJ*, 774, 126
- McGuire B. A., Burkhardt A. M., Kalenskii S., Shingledecker C. N., Remijan A. J., Herbst E., McCarthy M. C., 2018, *Science*, 359, 202
- McGuire B. A., et al., 2021, *Science*, 371, 1265
- McKee C. F., Ostriker E. C., 2007, *ARA&A*, 45, 565
- McKee C., McKee C. 1989, *IAUS*, 135, 431
- McKinnon R., Torrey P., Vogelsberger M., 2016, *MNRAS*, 457, 3775
- McKinnon R., Torrey P., Vogelsberger M., Hayward C. C., Marinacci F., 2017, *MNRAS*, 468, 1505
- McKinnon R., Vogelsberger M., Torrey P., Marinacci F., Kannan R., 2018, *MNRAS*, 478, 2851
- Mennella V., Hornekær L., Thrower J., Accolla M., Mennella V., Hornekær L., Thrower J., Accolla M., 2012, *ApJL*, 745, L2
- Micelotta E. R., Jones A. P., Tielens A. G. G. M., 2010a, *A&A*, 510, A37
- Micelotta E. R., Jones A. P., Tielens A. G., 2010b, *A&A*, 510, A36
- Min M., Waters L. B., De Koter A., Hovenier J. W., Keller L. P., Markwick-Kemper F., 2007, *A&A*, 462, 667
- Montet G. L., Montet L. G., 1967, *ApPhL*, 11, 223
- Montillaud J., Joblin C., 2014, *A&A*, 567, A45
- Montillaud J., Joblin C., Toubblanc D., 2013, *A&A*, 552, A15
- Moore T. J., Lumsden S. L., Ridge N. A., Puxley P. J., 2005, *MNRAS*, 359, 589
- Moseley E. R., Teyssier R., 2025, *MNRAS*, 542, 1011
- Moseley E. R., Teyssier R., Draine B. T., 2022, *MNRAS*, 518, 2825
- Mouschovias T. C., Mouschovias Ch. T., 1991, *ApJ*, 373, 169
- Murga M. S., Khoperskov S. A., Wiebe D. S., 2016, *Astron. Rep.*, 60, 233
- Murga M. S., Wiebe D. S., Sivkova E. E., Akimkin V. V., 2019, *MNRAS*, 488, 965
- Murga M. S., Kirsanova M. S., Vasyunin A. I., Pavlyuchenkov Y. N., 2020, *MNRAS*, 497, 2327
- Murray N., Quataert E., Thompson T. A., 2005, *ApJ*, 618, 569
- Murray N., Quataert E., Thompson T. A., 2010, *ApJ*, 709, 191
- Nakai Y., et al., 1991, *NIMPB*, 58, 452
- Narayanan D., et al., 2023, *ApJ*, 951, 100
- Narayanan et al., 2025, *arXiv*
- Novotný O., et al., 2005, *JChPh*, 123, 104303
- Nozawa T., Kozasa T., Habe A., 2006, *ApJ*, 648, 435
- Nozawa T., Kozasa T., Habe A., Dwek E., Umeda H., Tominaga N., Maeda K., Nomoto K., 2007, *ApJ*, 666, 955
- Nozawa T., Maeda K., Kozasa T., Tanaka M., Nomoto K., Umeda H., 2011, *ApJ*, 736, 45
- Okada Y., et al., 2013, *A&A*, 553, A2
- Omont A., Bettinger H. F., 2021, *A&A*, 650, A193
- Omont A., Bettinger H. F., Omont A., Bettinger H. F., 2025, *A&A*, 696, A180
- Omukai K., Tsuribe T., Schneider R., Ferrara A., 2005, *ApJ*, 626, 627
- Omukai K., Hosokawa T., Yoshida N., 2010, *ApJ*, 722, 1793
- Ormel C. W., Cuzzi J. N., 2007, *A&A*, 466, 413
- Ormel C. W., Paszun D., Dominik C., Tielens A. G., 2009, *A&A*, 502, 845
- Pallottini A., Ferrara A., 2023, *A&A*, 677, 4
- Parente M., Ragone-Figueroa C., Granato G. L., Borgani S., Murante G., Valentini M., Bressan A., Lapi A., 2022, *MNRAS*, 515, 2053
- Parente M., Parente Massimiliano 2025, *arXiv*, p. arXiv:2504.10585
- Parker D. S., Zhang F., Kim Y. S., Kaiser R. I., Landera A., Kislov V. V., Mebel A. M., Tielens A. G., 2012, *Proc. Natl. Acad. Sci. U. S. A.*, 109, 53
- Peeters E., Hony S., Van Kerckhoven C., Tielens A. G., Allamandola L. J., Hudgins D. M., Bauschlicher C. W., 2002, *A&A*, 390, 1089
- Peeters E., Spoon H. W. W., Tielens A. G. G. M., 2004, *ApJ*, 613, 986
- Pilleri P., Montillaud J., Berné O., Joblin C., 2012, *A&A*, 542, A69
- Pirronello V., Liu C., Shen L., Vidali G., 1996, *ApJL*, 475, L69
- Pirronello V., Biham O., Liu C., Shen L., Vidali G., 1997, *ApJL*, 483, L131
- Pirronello V., Liu C., Roser J. E., Vidali G., Pirronello V., Liu C., Roser J. E., Vidali G., 1999, *A&A*, 344, 681
- Poppe T., Blum J., Poppe T., Blum J., 1997, *AdSpR*, 20, 1595
- Popping G., Somerville R. S., Galametz M., 2017, *MNRAS*, 471, 3152
- Predehl P., Schmitt J. H. M. M., 1995, *A&A*, 293, 889
- Purcell E. M., Purcell M. E., 1976, *ApJ*, 206, 685
- Puska M. J., Nieminen R. M., Puska M. J., Nieminen R. M., 1983, *PhRvB*, 27, 6121
- Rachford B. L., et al., 2002, *ApJ*, 577, 221
- Ragone-Figueroa C., Granato G. L., Parente M., Murante G., Valentini M., Borgani S., Maio U., 2024, *A&A*, 691, A200
- Rapacioli M., Calvo F., Spiegelman F., Joblin C., Wales D. J., 2005, *J. Phys. Chem. A*, 109, 2487
- Rapacioli M., Calvo F., Joblin C., Parneix P., Toubblanc D., Spiegelman F., 2006, *A&A*, 460, 519
- Rau S. J., Hirashita H., Murga M., 2019, *MNRAS*, 489, 5218
- Rauls E., Hornekær L., Rauls E., Hornekær L., 2008, *ApJ*, 679, 531
- Reach W. T., et al., 2005, *AJ*, 131, 1479
- Rebrion-Rowe C., et al., 2003, *IJMSP*, 223-224, 237
- Reizer E., Viskolcz B., Fiser B., 2022, *Chemosphere*, 291, 132793
- Relanó M., et al., 2016, *A&A*, 595, A43
- Rémy-Ruyer A., et al., 2014, *A&A*, 563, A31
- Rémy-Ruyer A., et al., 2015, *A&A*, 582, A121
- Richter H., Howard J. B., 2002, *PCCP*, 4, 2038
- Rimola A., Ceccarelli C., Balucani N., Ugliengo P., 2021, *Frontiers in Astronomy and Space Sciences*, 8, 655405
- Ritter C., Herwig F., Jones S., Pignatari M., Fryer C., Hirschi R., 2018, *MNRAS*, 480, 538
- Rodríguez M. J., et al., 2025, *ApJ*, 983, 137
- Romano L. E., Nagamine K., Hirashita H., 2022a, *MNRAS*, 514, 1441
- Romano L. E. C., Nagamine K., Hirashita H., 2022b, *MNRAS*, 514, 1461
- Rosdahl J., Teyssier R., 2015, *MNRAS*, 449, 4380
- Rosdahl J., Blaizot J., Aubert D., Stranex T., Teyssier R., 2013, *MNRAS*, 436, 2188
- Rosdahl J., Schaye J., Teyssier R., Agertz O., 2015, *MNRAS*, 451, 34
- Rosdahl J., et al., 2018, *MNRAS*, 479, 994
- Roser J. E., Ricca A., 2015, *ApJ*, 801, 108
- Roy A., et al., 2012, *ApJ*, 763, 55
- Sandstrom K. M., Bolatto A. D., Draine B. T., Bot C., Stanimirović S., 2010, *ApJ*, 715, 701
- Sandstrom K. M., et al., 2012, *ApJ*, 744
- Sandstrom K. M., et al., 2023, *ApJL*, 944, L8
- Schaerer D., Meynet G., Maeder A., Schaller G., Schaerer D., Meynet G., Maeder A., Schaller G., 1993, *A&AS*, 98, 523
- Schlathölder T., Hadjar O., Hoekstra R., Morgenstern R., Schlathölder T., Hadjar O., Hoekstra R., Morgenstern R., 1999, *PhRvL*, 82, 73
- Schneider R., Maiolino R., 2024, *A&A Review*, 32, 2
- Schneider R., Omukai K., 2010, *MNRAS*, 402, 429
- Schneider R., Ferrara A., Natarajan P., Omukai K., 2002, *ApJ*, 571, 30
- Schneider R., Omukai K., Inoue A., Ferrara A., 2006, *MNRAS*, 369, 1437
- Schutte W. A., 1995, *Adv. Space Res.*, 16, 53
- Seitzzahl I. R., et al., 2013, *MNRAS*, 429, 1156
- Seok J. Y., Hirashita H., Asano R. S., 2014, *MNRAS*, 439, 2186
- Seok J. Y., Koo B.-C., Hirashita H., 2015, *ApJ*, 807, 100

- Serra Díaz-Cano L., Jones A. P., Serra Díaz-Cano L., Jones A. P., 2008, *A&A*, 492, 127
- Sheffer Y., Rogers M., Federman S. R., Abel N. P., Gredel R., Lambert D. L., Shaw G., 2008, *ApJ*, 687, 1075
- Shivaei I., et al., 2017, *ApJ*, 837, 157
- Shivaei I., et al., 2024, *A&A*, 690, A89
- Shukla B., Koshi M., 2010, *PCCP*, 12, 2427
- Shukla B., Koshi M., 2012, *Combust. Flame*, 159, 3589
- Shukla B., Susa A., Miyoshi A., Koshi M., 2008, *The Journal of Physical Chemistry A*, 112, 2362
- Sigmund P., 1969, *PhRv*, 184, 383
- Sigmund P., 1981, in Behrisch R., ed., , Vol. 47, Sputtering by Particle Bombardment I: Physical Sputtering of Single-Element Solids. Springer-Verlag, p. 9, doi:10.1007/3540105212_7
- Sigmund P., 1996, *Phys. Rev. A*, 54, 3113
- Sigmund P., 2014, *Springer Ser. Solid-State Sci.*, 179, 343
- Silsbee K., Caselli P., Ivlev A. V., 2021, *MNRAS*, 507, 6205
- Slavin J. D., Dwek E., Jones A. P., 2015, *ApJ*, 803, 7
- Slavin J. D., Dwek E., Low M.-M. M., Hill A. S., 2020, *ApJ*, 902, 135
- Sloan G. C., et al., 2007, *ApJ*, 664, 1144
- Sloan G. C., Sloan C. G., 2017, *P&SS*, 149, 32
- Smolders K., et al., 2010, *A&A*, 514, L1
- Snow T. P., Bierbaum V. M., Snow T. P., Bierbaum V. M., 2008, *ARAC*, 1, 229
- Sofia U. J., Meyer D. M., Sofia U. J., Meyer D. M., 2001, *ApJL*, 554, L221
- Spitzer Lyman J., Spitzer Lyman Jr. 1948, *ApJ*, 107, 6
- Stanway E. R., Eldridge J. J., 2018, *MNRAS*, 479, 75
- Stepnik B., et al., 2003, *A&A*, 398, 551
- Sutherland R. S., Dopita M. A., 1993, *ApJS*, 88, 253
- Sutter J., et al., 2024, *ApJ*, 971, 178
- Taniguchi K., et al., 2025, *ApJ*, 993, 104
- Tappe A., Rho J., Reach W. T., Tappe A., Rho J., Reach W. T., 2006, *ApJ*, 653, 267
- Temim T., Dwek E., 2013, *ApJ*, 774, 8
- Teyssier R., 2002, *A&A*, 385, 337
- Thompson T. A., Quataert E., Murray N., 2005, *ApJ*, 630, 167
- Thompson O. A., Richings A. J., Gibson B. K., Faucher-Giguère C. A., Feldmann R., Hayward C. C., 2024, *MNRAS*, 532, 1948
- Thrower J. D., et al., 2012, *ApJ*, 752, 3
- Tielens A. G. G. M., 2005, *The Physics and Chemistry of the Interstellar Medium*. Cambridge University Press, doi:10.1017/CBO9780511819056, https://www.cambridge.org/core/product/identifier/9780511819056/type/book
- Tielens A., 2008, *ARA&A*, 46, 289
- Tielens A. G. G. M., 2021, *Molecular Astrophysics*. Cambridge University Press, doi:10.1017/9781316718490, https://www.cambridge.org/core/product/identifier/9781316718490/type/book
- Tielens A. G. G. M., Hagen W., 1982, *A&A*, 114, 245
- Tielens A. G. G. M., McKee C. F., Seab C. G., Hollenbach D. J., Tielens A. G. G. M., McKee C. F., Seab C. G., Hollenbach D. J., 1994, *ApJ*, 431, 321
- Tobita S., et al., 1992, *CP*, 161, 501
- Totton T. S., Misquitta A. J., Kraft M., 2012, *PCCP*, 14, 4081
- Trayford J. W., et al., 2025, *MNRAS*, 000, 1
- Trebitsch M., et al., 2021, *A&A*, 653, A154
- Vasiliev E. O., 2025, *arXiv*, p. arXiv:2512.24677
- Vasiliev E. O., Nath B. B., 2025, *arXiv*, p. arXiv:2512.24670
- Verstraete L., 2021, *PAHs and the Universe*, pp 415–426
- Verstraete L., Leger A., D’Hendecourt L., Defourneau D., Dutuit O., 1990, *A&A*, 237, 436
- Verstraete L., et al., 2001, *A&A*, 372, 981
- Vijayan A. P., Clay S. J., Thomas P. A., Yates R. M., Wilkins S. M., Henriques B. M., 2019, *MNRAS*, 489, 4072
- Virtanen P., et al., 2020, *Nat. Methods*, 17, 261
- Voelk H. J., Jones F. C., Morfill G. E., Roeser S., 1980, *A&A*, 85, 316
- Vogelsberger M., Mckinnon R., O’neil S., Marinacci F., Torrey P., Kannan R., 2019, *MNRAS*, 487, 4870
- Wakelam V., et al., 2017, *Mol. Astrophys.*, 9, 1
- Weingartner J. C., Draine B. T., 1999, *ApJ*, 517, 292
- Weingartner J. C., Draine B. T., 2000, *ApJ*, 548, 296
- Weingartner J. C., Draine B. T., 2001a, *ApJS*, 134, 263
- Weingartner J., Draine B., 2001b, *ApJ*, 548, 296
- Weingartner J. C., Draine B. T., 2001c, *ApJ*, 563, 842
- Wenzel G., et al., 2020, *A&A*, 641, A98
- Wenzel G., et al., 2024, *Science*, 386, 810
- Wenzel G., et al., 2025, *ApJL*, 984, L36
- Whitcomb C. M., et al., 2024, *ApJ*, 974, 20
- Wiseman P., Schady P., Bolmer J., Krühler T., Yates R. M., Greiner J., Fynbo J. P., 2017, *A&A*, 599, 24
- Wolfire M. G., McKee C. F., Hollenbach D., Tielens A. G. G. M., 2003, *ApJ*, 587, 278
- Wolfire M. G., Tielens A. G. G. M., Hollenbach D., Kaufman M. J., 2008, *ApJ*, 680, 384
- Yan H., Lazarian A., 2002, *ApJL*, 592, L33
- Yan H., Lazarian A., Draine B. T., 2004, *ApJ*, 616, 895
- Zacharia R., Ulbricht H., Hertel T., 2004, *Phys. Rev. B*, 69, 155406
- Zhang F., et al., 2010, *JACHS*, 132, 2672
- Zhang Z., Ye L., Li M., Bi Y., Cong H., 2025, *Appl. Energy Combust. Sci.*, 24, 100391
- Zhao L., et al., 2018, *Nat. Astron.*, 2, 973
- Zhao H., Chen B., Li J., Zhao H., Chen B., Li J., 2025, *ApJL*, 991, L36
- Zhen J., Castellanos P., Paardekooper D. M., Linnartz H., Tielens A. G., 2014, *ApJL*, 797
- Zhen J., Castellanos P., Paardekooper D. M., Ligterink N., Linnartz H., Nahon L., Joblin C., Tielens A. G., 2015, *ApJL*, 804, L7
- Zhen J., et al., 2016, *ApJ*, 822, 113
- Zhu Z., Stone J. M., Bai X. N., 2015, *ApJ*, 801, 81
- Zhukovska S., 2014, *A&A*, 562, 76
- Zhukovska S., Gail H. P., Tieloff M., 2008, *A&A*, 479, 453
- Zhukovska S., Dobbs C., Jenkins E. B., Klessen R. S., 2016, *ApJ*, 831, 147
- Zhukovska S., Henning T., Dobbs C., 2018, *ApJ*, 857, 94
- Ziegler J. F., Biersack J. P., Ziegler J. F., Biersack J. P., 1985, *this*, p. 93
- Zubko V., Dwek E., Arendt R. G., 2004, *ApJS*, 152, 211
- van Hoof P. A. M., Weingartner J. C., Martin P. G., Volk K., Ferland G. J., 2004, *MNRAS*, 350, 1330
- van der Velden E., 2020, *JOSS*, 5, 2004

- Photoelectric emission (rate per grain):

$$J_{\text{pe}}(Q_g) = \int_{\nu_{\text{pet}}}^{\nu_{\text{max}}} \frac{c u_\nu}{h\nu} Y(Q_g, E) C_{\text{abs}}(\nu, a) d\nu + \int_{\nu_{\text{pd}}}^{\nu_{\text{max}}} \frac{c u_\nu}{h\nu} \sigma_{\text{pd}}(\nu, Q_g, a) d\nu. \quad (\text{A1})$$

The first term captures the photo-emission of valence electrons, whereas the second term considers the photo-detachment of captured electrons residing in the “lowest unoccupied molecular orbit” when $Q_g < 0$. Here u_ν is the radiation energy density per unit frequency, $C_{\text{abs}}(\nu, a)$ is the grain absorption cross section for radius a , $Y(Q_g, E)$ is the photoelectric yield as a function

APPENDIX

A. NUMERICAL IMPLEMENTATION OF EQUILIBRIUM DUST CHARGING

We compute the equilibrium probability distribution $P(Q_g)$ for a grain to possess integer charge Q_{mg} by enforcing detailed balance among the microphysical charging channels. The dominant processes included in the present implementation are (Weingartner & Draine 2001a):

of emitted-electron energy E and grain charge Q_g , and $\sigma_{\text{pd}}(\nu, Q_g, a)$ denotes the photo-detachment cross section. The integrals over radiation bins are limited at the top by the maximum radiation energy ν_{max} (e.g. 13.6 eV), the photo-emission threshold energy ν_{pet} , and the photo-detachment threshold energy ν_{pd} . We use dust cross sections from [Draine et al. \(1984\)](#); [Laor & Draine \(1993\)](#); [Weingartner & Draine \(2000\)](#) and the dielectric tables from [Draine \(2003b\)](#).

- Electron recombination and collisional charging by ions and electrons (rate per grain, per collisional species):

$$J_i(Q_g) = n_i s_i(Q_g) \left(\frac{8k_B T}{\pi m_i} \right)^{1/2} \pi a^2 \tilde{J}(Q_g, T, q_i), \quad (\text{A2})$$

where n_i is the number densities of electrons and ions with charge q_i and mass m_i , s_i their sticking coefficient, and $\tilde{J}(Q_g, T, q_i)$ is the Coulomb focusing function from [Draine & Sutin \(1987\)](#). This expression assumes a Maxwellian distribution of collisional species.

For compact notation we denote the net upward transition rate (loss of one electron) from Q_g to $Q_g + 1$ by $R^+(Q_g)$ and the downward transition rate (gain of one electron) by $R^-(Q_g)$. The key insight from steady state is that the detailed-balance recurrence yields:

$$P(Q_g + 1) = P(Q_g) \frac{R^+(Q_g)}{R^-(Q_g + 1)}. \quad (\text{A3})$$

Normalisation is imposed by requiring $\sum_{Q_g} P(Q_g) = 1$ after truncating the charge domain to a finite bracket $Q_{\text{min}} \dots Q_{\text{max}}$ chosen so that the tail probabilities at the boundaries are below a user-specified tolerance. We have found that $\sim 10^{-8}$ is sufficient for converged distributions at all relevant ISM conditions. We also impose physical limits to the GCD, given by the most negative allowed charge Q_{min} before auto-ionisation occurs, and the maximum positive charge Q_{max} allowed by the ionisation potential (IPV) for $h\nu_{\text{max}}$ (see equations 24 and eq. 23 in [Weingartner & Draine 2001a](#)).

The algorithm uses the following strategy to select a reference charge Q_{peak} and the bounds of the GCD:

1. The most probable charge Q_{peak} should occur approximately when $R^+(Q_g) \simeq R^-(Q_g + 1)$. Starting at $Q_g = 0$, the code steps up or down until:

$$r(Q_g) = \frac{R^+(Q_g)}{R^-(Q_g + 1)} \quad (\text{A4})$$

crosses 1. The crossing point is used as Q_{peak} .

2. Moving up and down from Q_{peak} , the probability distributions is computed until the lower bound $P(Q_{\text{lower}}) \rightarrow \epsilon$ and upper bound $P(Q_{\text{upper}}) \rightarrow \epsilon$ (where ϵ is the tolerance error).

Many of the $R^+(Q_g)$ and $R^-(Q_g + 1)$ computed during the search of Q_{peak} can be saved and used afterwards during the computation of the $P(Q_g)$ distribution with

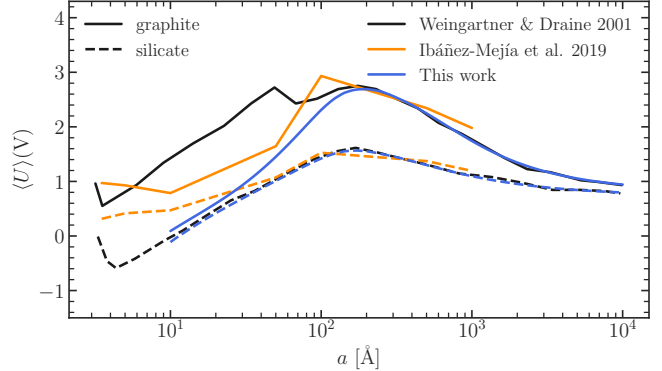


FIG. A1.—: Average electrostatic potential of dust grains embedded in the WNM irradiated with the [Mathis et al. \(1983\)](#) ISRF. Solid lines are for graphite grains, while dashed lines are for silicates. We compare the results of our model (blue lines) with the results from [Weingartner & Draine \(2001a\)](#) (black lines) and [Ibanez-Mejia et al. \(2019\)](#) (orange lines). Our results are in broad agreement with the original model by [Weingartner & Draine \(2001a\)](#), although our choice of pure graphitic grains for $a \lesssim 100 \text{ \AA}$ results in lower UV absorption efficiencies compared to the PAH+graphite mixture in [Weingartner & Draine \(2001a\)](#).

the detail balance recurrence. This is a key optimisation feature of our method.

We test our implementation by computing the average electrostatic potential:

$$U = \frac{eQ_g}{4\pi\epsilon_0 a}, \quad (\text{A5})$$

for grain of different sizes and compositions embedded in the [Mathis et al. \(1983\)](#) ISRF and within the WNM medium (i.e. $n_e = 0.03 \text{ cm}^{-3}$ and $T = 6000 \text{ K}$). ϵ_0 is the vacuum permittivity. The results in figure 10 of [Weingartner & Draine \(2001a\)](#) are shown in Fig. A1 with black solid (dashed) lines for graphite (silicate) grains. For the same compositions, our model results in the blue curves, which we have computed down to the minimum size allowed by the optical properties in [Draine et al. \(1984\)](#). Our results are in excellent agreement with [Weingartner & Draine \(2001a\)](#), except for graphite grains of radius below 100 \AA . The origin of this discrepancy is the choice of optical properties for very small graphite grains in [Weingartner & Draine \(2001a\)](#), which are not the pure graphite properties used in CALIMA, but rather with a mixture of PAH optical properties as described [Li & Draine \(2001\)](#). Given that within this regime of very small graphite grains in CALIMA we transition to the contribution of PAHs, we regard this discrepancy as a feature of our choice of dust discretisation. For comparison, we also show the prediction from fitting functions by [Ibanez-Mejia et al. \(2019\)](#) as orange lines. Our results are in overall agreement with theirs in the regime of $a \gtrsim 100 \text{ \AA}$, but we find significant deviations for smaller sizes, with their prediction of small silicates exceeding both ours and [Weingartner & Draine \(2001a\)](#).

	s [g cm ⁻³]	U_0 [eV]	K	$\langle Z_j \rangle$	$\langle m_j^{\text{atom}} \rangle$ [a.m.u.]	$\langle N_{\text{val}} \rangle$	Q_{d}^* [dyn cm g ⁻¹]
Carbon	2.2	4.0	0.61	6	12.011	4	8.9×10^9
Silicate	3.3	5.7	0.10	12	24.605	5	4.3×10^{10}

TABLE A1: Fiducial material parameters for dust species. From left to right: bulk material density, work function, normalization factor in the photoelectric yield model, mean atomic number, mean atomic mass, average number of valence electrons, and dust specific binding energy.

A.1. The interaction of dust grains with high energy ions

The thermal sputtering rate is a function of the velocity of the incident gas particles (ions, atoms or molecules) which is determined by the gas temperature (e.g. Barlow et al. 1978; Draine & Salpeter 1979):

$$\frac{da_i}{dt} = \frac{\langle m_i^{\text{atom}} \rangle}{2s_i} \sum_k n_k \langle Y_k v \rangle, \quad (\text{A6})$$

where $\langle m_i^{\text{atom}} \rangle$ is the average atomic mass of the dust grain in bin i , s_i is the material density of the dust grain, and $\langle Y_k v \rangle$ is the sputtering yield of gas species k defined as the mean number of emitted atoms per incident particle averaged over the Maxwellian distribution f_M :

$$\langle Y_k v \rangle = \int_0^\infty Y_k(E) v f_M(v) dv, \quad (\text{A7})$$

where $E = m_k v^2/2 + Z_k e Q_{g,i}/a_i$ is the energy of the incident gas particle, Z_k is the charge of the ion, e is the elementary charge, and $Q_{g,i}$ and a_i are the charge and radius of the dust grain bin i involved in the collision. The sputtering yields due to particle k impacting at normal incidence with energy E is given by equation 11 in Nozawa et al. (2006):

$$Y_k(E) = 4.2 \times 10^{14} \frac{S_k(E)}{U_0} \frac{\alpha_k(\mu_k)}{K\mu_k + 1} \times \left[1 - \left(\frac{E_{\text{sp}}}{E} \right)^{\frac{2}{3}} \right] \left(1 - \frac{E_{\text{sp}}}{E} \right)^2. \quad (\text{A8})$$

where U_0 is the surface binding energy in units of eV, $\mu_k = \langle m_i^{\text{atom}} \rangle / m_k$ is the ratio of the average atomic mass number of the dust grain and the impinging ion, α_k is a function of μ_k and is discussed further below, and K is a free parameter which is used to calibrate this analytic function for $Y_k(E)$ to experimental data (Tielens et al. 1994). Incident gas particles can cause sputtering of dust grains if their energies are equal or above the threshold energy E_{sp} given by (Bohdansky et al. 1980; Andersen & Bay 1981):

$$E_{\text{sp}} = \begin{cases} \frac{U_0}{4 \langle m_i^{\text{atom}} \rangle m_k} \frac{(\langle m_i^{\text{atom}} \rangle + m_k)^4}{(\langle m_i^{\text{atom}} \rangle - m_k)^2}, & \text{if } \frac{m_k}{\langle m_i^{\text{atom}} \rangle} \leq 0.3, \\ 8U_0 \left(\frac{m_k}{\langle m_i^{\text{atom}} \rangle} \right)^{1/3}, & \text{if } \frac{m_k}{\langle m_i^{\text{atom}} \rangle} > 0.3. \end{cases} \quad (\text{A9})$$

In Eq. A8 we also introduced the nuclear stopping cross-section $S_k(E)$ in units of erg cm² given by (Sigmund 1981):

$$S_k(E) = 4\pi a_{\text{sc}} Z_k \langle Z_i \rangle e^2 \frac{m_k}{m_k + \langle m_i^{\text{atom}} \rangle} \iota_k(\epsilon_k), \quad (\text{A10})$$

where Z_k and $\langle Z_j \rangle$ are the atomic number for the ion and the grain average atomic number. The screening length

	p_1	p_2	p_3	p_4	p_5	p_6	q_1	q_2	q_3
C-dust	4.9	0.55	0.77	4.7	3.0	1.2	4.51	0.92	0.40
Sil-dust	1.5	1.2	0.57	1.1	0.52	0.37	1.48	1.31	0.59

TABLE A2: Fitting parameters for the size-dependent correction of thermal sputtering yields. Columns list the coefficients p_i and q_i defining Eq. A15 for carbonaceous and silicate grains.

for the interaction potential between the nuclei is given by:

$$a_{\text{sc}} = 0.885 a_0 (Z_k^{2/3} + \langle Z_j \rangle^{2/3})^{-1/2}, \quad (\text{A11})$$

with the Bohr radius $a_0 = 0.529 \text{ \AA}$. The function $\iota_k(\epsilon_k)$ encapsulates the details of the screened Coulomb interaction and can be approximated by (Matsunami 1980):

$$\iota_k(\epsilon_k) = \frac{3.441 \sqrt{\epsilon_k} \ln(\epsilon_k + 2.718)}{1 + 6.35 \sqrt{\epsilon_k} + \epsilon_k(-1.708 + 6.882 \sqrt{\epsilon_k})}, \quad (\text{A12})$$

with the reduced energy defined as:

$$\epsilon_k = \frac{\langle m_i^{\text{atom}} \rangle}{m_k + \langle m_i^{\text{atom}} \rangle} \frac{a_{\text{sc}}}{Z_k \langle Z_i \rangle e^2} E. \quad (\text{A13})$$

The α_k function encapsulates how the energy is distributed in the material upon collision of the incident particle (see Sigmund 1969, for further details). We use the updated version of the Bohdansky (1984) approximation obtained by Nozawa et al. (2006) based on sputtering data:

$$\alpha_k = \begin{cases} 0.2, & \text{if } \mu_k \leq 0.5, \\ 0.1\mu_k^{-1} + 0.25(\mu_k - 0.5)^2, & \text{if } 0.5 < \mu_k \leq 1, \\ 0.3(\mu_k - 0.6)^{2/3}, & \text{otherwise.} \end{cases} \quad (\text{A14})$$

We refer to Table A1 for the relevant material parameters required for the expressions presented in this derivation. The experimental yields that were used to calibrate the analytic expression for $Y_k(E)$, and to hence derive the value of K , were measured for a semi-infinite target, rather than finite size dust grains (e.g. Tielens et al. 1994). The semi-infinite target approximation may break down for small grains and for sufficiently high gas temperatures. First proposed by Jurac et al. (1998), a size-dependent sputtering yield arises from the consideration that if the grain size is close to the stopping length (or penetration depth, i.e. r_{pd}), then the energy deposition per unit mass of the grain will be maximal. We apply the results of the size-dependent sputtering yield model by Bocchio et al. (2012); Bocchio et al. (2014) who obtain multi-Gaussian fittings to the correction function $f(x)$ between the sputtering yield of a semi-infinite target Y_∞ and the sputtering yield Y_a of a grain of finite radius a , $Y_a = f(x)Y_\infty$. We have further modified $f(x)$

to prevent unstable behaviour in the $x \ll 1$ regime:

$$f(x) = \begin{cases} 1 + p_1 \exp\left[-\frac{(\ln(x/p_2))^2}{2p_3^2}\right] & \text{if } x \geq 1, \\ -p_4 \exp\left[-(p_5x - p_6)^2\right], & \\ q_1 \exp\left[-\frac{(\ln(x/q_2))^2}{2q_3^2}\right], & \text{otherwise.} \end{cases} \quad (\text{A15})$$

where the fitting parameters are given in Table A2 and $x = a/(0.7r_{\text{pd}})$. The 0.7 factor comes from the fact that the ion usually loses the majority of its energy after it has travelled $\sim 0.7r_{\text{pd}}$ through the grain material (e.g. Serra Díaz-Cano et al. 2008). The penetration depth and the effective value of Y_a are the result of very complex theoretical work using codes like the Stopping and Range of Ions in Matter (SRIM; Ziegler et al. 1985). For CALIMA we instead estimate the value of r_{pd} via the integration of the total stopping power considering nuclear and electronic interactions derived in Section 2.6. As an example, we present in Fig. 6 the erosion rate $(da/dt)/n_{\text{H}}$ for the different dust species considering the finite size correction detailed above.

A.2. Energy transfer in dust-gas collisions

The collisional model by Hollenbach & Mckee (1979) is based on the *soft-cube* model (Logan et al. 1968) applied to the thermal accommodation of gas particles onto dust grain surfaces (Burke & Hollenbach 1983). Essentially, this model assumes that a grain surface can be approximated by an array of square particles attached by a spring to an infinite mass (the lattice). The infinitesimal collisional rate onto grain surface area dA by a gas particle with mass m , number density n , and following a Maxwell-Boltzmann velocity distribution at temperature T , is given by:

$$\begin{aligned} d\Gamma &= ndA \int_{v_z > 0} \left(\frac{m}{2\pi k_{\text{B}}T}\right)^{3/2} \exp\left(-\frac{mv^2}{2k_{\text{B}}T}\right) v_z d^3v \\ &= ndA \sqrt{\frac{k_{\text{B}}T}{2\pi m}}, \end{aligned} \quad (\text{A16})$$

where we have assumed the $x - y$ plane is parallel to the grain surface, such that only particles with $v_z > 0$ can reach the surface. Taking the integral over the full surface of the grain $4\pi a^2$ gives the total collisional rate as:

$$\Gamma = \pi na^2 \sqrt{\frac{8k_{\text{B}}T}{\pi m}}. \quad (\text{A17})$$

By a similar calculation, we can derive the average kinetic energy of the colliding gas particles $\langle E_{\text{kin}} \rangle = 2k_{\text{B}}T$. Therefore, we can express the energy transfer rate for a gas particle with mass m onto a dust grain of radius a and temperature T_{d} (Hollenbach & Mckee 1979):

$$H_{\text{coll}}(a, T) = \sqrt{\frac{8k_{\text{B}}T}{\pi m}} \pi na^2 2k_{\text{B}}(T - T_{\text{d}}) \mathcal{A}(T), \quad (\text{A18})$$

where the term in parenthesis indicates that the energy transfer goes to zero when $T = T_{\text{d}}$ and allows for gas heating when $T_{\text{d}} > T$. The parameter $\mathcal{A}(T)$ encapsulates the efficiency of energy transfer from the gas atom to the

dust grain, termed the *accommodation* factor (Burke & Hollenbach 1983). This is usually assumed to be of order unity, with a small dependence on the gas and dust temperatures in the range $\sim 10 - 1000$ K (see figure 4 in Burke & Hollenbach 1983). The *soft-cube* model is valid as long as the surface is approximately flat from the perspective of the impinging gas atom. However, more energetic gas particles are capable of interacting with a larger region of the grain surface, potentially encountering a more uneven surface topology. This limits the validity of the model to gas temperatures $T \lesssim 10^4$ K, which has not been enforced when implemented in many ISM or cloud collapse models (e.g. Wolfire et al. 2003; Grassi et al. 2014; Bialy & Sternberg 2019; Kim et al. 2023; Katz et al. 2022). We therefore enforce a logistic curve centred on $T = 10^4$ K, allowing for a smooth transition between the regime of applicability for Eq. A18, to the hard-sphere regime at high temperature (e.g. Lindhard & Nielsen 1962; Sigmund 2014). We note that this will have an appreciable influence on the cooling rates at solar metallicity below $n_{\text{H}} < 1 \text{ cm}^{-3}$ (e.g. see figure 2 in Katz et al. 2022, for the case of the PRISM model). When the low-temperature condition is satisfied, we obtain $\mathcal{A}(T)$ for atomic H and H₂ as (Hollenbach & Mckee 1979):

$$\mathcal{A}_{\text{H,H}_2} = (1 - \mathcal{A}_{\text{H,H}_2}^0) \exp\left(-\sqrt{\frac{2k_{\text{B}}(T + T_{\text{d}})}{D_{\text{H,H}_2}}}\right) + \mathcal{A}_{\text{H,H}_2}^0, \quad (\text{A19})$$

where:

$$\mathcal{A}_{\text{H,H}_2}^0 = \frac{2m_{\text{H,H}_2}m_{\text{d}}}{(m_{\text{H,H}_2} + m_{\text{d}})^2}, \quad (\text{A20})$$

is the hard-sphere limit and $D_{\text{H,H}_2} = 500k_{\text{B}}$ is the depth of the potential well (i.e. the adsorption energy per particle).

As we have seen in Sec. 2.5, the ion-grain interaction in the high-temperature regime brings into play different physics. In this case, ions can get close enough to feel the grain potential and to travel through the grain material. This form of *transmission* is the basis behind the thermal and non-thermal sputtering of dust grains (Draine et al. 1979; Nozawa et al. 2006). Understanding ion transmission through the grain material requires accounting for the interaction of ions with nuclei and electrons, giving rise to an effective drag force. Unfortunately, the topic of a material's stopping power (i.e. the average change in energy of an ion over an infinitesimal path length through the solid) at sub-relativistic velocities remains a question of great debate in the solid-state and nuclear physics community (see Sigmund 2014, for a review on the different models and approximations used to account for the slowing down of ions through solids). In the high energy regime ($E \gg 1 \text{ MeV}$), the Bohr and Bethe stopping equations have been of great use in predicting the transport of heavy ions. However, these theories, when extended to the low energy regime, give negative values for the stopping power below a threshold energy. Given that an ion energy gain is not considered in these theories, the origin of these negative values is an artefact caused by the approximation limits for Bessel functions used in their derivation (Sigmund 1996). Furthermore,

the first Born approximation can only be applied to the most energetic particles that we will encounter in a coronal gas, so the physical meaning of these equations also becomes questionable in these regimes²².

We instead follow the formalism developed by Sigmund (1981) for the nuclear and electronic stopping by graphite and silicate materials. We recall (Section 2.5) that the stopping power is defined as the average energy loss per unit path length, l , through the solid material (Lindhard & Scharff (1964):

$$\frac{dE}{dl} = -N(S_n(E) + S_e(E)), \quad (\text{A21})$$

where N is the nuclear number density, S_n is the nuclear stopping cross-section defined in Eq. A10 and S_e is the electronic stopping cross-section given by the Lindhard & Scharff (1961) equation for an electron gas:

$$S_e(E) = 8\pi\xi_e \frac{Z_k \langle Z_{\text{atom}} \rangle}{\tilde{Z}} a_{\text{sc}} e^2 \frac{v(E)}{v_0}, \quad (\text{A22})$$

with:

$$\tilde{Z} = (Z_k^{2/3} + \langle Z_i \rangle^{2/3})^{3/2}, \quad (\text{A23})$$

for projectile k , and where the average grain atomic number $\langle Z_i \rangle$, and the screening length a_{sc} are as defined in Section 2.5. The factor $\xi_e \simeq Z_k^{1/6}$ was included to improve agreement with experimental penetration depths, and v_0 is given by $v_0 = \sqrt{2E_0/m_e}$ where:

$$E_0 = \frac{\hbar^2}{2m_e} (3\pi^2 \langle N_{\text{val}} \rangle N)^{2/3}, \quad (\text{A24})$$

is the Fermi energy with number density provided by the material valence electrons per atom $\langle N_{\text{val}} \rangle$, and \hbar is the reduced Planck constant. We can now numerically integrate Eq. A21 to determine how an ion of initial energy E slows down as it travels through the graphite and silicate materials of the dust grains modelled in CALIMA.

The heating rate of a dust grain of size a experiencing collisions with a gas atom k with mass m_k , number density n_k and following a Maxwell-Boltzmann distribution $f(E)$ of energies $E = 1/2 m_k v^2$ is given by :

$$H(\vec{\mathcal{P}}_i, T, n_k) = \pi a_i^2 n_k F_C \int f(E) v(E) E \zeta(\vec{\mathcal{P}}_i, E) dE, \quad (\text{A25})$$

where $\vec{\mathcal{P}}_i$ is a vector of the material properties of the grain bin i

$$\vec{\mathcal{P}}_i = (a_i, s_i, \langle Z_i \rangle, \langle m_i^{\text{atom}} \rangle, \langle N_{\text{val}} \rangle), \quad (\text{A26})$$

F_C is the Coulomb enhancement factor (see Section 2.4), and ζ is the fraction of incident ions left in the grain, computed by integrating Eq. A21. Eq. A25 can easily be

²² We note that one of these theories for high energy stopping power, the Bethe-Bloch approximation (Bethe et al. 1930; Bloch et al. 1933), was used in the SN dust modelling by Kirchschrager et al. (2019), resulting in numerically incorrect penetration depths in the low energy regime.

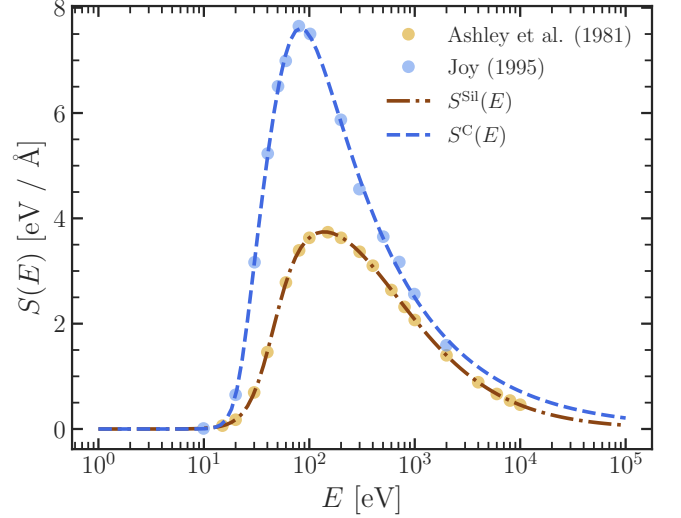


FIG. A2.— Experimental electron stopping power for solid carbon (blue markers) by Joy (1995) and silicon dioxide (yellow markers) by Ashley & Anderson (1981). The dashed lines show the analytical fits for silicate (brown dot-dashed line) and carbonaceous grains (blue dashed line), following Eq. A29.

	SiO ₂	C
a	7.474	-4.280×10^{-4}
b	0.892	-1.221×10^{-16}
c	7.703×10^{-6}	-1.304×10^{-7}
d	0.997	-6.502
e	-2.918	-0.985
f	0.082	-2.614×10^{-4}
g	0.223	1.544
h	0.947	1.524

TABLE A3: Analytical fitting parameters for Eq. A29, describing the electron stopping power in solid carbon (C) and silicon dioxide (SiO₂). Experimental data from Joy (1995) and Ashley & Anderson (1981).

integrated resulting in:

$$H(\vec{\mathcal{P}}_i, T, n_k) = \sqrt{\frac{32}{\pi m_k}} \pi a_i^2 n_k (k_B T)^{3/2} F_C h(\vec{\mathcal{P}}_i, T), \quad (\text{A27})$$

where:

$$h(\vec{\mathcal{P}}_i, T) = \frac{1}{2} \int u^2 \zeta(\vec{\mathcal{P}}_i, E) \exp(-u) du, \quad (\text{A28})$$

is the distribution-averaged heating efficiency function, and $u \equiv E/(k_B T)$. We compute $h(\vec{\mathcal{P}}_i, T)$ for the material properties and sizes of the dust grains in CALIMA, such that a simple linear interpolation in log-log space can be used to compute its value on-the-fly. The other quantities in Eq. A27 are computed on a per-cell basis during the simulation. In gas with temperature below 10^9 K, electrons are still in the sub-relativistic regime. This implies that, outside of the most energetic electrons above ~ 10 keV, the first Born approximation breaks down and the Rutherford cross-section is no longer applicable. In this regime, analytic expressions (e.g. Eq. A22) are a poor predictor of the stopping power of electrons in different solids at low energies (Iskef et al. 1983; Luo et al. 1991; Joy et al. 1996). We therefore follow the approach in

Micelotta et al. (2010a) (see also Section 3.4) and instead determine the energy deposition and penetration depth by obtaining fitting functions to experimental values. For carbonaceous grains we use the experiments on carbon films by Joy (1995), and in the absence of experimental data for astrophysically relevant silicates, we use the experimental data on SiO₂ stopping power by Ashley & Anderson (1981) (see blue and yellow markers in Fig. A2, respectively). We use the fitting equation by Micelotta et al. (2010a) for the stopping power (i.e. dE/dl) of the colliding electrons:

$$S(E) = \frac{h \log(1 + aE_{\text{keV}})}{fE_{\text{keV}}^g + bE_{\text{keV}}^d + cE_{\text{keV}}^e} \text{eV } \text{\AA}^{-1}, \quad (\text{A29})$$

where the E_{keV} is the electron energy in keV and our fitting parameters are given in Table A3²³. We present the results of this fit in Fig. A2, indicating a larger stopping power for carbon than for SiO₂ at the peak stopping efficiency of $\sim 10^2$ eV.

A.3. Subgrid modelling of dust turbulent shattering

The Ormel & Cuzzi model is an updated version of the pioneering work of Voelk et al. (1980). Voelk et al. like models are based on the classification of turbulent eddies according to whether their lifetime (i.e. turnover timescale τ_p) is comparable to the stopping time t_s of the particle (Class I) or not (Class III). In our case the particle is the dust grain. This classification provides a straightforward derivation of the particle-eddy relative velocity and in turn the variance of the particle-particle relative velocity.

We assume that dust particles and gas are coupled to each other via collisions and are in thermal equilibrium, meaning that the final relative velocity between grains is a combination of Brownian motion and the turbulent-induced velocities discussed above. The relative velocity due to thermal (Brownian) motion for two dust particles of masses m_i and m_j is:

$$\Delta V_{ij}^{\text{B}} = \sqrt{\frac{8k_{\text{B}}T(m_i + m_j)}{\pi m_i m_j}}. \quad (\text{A30})$$

In the context of collapsing molecular clouds (e.g. Guillet et al. 2020; Kawasaki et al. 2022a) the forcing timescale for the turbulent cascade is assumed to be the free-fall time of the cloud t_{ff} (e.g. Lebreuilly et al. 2022). In our case, and consistent with the turbulent enhancement of the gas density PDF used for dust metal accretion (see Section 2.4), we consider the local forcing timescale to be $\tau_{\text{L}} = \Delta x_{\text{cell}}/\sigma$ (σ is the local gas velocity dispersion), and the turbulent Mach number is $\mathcal{M} = \sigma/c_s$. Assuming a Kolmogorov turbulent spectrum, the eddy turnover time on the viscous dissipation scale is:

$$\tau_{\eta} = \frac{\tau_{\text{L}}}{\sqrt{\text{Re}}}, \quad (\text{A31})$$

with the Reynolds number, Re , parameterised by the local thermodynamic conditions as $\text{Re} = 6.2 \times$

²³ Note that we have re-computed the fitting values for solid carbon, which has resulted in a minor deviation from the parameters provided in Micelotta et al. (2010a). These differences are negligible.

$10^7 \sqrt{\frac{\rho/\mu}{10^5 \text{cm}^{-3}}} \sqrt{\frac{T_{\text{gas}}}{10\text{K}}}$ (Ormel et al. 2009). The motion of dust particles in a fluid is governed by the drag forces caused by gas²⁴. Based on Epstein's law, the stopping time is:

$$t_s = \frac{sa}{\rho_{\text{gas}} v_{\text{th}}}, \quad (\text{A32})$$

with $v_{\text{th}} = \sqrt{8/\pi} c_s$ the thermal velocity of the gas and s the material density of the grain. Eq. A32 applies when the mean free path l_{mfp} of the gas is larger than the particle size (Commerçon et al. 2023). When this is no longer the case, one should use Stokes' law, with a transition particle size given by the condition $a_{\text{tr}} \geq (9/4)l_{\text{mfp}}$. Given that the largest particle size considered in this work is of 0.1 μm , this corresponds to $n_{\text{H}} \geq 7.5 \times 10^{19} \text{cm}^{-3}$, well out of reach of current galaxy formation simulations. Therefore, it is safe to assume that all dust particles modelled are well within the Epstein regime. Given these definitions of the stopping time and turbulent forcing timescale, we can define the particle Stokes' number as $\text{St} = t_s/\tau_{\text{L}}$.

Consider Stokes' numbers for dust particles i and j with $\text{St}_i \geq \text{St}_j$ (thus $t_s^i \geq t_s^j$ and $m_i \geq m_j$). Ormel & Cuzzi (2007) provide closed forms for the turbulent-induced relative velocities in three limiting regimes dictated by the viscous timescale τ_{η} and the turnover timescale τ_{L} :

$$\Delta V_{ij}^{\text{T}} = \begin{cases} \sqrt{\frac{3}{2}} \sigma \sqrt{\frac{\text{St}_i - \text{St}_j}{\text{St}_i + \text{St}_j}} & \text{if } \tau_{\eta} > t_s^i, \\ \times \sqrt{\frac{\text{St}_i^2}{\text{St}_i + \text{St}_{\text{min}}} - \frac{\text{St}_j^2}{\text{St}_j + \text{St}_{\text{min}}}}, & \\ \sqrt{\frac{3}{2}} \sigma \sqrt{f\left(\frac{\text{St}_j}{\text{St}_i}\right) \text{St}_i}, & \text{if } \tau_{\eta} \leq t_s^i < \tau_{\text{L}}, \\ \sqrt{\frac{3}{2}} \sigma \sqrt{\frac{1}{1 + \text{St}_i} + \frac{1}{1 + \text{St}_j}}, & \text{if } \tau_{\text{L}} \leq t_s^i. \end{cases} \quad (\text{A33})$$

with the function f given by

$$f(x) = 3.2 - (1 + x) + \frac{2}{1 + x} \left(\frac{1}{2.6} + \frac{x^3}{1.6 + x} \right), \quad (\text{A34})$$

and $\text{St}_{\text{min}} \equiv \tau_{\eta}/\tau_{\text{L}} = 1/\sqrt{\text{Re}}$. The final relative velocity is obtained by combining the Brownian and turbulent contributions:

$$\Delta V_{ij} = \sqrt{(\Delta V_{ij}^{\text{B}})^2 + (\Delta V_{ij}^{\text{T}})^2}. \quad (\text{A35})$$

Recall that the collision velocity determines whether shattering, coagulation or simple bouncing²⁵ takes place. Furthermore, in the case of shattering, the energy of the collision determines the fragment distribution that will emerge from the two-body interaction (Jones et al. 1996; Hirashita & Yan 2009), which depends on a number of material properties. Hirashita & Li (2013) showed that

²⁴ This modelling is pure hydrodynamical, so we leave extending this two include magnetohydrodynamical modifications for future work (e.g. Yan et al. 2004).

²⁵ We do not consider effect of deformations on the dust grain geometrical properties.

the most relevant parameter is the velocity threshold for catastrophic fragmentation (i.e. when more than half of the target grain mass is shocked above the grain internal sound speed). Therefore, following [Hirashita & Li \(2013\)](#) we simplify the shattering model using the prescription presented by [Kobayashi & Tanaka \(2010\)](#). We assume that the disrupted mass ejected from m_i is proportional to

$$\phi_{ij} = \frac{E_{\text{imp}}}{m_i Q_d^*}, \quad (\text{A36})$$

where

$$E_{\text{imp}} = \frac{1}{2} \frac{m_i m_j}{m_i + m_j} (\Delta V_{ij})^2, \quad (\text{A37})$$

is the impact energy for m_i colliding with m_j and Q_d^* is the specific impact energy for catastrophic disruption (estimated to be $\simeq 8.9 \times 10^9 \text{ dyn cm g}^{-1}$ for carbonaceous grains and $\simeq 4.3 \times 10^{10} \text{ dyn cm g}^{-1}$ for silicate grains, [Jones et al. 1996](#)). Using ϕ , the ejected mass m_{ej} is estimated as

$$m_{\text{ej}}(\Delta V_{ij}, m_i, m_j) = \frac{\phi_{ij}}{1 + \phi_{ij}} m_i. \quad (\text{A38})$$

The maximum $a_{f,\text{max}}$ and minimum $a_{f,\text{min}}$ sizes of the fragments are taken to be

$$m_{f,\text{max}} = 0.02 m_{\text{ej}}, \quad (\text{A39})$$

$$m_{f,\text{min}} = 10^{-6} m_{f,\text{max}}, \quad (\text{A40})$$

with the fragment mass distribution following (i.e. given the collision of grains of masses m_i and m_j with relative velocity ΔV_{ij} it returns the probability of fragment of mass m)

$$\begin{aligned} \mu_{\text{frag}}(m; \Delta V_{ij}, m_i, m_j) &= \frac{(4 - \alpha_f) m_{\text{ej}} m^{(-\alpha_f + 1)/3}}{3 \left[m_{f,\text{max}}^{(4 - \alpha_f)/3} - m_{f,\text{min}}^{(4 - \alpha_f)/3} \right]} \\ &\quad + (m_i - m_{\text{ej}}) \delta(m - m_i + m_{\text{ej}}), \end{aligned} \quad (\text{A41})$$

where we have dropped the dependence of $m_{\text{ej}}(\Delta V_{ij}, m_i, m_j)$ for clarity. This is a power law distribution with exponent $\alpha_f = 3.3$ in agreement with the results of [Jones et al. \(1996\)](#), plus a remnant fragment of mass $m_i - m_{\text{ej}}$ corresponding to last term on the RHS of the equation (where δ is the dirac delta function).

These results need to be applied and implemented into our discretised dust distribution framework. Equation [A41](#) can be easily integrated over the limits corresponding to large grains, small grains, and in the case of carbonaceous grains, PAHs (see [Section 3](#)), in order to obtain the contribution of the shattered fragments to each bin. Integrating [Eq. A41](#) over the whole spectrum of fragments gives m_x , allowing us to define the fraction of target mass fragments that fall within the dust grain bin centred on grain size a_x and limited by minimum and maximum masses $m_{x,\text{min}}$ and $m_{x,\text{max}}$:

$$\chi_f(a_x; \mathcal{M}, a_i, a_j) \equiv \chi_f(m_x; \Delta V_{ij}, m_i, m_j) \quad (\text{A42})$$

$$= \frac{1}{m_i} \int_{m_{x,\text{min}}}^{m_{x,\text{max}}} \mu_{\text{frag}}(m; \Delta V_{ij}, m_i, m_j) dm. \quad (\text{A43})$$

Using [Eq. A42](#) we define the local timescale of fragment production for a given collision model ([Hirashita & Aoyama 2019](#)):

$$t_{\text{sha}}(a_x; \mathcal{M}, a_i, a_j) = (\sigma_{ij} \Delta V_{ij} n_{d,j} \chi_f)^{-1}, \quad (\text{A44})$$

where we have dropped the arguments of χ_f for clarity, and defined the collision cross section of grains of sizes a_i and a_j as $\sigma_{ij} = \eta_{ij} \pi (a_i + a_j)^2$, where η_{ij} allows for corrections to the geometrical cross section. We choose the simple case $\eta_{ij} = 1$. This definition of the shattering timescale allows us to obtain separate timescales for the production of shattered fragments within different grain size bins. Therefore, for carbonaceous grains we compute the timescales for the production of large grains (i.e. inefficient shattering), small grains, PAHs and full destruction (i.e. return to the gas phase). We do similar calculations for silicates, except that we do not follow the shattering of very small grains in this case; instead every fragment below 4.5 \AA is considered to return to the gas phase. This is based on the result that smaller silicate grains are photolytically unstable in the ISM ([Guhathakurta et al. 1989](#)). We only consider silicate-silicate, or carbon-carbon collisions, i.e. we do not allow silicate-carbon collisions. Following [Hirashita & Li \(2013\)](#), we posit that approaching particles have a uniform probability of hitting each other from any direction, so we obtain maximum and minimum estimates for the relative velocity given by head-on collisions and tangential collisions, respectively.

[Fig. A3](#) shows the results of this turbulent shattering model for carbonaceous grains in the WIM as defined in [Table 1 of Yan et al. \(2004\)](#). In the left panel we consider collisions of large grains with other large grains (i.e. $m_i = m_j$), whereas in the right panel we consider the collisions of large and small grains (i.e. $m_i > m_j$). We show the fragment mass fraction χ_{frag} (see [Eq. A42](#)) which indicates what mass of the fragment distribution falls under the limits of each of the PAH and carbonaceous dust grain bins. In order to put our results within the context of previous treatments of the shattering timescale, we also compare the results of the [Ormel & Cuzzi \(2007\)](#) model to [Hirashita & Aoyama \(2019\)](#) (see their [Appendix C](#)). This modelling assumes that the particle sits in the intermediate regime given in [Eq. A33](#), which is a good approximation for the molecular ISM, but not for the high \mathcal{M} typical of the WNM or WIM. The results using the [Hirashita & Aoyama \(2019\)](#) model is represented in [Fig. A3](#) by the shaded bands. Compared to our fiducial implementation using the [Ormel & Cuzzi \(2007\)](#) model, we find that the [Hirashita & Aoyama \(2019\)](#) model strongly underestimates the fragmentation of large grains at low to intermediate \mathcal{M} . This approximated form only becomes valid at very high \mathcal{M} . The results of the approximation are even less reliable for the case of non-equal mass collisions (see right panel).

Independent of the velocity model assumed, shattering in large-large grain collisions in transonic turbulence results in the efficient production of small shattering fragments, allowing for $\sim 1\%$ and $\sim 20\%$ mass fraction in small PAHs and large PAHs. We therefore expect shattering of large grains to be an interesting process for the top-down formation of PAHs ([Seok et al. 2014](#)). Additionally, our fiducial model finds that the production

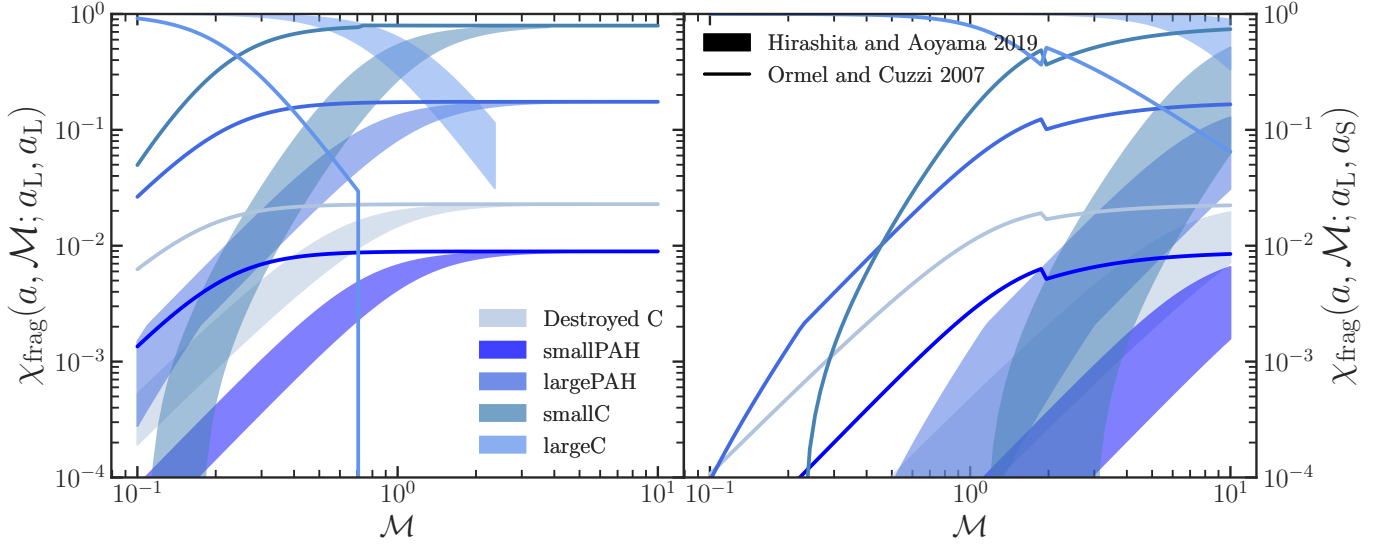


FIG. A3.—: Carbonaceous shattering fragment mass fraction versus turbulent Mach number in the WIM ($n_{\text{H}} = 0.1 \text{ cm}^{-3}$) for the turbulent shattering models detailed in Section 2.8. Each line and shaded area colour indicates different bins of PAHs and carbonaceous grains. Shattering is computed using either: (i) our fiducial model based on the collision velocity results of Ormel & Cuzzi (2007) (solid lines), or (ii) our model with the basic velocity scaling from Hirashita & Aoyama (2019) (shaded regions). *Left panel:* Results for the models using only the collisions between two large grains with $a_{\text{L}} = 0.1 \mu\text{m}$. *Right panel:* Results for the collision between a large grain $a_{\text{L}} = 0.1 \mu\text{m}$ and a small grain $a_{\text{S}} = 0.01 \mu\text{m}$. Collisions between large grains in the WIM allow for efficient shattering of large grains into smaller grains. The basic modelling by Hirashita & Aoyama (2019) significantly underestimates the shattering efficiency at low \mathcal{M} . Big-small grain collisions only become relevant for supersonic turbulence.

of small and very small shattered fragments through the collision of large grains and small grains may become important in highly turbulent systems at high redshift (e.g. Falgarone et al. 2017).

A.4. Revisiting PAH sputtering

Ion-PAH collisions can be described by the simultaneous processes of nuclear stopping (elastic energy loss), and electronic stopping (inelastic energy loss). Nuclear stopping involves a binary collision of an ion with a single atom of a PAH molecule. If the collision energy exceeds the threshold for atom removal, the atom is ejected. For electronic stopping, the interaction is instead between the electrons of the PAH and the projectile ion. The transferred energy is then shared between the vibrational modes of the molecule, resulting in either IR emission (photo-relaxation) or in fragmentation via hydrogen or C_2H_n loss, where $n = 0, 1, 2$. The transfer of energy in an electronic interaction for a PAH is a topic that remains, by-and-large, theoretically unexplored. We use the theoretical modelling developed for fullerenes in Schlathölter et al. (1999) and Hadjar et al. (2001). We consider that a PAH delocalised valence electrons behave like an electron gas, giving rise to an effective stopping power of the ion S (Sigmund 1981):

$$S = \frac{dT}{dl} = \gamma(r_s)v, \quad (\text{A45})$$

where dT is the energy loss over the path length dl through the PAH electron gas, γ is the friction coefficient (Puska et al. 1983), and v is the incident ion velocity. The friction coefficient depends on the density parameter $r_s = (\frac{4}{3}\pi n_0)^{-1/3}$ which is itself a function of the valence electron density n_0 . In the fullerene jell-

ium model of Puska et al. (1983) n_0 assumes a spherical geometry, which requires some modifications for a disc geometry more reasonable for PAHs. The effective PAH radius R is computed using Eq. 28, and the π -electron cloud thickness is fixed to $d \sim 4.31 \text{ \AA}$. Applying the jellium model to n_0 for PAHs Hadjar et al. (2001), n_0 is given in terms of the coordinates l and θ :

$$n_0(l, \theta) = 0.15 \exp\left\{-\frac{(s \cos \theta)^2}{2.7}\right\} \quad (\text{A46})$$

where θ is the angle between the minor axis of the PAH and the direction of the incoming ion and s is the distance travelled through the PAH. The friction parameter has been computed by Puska et al. (1983) for different projectile ions with the following functional form:

$$\gamma(r_s) = \Gamma_0 \exp\left(-\frac{r_s(s, \theta) - 1.5}{R_2}\right), \quad (\text{A47})$$

where Γ_0 and R_2 are fitting parameters to their experimental results and given in Table A4 for the main ion projectiles that contribute to thermal sputtering (i.e. H, He, C and O). The total energy transferred can then be computed by integrating Eq. A45 for a given incidence angle θ :

$$T_e(\theta) = \int_{-L(\theta)/2}^{L(\theta)/2} \gamma(r_s(l, \theta))v ds, \quad (\text{A48})$$

where L is the total path length through the PAH. Given the PAH disc geometry, $|\tan(\theta)| < \tan(\alpha)$, then $L(\theta) = d/\cos(\theta)$, and otherwise $L(\theta) = 2R/|\sin(\theta)|$. This means that if the angle of incidence is $\theta = \pi/2$ the path length will be maximal, and hence so will the energy transferred.

Ions colliding with a PAH may also remove a C atom from the PAH skeleton, for which we need to consider the

Element	Γ_0/a_0^2	R_2
H	0.33	2.28
He	0.75	0.88
C	1.68	0.90
O	1.62	0.57

TABLE A4: Fitting parameters for the electron friction (Eq. A47) taken from the theoretical predictions of Puska et al. (1983). The scaling parameter Γ_0 is given in units of the the Bohr radius $a_0 \simeq 5.291 \times 10^{-11}$ m.

theory of nuclear collisions by Micelotta et al. (2010b). In this case, we only consider collisions with energies above the threshold energy, T_0 , of C removal. The destruction rate $R_N^k(T, N_C)$ (the subscript N stands for ‘Nuclear’) is given by a collisional rate weighted by the Maxwellian velocity distribution $f(v, T)$ for ion k in the gas, and adding the correction due to Coulomb focusing with the F_C factor (see Section 2.4) to the original derivation in Micelotta et al. (2010a):

$$R_N^k(T, N_C) = \frac{1}{2} N_C n_k F_C \int_{v_0}^{\infty} v \sigma_{N,k}(v, T_0) f(v, T) dv, \quad (\text{A49})$$

where n_k is the local number density of ion k , N_C is the number of carbon atoms in the PAH, v_0 is the velocity corresponding to the threshold energy T_0 , and $\sigma_{N,k}(v, T_0)$ is the nuclear interaction cross-section per C atom, taken from interpolating the results in figure 2 of Micelotta et al. (2010b). The threshold energy T_0 is the minimum energy that a collision must transfer to a C atom to eject it from the PAH skeleton. However, as detailed in Micelotta et al. (2010b) the choice of T_0 is very uncertain, as there are no experimental nor theoretical determinations of its value for astrophysically relevant PAHs. The physical meaning of T_0 is also different from the threshold energy for atomic displacement used in solid state physics, which for graphite has been measured to vary from 12 eV (Nakai et al. 1991) up to 30 eV (Montet et al. 1967), while for amorphous carbon the value is suggested to be lower and close to 5 eV (Cosslett 1978). We hence choose a value of 7.5 eV as in Micelotta et al. (2010b) to be consistent with the experimental data observed for pseudo-PAH materials. We found that varying the value of T_0 from 4.5 to 15 eV mainly introduces a shift in the gas temperature at which sputtering starts to be relevant, from $\sim 5 \times 10^3$ K to $\sim 10^4$ K.

In the coronal hot gas (up to $\sim 10^8$ K), electrons can reach very high thermal velocities, with kinetic energies capable of significantly altering the internal energy of a PAH molecule. In these sub-relativistic regimes (~ 10 keV), elastic collisions between electrons and target nuclei are not effective, and instead inelastic interactions with target electrons dominate. Similar to the case of electronic excitations by hot ions, these inelastic interactions excite molecules, followed by either dissociation or IR photo-relaxation. However, at these low kinetic energies, the Born approximation is no longer valid (no impulsive interaction, see also Section 2.5), which obliges us to instead use experimentally motivated stopping powers. We use the fit to the electron stopping power S of solid carbon given by Eq. A29 with the parameters in Table A3. Since $S = -\frac{dE}{dl}$, we can find the maximum pathlength $L(\theta)$ through the PAH by numerically inte-

grating Eq. A29:

$$\int dl = - \int_{E_0}^{E_1} \frac{dE}{S(E)} = l_1 - l_0 = L(\theta), \quad (\text{A50})$$

where we integrate from the initial energy of the electron E_0 to its final energy E_1 upon exit from the PAH. Given that we know for a given θ the value of L , we can numerically solve Eq. A50 to determine the value of E_1 , such that the energy transferred by the electron to the π -valence electron cloud is simply $T_{\text{elec}}(\theta) = E_0 - E_1$.

In the microcanonical description of a PAH (e.g. Tielens 2005), and under the ergodic approximation, the microcanonical temperature T_m can be approximated by:

$$T_m \simeq 2000 \left(\frac{E_{\text{in}}}{\text{1eV}} \right)^{0.4} N_C^{-0.4} \text{K}, \quad (\text{A51})$$

which is valid over the range 35 – 1000 K. This can then be related to the effective temperature of the PAH for a particular internal energy E_{in} :

$$T_{\text{eff}} = T_m \left(1 - 0.2 \frac{E_{\text{bind}}}{E_{\text{in}}} \right), \quad (\text{A52})$$

with E_{bind} the binding energy of the dissociated fragment (e.g. C_2H_n). The second term in Eq. A52 is a correction factor due to the finite heat bath obtained when Taylor expanding the system energy E around the average energy $\langle E(T_m) \rangle$. Therefore, the effective PAH temperature for a given excitation energy T_e (in eV) is approximately (Draine & Li 2001; Tielens 2005):

$$T_{\text{eff}} \simeq 2000 \left(\frac{T_e}{N_C} \right)^{0.4} \left(1 - 0.2 \frac{E_{\text{bind}}}{T_e} \right) \text{K}. \quad (\text{A53})$$

In the Gibbs microcanonical distribution, the bond dissociation rate k_{diss} is estimated via the Arrhenius law (Tielens 2005):

$$k_{\text{diss}} = k_0(T_{\text{eff}}) \exp\left(-\frac{E_{\text{bind}}}{k_B T_{\text{eff}}}\right), \quad (\text{A54})$$

where k_0 is a coefficient estimated by:

$$k_0(T_{\text{eff}}) = \frac{k_B T_{\text{eff}}}{h} \exp\left(1 + \frac{\Delta S}{\mathcal{R}}\right), \quad (\text{A55})$$

where h is Planck’s constant, ΔS is the change in entropy due to dissociation, and \mathcal{R} is the ideal gas constant. We use the dissociation parameters for the acetylene fragment (C_2H_2) given in Micelotta et al. (2010a) and Ling et al. (1998). We now need to consider the competition between this dissociation pathway and IR photo-relaxation. Computing the probability for dissociation requires evaluating the photon emission and photo-dissociation rates over the energy cascade resulting from each IR photon emission. This quickly becomes a difficult numerical task, but because of the steep dependence of the dissociation rate k_{diss} on the internal energy (Eq. A54), one can simplify this computation by evaluating the internal energy before IR cooling sets in (Tielens 2021). We follow an approach to this method presented in Micelotta et al. (2010a), in which we assume all photons have the same energy $\Delta\epsilon = 0.16$ eV, corresponding

Fragment	E_0 [eV]	ΔS [cal K ⁻¹ mol ⁻¹]
H	4.3	11.8
H ₂	3.52	-12.69
C ₂ H ₂	4.6	10.0

TABLE A5: Dissociation parameters used for our PAHs with normal hydrogen coverage.

to a typical C-C vibrational mode. In this case, the normalised dissociation probability²⁶ is given by:

$$P(n_{\max}) = \frac{k_0 \exp[-E_{\text{bind}}/(k_B T_{\text{av}})]}{k_{\text{IR}}/(n_{\max} + 1) + k_0 \exp[-E_{\text{bind}}/(k_B T_{\text{av}})]}, \quad (\text{A56})$$

where T_{av} is the geometric mean of the PAH effective temperature between the initial excitation energy and the final equilibrium internal energy after n_{\max} IR photon emissions. Naively, n_{\max} could be estimated as $n_{\max} = (T_{\text{eff}} - E_{\text{bind}})/\Delta\epsilon$, assuming that the probability for dissociation after each IR photon emission is the same. However, an accurate computation of the probability indicates that these probabilities decrease. In [Micelotta et al. \(2010a\)](#) they instead determine the value of n_{\max} as the step at which the probability has decreased by a factor of 10 with respect to the previous step. We have obtained a simple scaling from their n_{\max} for different N_C given by $n_{\max} = N_C/5$. Once the dissociation probability $P(v, \theta, N_C)$ is computed, we can obtain the mean dissociation rate for a given particle velocity v_k :

$$R_e^k(v, N_C) = v_k n_k F_C \times \int_0^{\pi/2} \sigma_{\text{PAH,geo}}(N_C, \theta) P(v, \theta, N_C) \sin \theta d\theta. \quad (\text{A57})$$

where here k goes over ions and electrons as well, and the PAH geometrical cross-section seen by a particle colliding with a PAH depends on the angle θ as follows:

$$\sigma_{\text{PAH,geo}}(N_C, \theta) = \pi R(N_C)^2 \cos \theta + 2R(N_C)d \sin \theta. \quad (\text{A58})$$

This can be integrated over the full Maxwellian distribution to give the total collision rate constant at a given T :

$$R_e^k(T, N_C) = \int_{v_0}^{\infty} R_e^k(v, N_C) f(v, T) dv, \quad (\text{A59})$$

where v_0 is the impinging electron or ion velocity corresponding to the binding energy of the acetylene group E_{bind} .

In [Fig. A4a](#) we present the results of our PAH sputtering model for small PAHs ($N_C = 54$) embedded in ionised gas with density of 1 cm^{-3} and metal solar abundance following [Asplund et al. \(2009\)](#). We drop the dependence on the factor F_C as this depends on the ion charge. Therefore, these rate constants are in units of C-atom/s (such that the sputtering mass-loss timescale can be computed with [Eq. 29](#)), for electronic ion collisions ([Eq. A59](#) with the probability obtained for the excitation energy given by [Eq. A48](#)), nuclear ion collisions ([Eq. A49](#)), and free electron collisions ([Eq. A59](#)

²⁶ Note that in [Micelotta et al. \(2010a\)](#) $P(n_{\max})$ is defined as the un-normalised probability, i.e. is missing the second term in the denominator.

with the deposited energy given by [Eq. A50](#)). For the ions, we separate the contributions into electronic and nuclear rates coming from the dominant ions: H, He, C and O. Thermal sputtering becomes a relevant process for PAHs at $\sim 10^4 \text{ K}$, i.e. approximately 1 dex lower in temperature than thermal sputtering for regular dust grains (see [Section 2.5](#)). At this temperature, the nuclear collisions dominate the destruction rate, with H and He dominating due to their larger abundance with respect to C and O. Above $\sim 10^4 \text{ K}$ the destruction rate by free electrons grows sharply becoming the dominant sputtering agent in warm ionised gas (blue solid line). The electron sputtering peaks at $\sim 10^6 \text{ K}$, decreasing at higher temperatures due to decreasing stopping power ([Eq. A45](#)) at these thermal energies. Ion electronic collisions start to dominate the PAH sputtering rate only when gas temperatures reach $\sim 10^8 \text{ K}$, again, mainly driven by H and He collisions.

We have also computed these rates for our large PAHs ($N_C = 418$) in [Fig. A4b](#). Due to direct dependence of nuclear sputtering rate on N_C , large PAHs are dominated by C direct collisions up to $\gtrsim 10^7 \text{ K}$. Also, the N_C -dependence is implicit in the electron excitations, which means that electron and ion electronic collisions differ significantly from their smaller PAH counterparts. We find that for large PAHs, free electron collisions are subdominant at all temperatures.

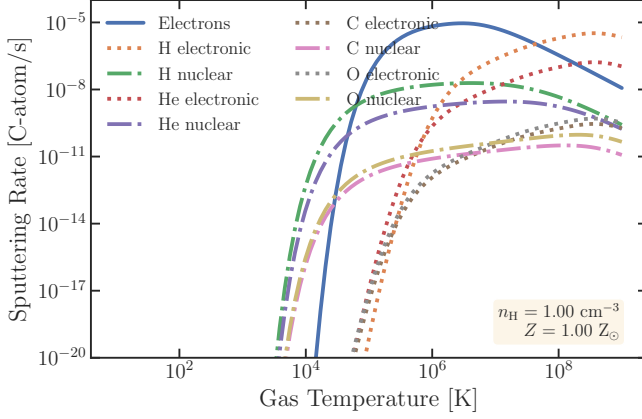
A.5. Equilibrium charge distribution of PAHs and their PEH and recombination cooling

To be consistent with the rest of the photo-physical processes considered for PAHs, we use the distribution-averaged cross-sections in [Section 3.1](#) which have been computed for the small and large PAH bins based on the theoretical curves by [Li & Draine \(2001\)](#). In this model we assume that with both grain sizes we can explore the charge parameter space $Q \in -1, 0, 1, 2$. Larger grains are capable of reaching higher ionisation states than smaller grains. While this could be the case for PAH clusters ($\sim 10 \text{ \AA}$), we have opted to maintain the di-cation as the maximum ionisation state for all PAHs (see also [Andrews et al. 2016](#); [Ibanez-Mejia et al. 2019](#)). Experimental data for the ionisation potential (IP) of the di-cation is limited ([Zhen et al. 2016](#)), but it seems that it is higher than 13.6 eV for small PAHs, and theoretical modelling argue for a negligible variation at least up to circumcoronene ($N_C = 96$, [Andrews et al. 2016](#)). For the rest of the charge states, we use the IP fitting function from [Jochims et al. \(1996\)](#); [Verstraete et al. \(1990\)](#) and updated by [Wenzel et al. \(2020\)](#). We assume that $IP^0 = 0$ for $Q = -1$. Based on the experimental studies of neutral ([Jochims et al. 1996](#); [Verstraete et al. 1990](#)) and cationic ([Zhen et al. 2016](#)) PAHs ([Wenzel et al. 2020](#)), empirical functions can be derived for the electron yield of different PAHs. For the neutral species, we use the yields from [Jochims et al. \(1996\)](#)²⁷:

$$Y(E, Q) = \begin{cases} \frac{E - IP^+}{9.2} & , E \leq IP^+ + 9.2 \\ 1 & , E > IP^+ + 9.2 \end{cases}, \quad (\text{A60})$$

with IP^+ referring to the ionisation potential from $Q = 0$ to $Q = 1$. In the case of the first cation, we use the yields

²⁷ Energy values are expressed in eV here and in the following.



(a) Results for small PAHs ($N_C = 54$). Nuclear collisions are only important at the onset of sputtering at $\sim 10^4$ K, quickly overcome by the free electron destruction rate, peaking at $\sim 10^6$ K. Ion electronic excitations play an important role at very high gas temperatures.

FIG. A4.—: Sputtering rates for different PAH sizes due to free electron collisions (solid blue line), ion electronic excitations (dashed lines), and nuclear collisions (dot-dashed lines), separated by different ions: H, He, C and O. These rates have been computed for a gas density of 1 cm^{-3} and assuming solar metal abundances (Asplund et al. 2009).

from Wenzel et al. (2020):

$$Y(E, Q) = \begin{cases} 0 & , E < IP^{2+} \\ \frac{\alpha}{11.3 - IP^{2+}} (E - IP^{2+}) & , IP^{2+} \leq E < 11.3 \\ \alpha & , 11.3 \leq E < 12.9 \\ \frac{\beta(N_C) - \alpha}{2.1} (E - 12.9) & , 12.9 \leq E < 15.0 \\ \beta(N_C) & , E \geq 15.0 \end{cases}, \quad (\text{A61})$$

where $\alpha = 0.3$ and the correction factor β is given by:

$$\beta(N_C) = \begin{cases} 0.59 + 8.1 \times 10^{-3} N_C & , 32 \leq N_C < 50 \\ 1 & , N_C \geq 50 \end{cases}. \quad (\text{A62})$$

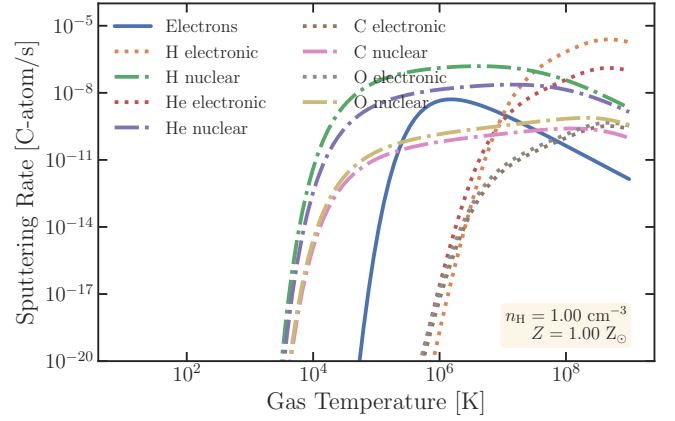
We set the ionisation yield of the anion equal to 1. This is an approximation, as recent experimental data (Iida et al. 2021) has shown that electron detachment does not occur for the energy expected from electron affinity for the pentacene anion ($\text{C}_{22}\text{H}_{14}$), but instead experiments show efficient detachment for photon energies E beyond 2.8 eV. It remains unclear how this extrapolates to the larger PAH molecules and PAH clusters that we consider in CALIMA, but given the little effect on the PEH efficiency of having $IP^0 > 0$ (Berné et al. 2022), we have maintained this approximation across our PEH model.

The ionisation cross-section is defined as:

$$\sigma_{\text{ion}}(N_C, E, Q) = Y(E, Q) \langle C_{\text{abs}}(N_C, E, Q) \rangle, \quad (\text{A63})$$

which we assume to be in units of m^2 in this section and C_{abs} is the absorption cross-section in Section 3.1. From this definition we can compute the ionisation rate for a PAH molecule of charge Q and number of carbons N_C :

$$k_{\text{pe}}(N_C, Q) = \int_{IP^{Q+1}}^{13.6} \frac{\sigma_{\text{ion}}(N_C, E, Q) F(E)}{E} dE, \quad (\text{A64})$$



(b) Results for large PAHs ($N_C = 418$). In this case, nuclear collisions dominate across all temperatures, with direct C collision important up to $\sim 10^7$ K, and nuclear electronic excitations at higher temperatures. Collisions with free electrons are less relevant.

where $F(E)$ is the flux density of the radiation field. Photo-ionisation is only allowed for photons with energy E above the ionisation potential and below the Lyman limit. The recombination rate is calculated using Spitzer's method adapted by Verstraete et al. (1990) for cations:

$$k_{\text{rec}} = 4.27 \times 10^{-13} N_C (1 + \Phi) \left(\frac{T}{300\text{K}} \right)^{1/2} \text{ cm}^3 \text{ s}^{-1}, \quad (\text{A65})$$

where we have defined the dimensionless quantity:

$$\Phi = \frac{eU}{k_B T} = N_C^{-1/2} \left(\frac{T}{1.85 \times 10^5 \text{K}} \right)^{-1} \quad (\text{A66})$$

where U is the mean electrostatic potential evaluated at the radius of the PAH. This equation can be extended to allow all cations ($Q > 0$):

$$k_{\text{rec}} = 4.27 \times 10^{-13} N_C (1 + \Phi(1 + Q)) \left(\frac{T}{300\text{K}} \right)^{1/2} \text{ cm}^3 \text{ s}^{-1}. \quad (\text{A67})$$

The electron attachment rate comes from empirical rates fitted to the quantum mechanical computations of Carelli et al. (2013):

$$k_{\text{att}} = 2.74 \times 10^{-9} \left(\frac{T}{300\text{K}} \right)^{0.11} \exp\left(\frac{1.11 \text{K}}{T} \right) \text{ cm}^3 \text{ s}^{-1}. \quad (\text{A68})$$

For the fitting parameters a , b and c we use the results for coronene, the largest molecule in their study. Both electron recombination and attachment rates are very uncertain aspects of our PEH modelling.

Another option available in CALIMA for the electron recombination rate (see Section 4.1) is the one given by

Tielens (2005):

$$k_{\text{rec}} \simeq 1.3 \times 10^{-6} \sqrt{N_{\text{C}} \frac{300 \text{ K}}{T}} \text{ cm}^3 \text{ s}^{-1}, \quad (\text{A69})$$

which is independent of Q . Experimentally measured rates for ionised small PAHs (Abouelaziz et al. 1993; Rebrion-Rowe et al. 2003; Novotný et al. 2005; Bienner et al. 2005) fall well below the rate given by Eq. A69. One explanation for this unexpected low sticking efficiency in small PAHs could be that dissociative recombination becomes important. When PAH cations recombine with electrons their internal energy is increased by the value of IP . This excited state needs to reach a new stable state, which could trigger molecular dissociation. However, for the IP of circumcoronene cations (5.9 and 8.8 eV for the first and second ionisation states) the IR relaxation rate is about 2 orders of magnitude larger than the dissociation rate (e.g. Montillaud et al. 2013; Andrews et al. 2016), and for larger PAHs their IP is even smaller. This means that, for the PAHs of interest in this model, recombination is expected to be non-dissociative. Therefore, we assume that this extrapolated stability to ISM-relevant PAHs results in a roughly constant k_{rec} value of $10^{-5} \text{ cm}^3 \text{ s}^{-1}$, close to the prediction of Eq. A67. Similarly, for electron attachment to neutral PAHs, the electron affinity increases with PAH size and for $N_{\text{C}} > 30$ it exceeds 1 eV and auto-ionisation is very unlikely. Therefore, from the PAH polarisability, we obtain (Tielens 2021):

$$k_{\text{att}} \simeq 1.3 \times 10^{-7} N_{\text{C}} \text{ cm}^3 \text{ s}^{-1}. \quad (\text{A70})$$

Again, this rate falls well above the experimental results of Tobita et al. (1992) and Canosa et al. (1994), which reported a rate close to $10^{-9} \text{ cm}^3 \text{ s}^{-1}$. Given the lack of experimental studies on astrophysically relevant PAHs, we have opted to use the more conservative rates from Verstraete et al. (1990) and Carelli et al. (2013). These rates are highly uncertain, so both implementations of recombination and attachment are implemented in CALIMA, allowing future work to further constraint what prescription better agrees with PAH charging observations. In the future, these rates will need to be revised once further progress has been made on the experimental measurements of large PAHs.

By assuming equilibrium between the different processes driving the evolution of the different population charges, we obtain (Berné et al. 2022):

$$f^- = \left(1 + \frac{k_{\text{det}}}{k_{\text{att}} n_{\text{e}}} + \frac{k_{\text{det}} k_{\text{pe}}^0}{k_{\text{att}} k_{\text{rec}}^+ n_{\text{e}}^2} + \frac{k_{\text{det}} k_{\text{pe}}^0 k_{\text{pe}}^+}{k_{\text{att}} k_{\text{rec}}^+ k_{\text{rec}}^{2+} n_{\text{e}}^3} \right)^{-1}, \quad (\text{A71})$$

$$f^0 = \left(1 + \frac{k_{\text{att}} n_{\text{e}}}{k_{\text{det}}} + \frac{k_{\text{pe}}^0}{k_{\text{rec}}^+ n_{\text{e}}} + \frac{k_{\text{pe}}^0 k_{\text{pe}}^+}{k_{\text{rec}}^+ k_{\text{rec}}^{2+} n_{\text{e}}^2} \right)^{-1}, \quad (\text{A72})$$

$$f^+ = \left(1 + \frac{k_{\text{rec}}^+ n_{\text{e}}}{k_{\text{pe}}^0} + \frac{k_{\text{pe}}^+}{k_{\text{rec}}^+} + \frac{k_{\text{att}} k_{\text{rec}}^+ n_{\text{e}}^2}{k_{\text{det}} k_{\text{pe}}^0} \right)^{-1}, \quad (\text{A73})$$

$$f^{2+} = \left(1 + \frac{k_{\text{rec}}^{2+} n_{\text{e}}}{k_{\text{pe}}^+} \right)^{-1}, \quad (\text{A74})$$

where f^- , f^0 , f^+ and f^{2+} are the fractions of PAH

molecules in the anion, neutral, mono-cation, and dication states, respectively, and $k_{\text{det}} = k_{\text{pe}}^-$. Based on this, we can compute the power injected by the photo-electrons from the first three charge states above:

$$P_e^{\text{tot}} = f^- P_e^- + f^0 P_e^0 + f^+ P_e^+, \quad (\text{A75})$$

where the power injected in the gas by the charge state Q is defined as:

$$P_e^Q = \int_{IP^{Q+1}}^{13.6} \gamma_e(E) (E - IP^{Q+1}) \sigma_{\text{ion}}(N_{\text{C}}, E, Q) \frac{F(E)}{E} dE, \quad (\text{A76})$$

with $\gamma_e(E)$ encapsulating the fraction of the energy which goes into the kinetic energy E_{K} of the photo-electron. Energy conservation requires $E - IP = \Delta E^*(E) + E_{\text{K}}(E) + E_{\text{K}}^{\text{PAH}}(E)$, where ΔE^* is the change in internal energy of the PAH upon excitation by ionisation and $E_{\text{K}}^{\text{PAH}}$ is its kinetic energy. PAH molecule has much larger mass than the electron's and due to conservation of momentum, the kinetic energy of the PAH molecule is negligible compared to that of the electron. Therefore, assuming that the photon energy is primarily used for the ionisation reaction, the internal energy of the PAH is barely modified, allowing to define the energy averaged partition coefficient (D'Hendecourt et al. 1987):

$$\langle \gamma_e(E) \rangle = \left\langle \frac{E_{\text{K}}(E)}{E - IP} \right\rangle. \quad (\text{A77})$$

We use the estimated value of $\langle \gamma_e(E) \rangle = 0.46 \pm 0.06$ obtained by Berné et al. (2022) from the spectroscopic measurements performed for the coronene molecule by Bréchnignac et al. (2014). The final outcome of any PEH model is the total heating efficiency, ϵ_{PAH} , defined as the ratio of the power injected by the photo-electrons and the power absorbed by the PAHs:

$$\begin{aligned} \epsilon_{\text{PAH}}(N_{\text{C}}) &= \frac{P_e^{\text{tot}}}{P_{\text{abs}}^{\text{tot}}} \quad (\text{A78}) \\ &= \frac{P_e^{\text{tot}}}{f^- P_{\text{abs}}^- + f^0 P_{\text{abs}}^0 + f^+ P_{\text{abs}}^+ + f^{2+} P_{\text{abs}}^{2+}}. \quad (\text{A79}) \end{aligned}$$

where the power absorbed by each PAH charge state is:

$$P_{\text{abs}}^Q = \int_0^{13.6 \text{ eV}} \langle \sigma_{\text{abs}}(N_{\text{C}}, E, Q) \rangle F(E) dE. \quad (\text{A80})$$

This definition of the PEH efficiency is similar to that used by Weingartner & Draine (2001a) but differs from Bakes et al. (1994) as they only consider photons in the range 6 – 13.6 eV. From this, the local PEH rate for each PAH size bin writes:

$$\Gamma_{\text{PAH}}(N_{\text{C}}) = \epsilon_{\text{PAH}} P_{\text{abs}}^{\text{tot}} n_{\text{PAH}}(N_{\text{C}}), \quad (\text{A81})$$

with $n_{\text{PAH}}(N_{\text{C}})$ being the local number density of PAH molecules with carbon number N_{C} .

In Fig. A5 we show the results of our modelling of the PAH charge distribution and PEH for the small (solid lines) and large (dashed lines) PAHs. In order to allow benchmarking against the modelling in Berné et al. (2022) (dotted lines) for $N_{\text{C}} = 54$, we use the Draine (1978) ISRF, fixing the gas temperature to 10^4 K and

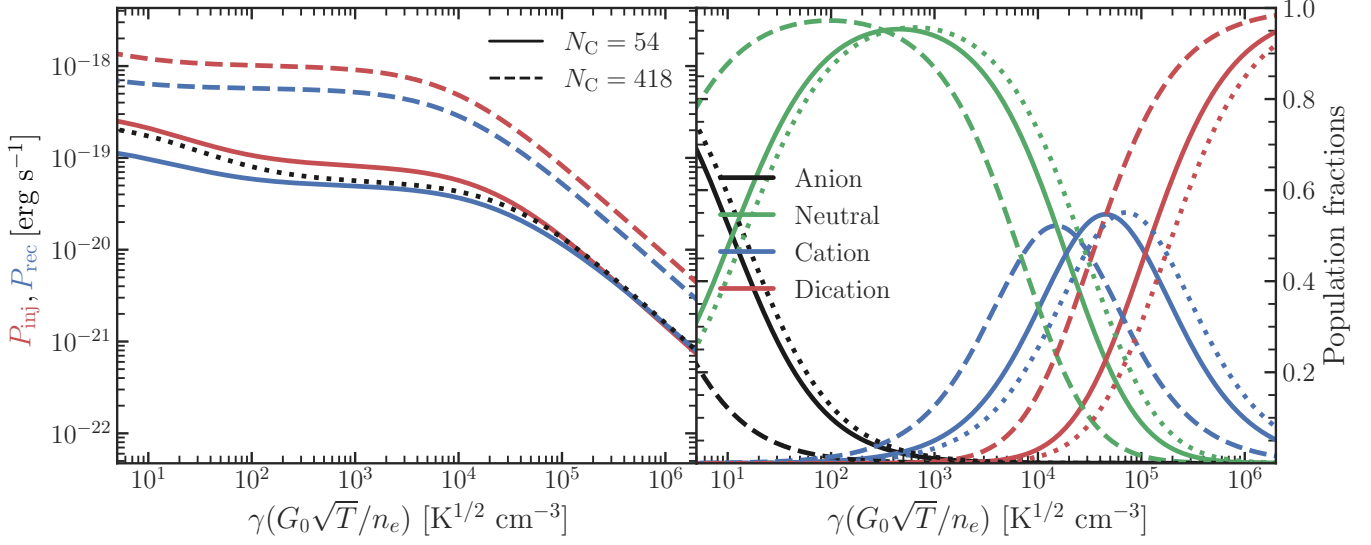


FIG. A5.—: Photo-electric heating, recombination cooling and PAH charge distributions embedded in the [Draine \(1978\)](#) at constant $T = 10^4$ K and varying charging parameter γ . We separate the contribution from small (solid lines) and large (dashed lines) PAHs, comparing also to the results from [Berné et al. \(2022\)](#) for $N_C = 54$ (dotted lines). *Left panel*: per PAH injected (red) and recombined (blue) power evolution with γ . *Right panel*: PAH charge fraction for anions (black), neutral (green), cation (blue), and dication (red). Given the $\lesssim 50\%$ lower cross-section for anion and neutral PAHs used in [Berné et al. \(2022\)](#) compared to ours, we find $\sim 50\%$ higher injected power at $\gamma < 10^4$.

varying the value of n_e to span the range of charging parameter γ of interest for PEH. Since the anion and neutral PAH cross-sections from [Mallocci et al. \(2004\)](#) are on average $\sim 30\%$ smaller than ours, we find on a difference of $\sim 20\%$ in the computed injected power (solid red line). This difference can also be appreciated in the population fractions of each charge state in the right panel of [Fig. A5](#). The most effective PAH charges for photoelectron ejection are the anion and the neutral, which dominate for $\gamma \lesssim 10^4 \text{ K}^{1/2} \text{ cm}^{-3}$, explaining the plateau in ϵ_{PAH} observed below this ionisation parameter value. We do not include it in this plot, but using the recombination and attachment rates from [Tielens \(2021\)](#) as

described above has a critical effect on the distribution of PAH charges, allowing for the dominance of anions ($Z = -1$) at low γ , and therefore an efficiency 4 times larger at $10^2 < \gamma < 10^4 \text{ K}^{1/2} \text{ cm}^{-3}$.

This paper was built using the Open Journal of Astrophysics \LaTeX template. The OJA is a journal which provides fast and easy peer review for new papers in the [astro-ph](#) section of the arXiv, making the reviewing process simpler for authors and referees alike. Learn more at <http://astro.theoj.org>.